DISSERTATION

IMPACTS OF ARCTIC WARMING AND SEA ICE LOSS ON THE NORTHERN HEMISPHERE MID-LATITUDE LARGE-SCALE CIRCULATION

Submitted by

Bryn Ronalds

Department of Atmospheric Science

In partial fulfillment of the requirements

For the Degree of Doctor of Philosophy

Colorado State University

Fort Collins, Colorado

Spring 2020

Doctoral Committee:

Advisor: Elizabeth A. Barnes

David Thompson
David A. Randall
Richard Eykholt

ABSTRACT

IMPACTS OF ARCTIC WARMING AND SEA ICE LOSS ON THE NORTHERN HEMISPHERE MID-LATITUDE LARGE-SCALE CIRCULATION

The consequences of the rapid warming of the Arctic and associated sea ice loss on the Northern Hemisphere atmospheric circulation is still largely debated. The uncertainty in the circulation response stems from a poor understanding of the underlying physical mechanisms of the remote response, regional and seasonal differences, differences between models and experimental set-ups, the large internal variability of the system, and the short observational record. This research seeks to address some of this uncertainty, specifically the uncertainty related to the physical mechanisms, regionality, and modeling differences.

The wintertime Northern Hemisphere eddy-driven jet streams over the North Pacific and North Atlantic basins exhibit differing responses to Arctic warming and sea ice loss in a fully coupled climate model. In the North Atlantic the jet weakens, narrows along the poleward flank, and shifts slightly equatorward. This response is similar to previous studies examining the Northern Hemisphere zonal mean jet response. In contrast, the North Pacific jet strengthens and extends eastward in response to Arctic sea ice loss, with no change in latitude, and narrows slightly along the poleward flank. In both cases, there are high latitude anomalous easterlies in the region of sea ice loss, where the local surface temperature gradients are weakening. This can lead to changes in locations and frequency of wave-breaking, thus leading to changes in the mean zonal winds further south, in the vicinity of the jet. This work relates the differing changes in the North Pacific and North Atlantic to these changes in wave-breaking in a simplified atmospheric model, and posits that the location of the jet relative to the region of Arctic sea ice loss is a dominant factor in determining the mean jet response to the sea ice loss and local warming.

Changes in the mean wintertime Northern Hemisphere midlatitude zonal winds are found to be indicative of changes to the sub-seasonal variability of the wintertime zonal winds. The sub-seasonal circulation patterns over the ocean basins are closely linked with continental weather

regimes, including changes in temperature and precipitation. While establishing a causal link between Arctic sea ice loss and changes to remote weather regimes in the observational record remains difficult, the Polar Amplification Model Intercomparison Project (PAMIP) provides insight into possible relationships and consequences. The design of the project eliminates differences in experimental set-ups across models and aids in addressing the uncertainty in regional responses. Across four climate models, Arctic sea ice loss leads to a strengthened and extended North Pacific jet in the January-February mean. This mean change is also associated with changes to the sub-seasonal, wintertime North Pacific zonal wind variability. All four models show an increase in strengthened and extended North Pacific eddy-driven jet stream events and a decrease in weakened, retracted and equatorward-shifted North Pacific jet events in January-February. Previous work has also established the relationships between North Pacific jet stream variability and downstream, North American weather regimes, and changes to the former are expected to impact the latter. Again, there is model agreement in an increase of a warm west/cold east temperature dipole over North America, associated with the strengthened and extended jet events. There is also a decrease in cold air temperature anomalies over North America, associated with weakened and equatorward-shifted jet events.

ACKNOWLEDGMENTS

This dissertation has been far from a solo affair. This work would not have been possible without the exceptional emotional support from family and friends, and the incredible scientific and research support from my advisor, professors and colleagues. I would like to specifically acknowledge several of you here.

My incredible advisor, Libby Barnes, has been beyond instrumental in this work. This includes, and is not limited to, her enthusiasm for research, her stellar edits, and her patience and guidance, both at times where things were going smoothly, and times where nothing was going right. I feel exceptionally lucky that she accepted my application and chose to work with me for the last four years, it means the world. You have taught me so much, and are hands down the best professor I've ever had. Thank you for never giving up on me, and always believing in what I can accomplish.

My professors and committee members have expanded my knowledge base far beyond what I thought possible. Learning the fundamentals of atmospheric modeling from Dave Randall was a pleasure, and not something I ever thought I could do. Classes with Dave Thompson and Libby Barnes were also fascinating, informative and fun! In addition, the group dynamics meetings with the Dave Thompson, Dave Randall, Eric Maloney, Libby Barnes and Jim Hurrell research groups have been invaluable. These meetings provided much more than updates on research, they also provided a place to develop communication skills both as the researcher and as the audience member, and empowered me as a scientist. I never believed that I'd be able to understand the research being presented, much less be able to ask questions in a group atmosphere. Thank you to my outside committee member, Richard Eykholt for trekking out to the Atmospheric Science campus, and a huge thank you to Karan Venayagamoorthy, for stepping in at the last minute to observe my defence.

There have been so many helpful encounters with my fellow students here at the department, but I wish to highlight one person in particular. Marie McGraw has not only been a source of unending emotional support and an amazing friend, she has also provided her insight and intelligence many times throughout my stay here at Colorado State. Her willingness to always go the extra mile,

and her breadth of knowledge has been instrumental in my success here. Merci mille fois, Marie.

My family and friends, both here in Colorado and those back home or abroad, have also played a huge role in my ability to stay focused, somewhat centered, and persevere throughout the course of this degree. A huge thanks to Kyle Chudler, friend since day one and chosen brother, I could not have done this without you. Also thank you to the Mikes: Natoli and Cheeseman. You have both been my family and support, and I am grateful to you both. Thank you to Colleen Brents for being an amazing friend and accountabili-buddy. Chad Ronalds, aka Chad the Rad Dad, and the best father in the world, I am so lucky to always have you cheering in my corner. Same goes to my sisters, Caroline, Emilie, Katianna and Genevieve, you guys keep me sane sometimes, totally insane others, and always remind to be proud of myself. Thank you to the Fam 5. Je t'aime!

I also have to thank the following people for being great email correspondents as we all figure out this PAMIP output together: Rosie Eade, Yannick Peings and Lantao Sun. This last paper would not have been possible without all of you. Lantao especially has provided a great deal of aid, data, information and support throughout the entirety of my time at Colorado State. I'd also like to thank Clara Deser at the National Center for Atmospheric Research for her interest and support of my work. It continuously thrills me to receive positive feedback from you Clara, thank you.

There are so many other people that can be included in these acknowledgments, but in the interest of space I will finish by saying that the community here at Colorado State is unsurpassable. The students are all fiercely intelligent and also highly supportive of one another, the professors put extra effort into helping all of us succeed, and the staff is top notch. I enjoyed my time here immensely, thank you all.

TABLE OF CONTENTS

LIST OF FIGURES

1 Introduction

Recent decades have seen the rise of sea levels (e.g. Douglas 1991; Vermeer and Rahmstorf 2009), the increase of global temperatures (e.g. Hansen et al. 2006; New et al. 2011), an increase in extreme weather events (e.g. Kirch et al. 2005; Lubchenco and Karl 2012), and the substantial loss of Arctic sea ice (e.g. Serreze 2003; Stroeve et al. 2008, 2012). All of these elements of global climate change are cause for concern, and there has been a huge amount of research into the possible economic, sociological and environmental impacts associated with these changes (e.g. Fatorić and Seekamp 2017; Palomo 2017; Blythe et al. 2019; Chan et al. 2019; Ciarli and Savona 2019; Gruda et al. 2019; Nordhaus 2019; Petrov et al. 2017; Raza et al. 2019; Thomas et al. 2019; Tschakert et al. 2019). In particular, the substantial warming of the Arctic and extreme sea ice loss has sparked countless debates on the possible economic, sociological and environmental consequences for the Northern Hemisphere (e.g. Alvarez et al. 2019; Falardeau and Bennett 2019; Yuan et al. 2019; Vincent 2020). In addition, there is widespread concern that Arctic warming and sea ice loss can impact and even change Northern Hemisphere atmospheric circulations and weather regimes (e.g. Strong and Davis 2008; Cohen et al. 2014; Vihma 2014; Kug et al. 2015; Lee et al. 2015; Cvijanovic et al. 2017; Cohen et al. 2018; Overland and Wang 2018a,b; Ronalds et al. 2018; Li and Luo 2019; Ronalds and Barnes 2019; Smith et al. 2019).

1.1 ARCTIC WARMING AND ATMOSPHERIC CIRCULATION

The Arctic is warming more than twice as fast as the global average temperature (e.g. Holland and Bitz 2003; Serreze and Francis 2006; Cohen et al. 2020). The combination of near-surface warming at high latitudes, the loss of sea ice, the melting of permafrost regions, and the disparity in temperature changes between the low and high latitudes can all impact both local and remote atmospheric circulation patterns (e.g. Strong and Davis 2008; Vihma 2014; Smith et al. 2019). One possibility is that the Northern Hemisphere midlatitude jet stream, associated with the storm tracks, will slow, or weaken, in response to Arctic warming due to the reduction of the equator-to-pole

temperature gradient (e.g. Peings and Magnusdottir 2014; Deser et al. 2016; Screen et al. 2018b). While some studies have found this to be true in both the zonal mean (e.g. Screen et al. 2018b) and in the North Atlantic (e.g. Deser et al. 2016), others have found the opposite response in the North Pacific (e.g. Barnes and Simpson 2017; Ronalds and Barnes 2019). Some studies also argue that a weakened jet will meander more, and could lead to increased blocking events, which are associated with extreme weather events (e.g. Francis and Vavrus 2012; Peings and Magnusdottir 2014; Overland et al. 2015), while others find no connection between Arctic sea ice loss and changes in blocking (e.g. Barnes 2013; Screen 2014; Hassanzadeh et al. 2014; Hassanzadeh and Kuang 2015). Some sources of this uncertainty in the Northern Hemisphere jet stream response include poor understanding of the particular physical mechanisms, model and experimental set-up differences, regionality, seasonality, and the large internal variability of the system (e.g. Deser et al. 2012; McGraw and Barnes 2016; Smith et al. 2019; Cohen et al. 2020). Addressing these uncertainties is therefore of paramount importance when studying the impacts of Arctic warming and sea ice loss on the atmospheric circulation.

1.2 SCOPE OF THIS WORK

The work presented here is focused on understanding the Northern Hemisphere, wintertime eddy-driven jet streams' responses to Arctic warming and sea ice loss, taking regionality into account, and identifying underlying mechanisms which explain the responses. The mean change in the wintertime jet stream is identified and investigated, as well as the change in sub-seasonal variability. Further, the ramifications of sub-seasonal variability changes in terms of associated weather regimes is also investigated. Some of the over-arching research questions being answered here include:

- What is the mean, wintertime eddy-driven jet stream response to Arctic warming and sea ice loss in the North Atlantic versus the North Pacific?
- What physical mechanism(s) can explain the responses?
- Will Arctic warming and sea ice loss change atmospheric circulation variability and alter dominant weather regimes, particularly over North America?

The three chapters of research which follow all focus on the lower-level zonal wind response to Arctic sea ice loss in modeling experiments. All three are written as stand-alone papers, and thus there will be some overlap of the literature reviews and methodologies. The first two research chapters have been published in peer-reviewed scientific journals, and use an idealized modeling framework to identify dynamical mechanisms for the eddy-driven jet responses seen in a sea ice loss experiment in a fully coupled climate model. The third research chapter will be submitted to a scientific journal in the coming months, and uses output from the ongoing Polar Amplification Model Intercomparison Project (PAMIP) to examine the North Pacific atmospheric circulation response to Arctic sea ice loss across four models.

In Chapter 2, the results from a fully coupled climate model Arctic sea ice loss experiment are used to motivate a series of idealized modeling experiments. The North Atlantic eddy-driven jet stream weakens in response to Arctic sea ice loss in the fully coupled climate model, and the zonal mean jet latitude shifts equatorward. Both this mean change and the decreased monthly variability of the North Atlantic jet latitude are explained using changes to wave propagation and associated changes to wave breaking locations.

> Ronalds, B., E.A. Barnes, and P. Hassanzadeh 2018: A Barotropic Mechanism for the Response of Jet Stream Variability to Arctic Amplification and Sea Ice Loss. *J. Climate*, **31**, 7069-7085, https://doi.org/10.1175/JCLI-D-17-0778.1

The same Arctic sea ice loss experiment in a fully coupled model is also used in Chapter 3 to motivate a set of idealized modeling experiments investigating the differences in the mean, wintertime eddy-driven jet responses in the North Atlantic versus the North Pacific basins. While the North Atlantic wintertime eddy-driven jet stream weakened in response to Arctic sea ice loss, the North Pacific jet strengthened. The difference in responses is investigated in an idealized modeling framework, where changes in wave breaking frequencies and locations alter the response of the mean jet. The differing responses in the idealized model depend on the jet latitude relative to the sea ice loss forcing.

Ronalds, B. and E.A. Barnes, 2019: A role for barotropic eddy-mean flow feedbacks in the zonal wind response to sea ice loss and Arctic Amplification. *J. Climate*, **32**, 7469-7481, https://doi.org/10.1175/JCLI-D-19-0157.1

The final research chapter, Chapter 4, examines the North Pacific response to sea ice loss using output from the ongoing Polar Amplification Model Intercomparison Project (PAMIP). Daily data from four models is available at this time, allowing for the study of both the mean, wintertime eddy-driven jet response, and the changes in the sub-seasonal variability of the low-level zonal winds over the North Pacific basin. The changes in variability are also associated with downstream changes in North American surface temperature variability. At the time of this dissertation only a few modeling centres have made the first tier of PAMIP experiments available, and this ongoing project will provide valuable research data for future projects. Current results suggest that the strengthened North Pacific eddy-driven jet stream is a robust response to Arctic sea ice loss, and that the changes in zonal wind variability across the North Pacific basin are related to changes in North American surface temperatures.

The last chapter of this dissertation summarizes the results of the research and provides a discussion on the implications for current and future research. It also includes comments and suggestions for future work.

2 A barotropic mechanism for the response of jet stream variability to Arctic amplification and sea ice loss[1]

Previous studies have found that the most consistent response of the eddy-driven jet to sea ice loss and Arctic amplification in fully coupled general circulation models (GCMs) is a broad region of anomalous easterlies on the poleward flank. In this study, a similar response is noted in a dry dynamical core GCM with imposed surface heating at the pole, and it is shown that in both a fully coupled GCM's North Atlantic basin and the dry dynamical core the anomalous easterlies cause an asymmetrical narrowing of the jet on the poleward flank of the climatological jet. A suite of barotropic model simulations run with polar forcing shows decreased jet positional variability consistent with a narrowing of the jet profile, and it is proposed that this narrowing decreases the distance Rossby waves can propagate away from the jet core, which drives changes in jet variability. Since Rossby wave propagation and dissipation is intrinsic to the development and maintenance of the eddy-driven jet, and is tightly coupled to a jet's variability, this acts as a meridional constraint on waves' ability to propagate outside of the jet core, leading to the decreased variability in zonal-mean jet position. The results from all three models demonstrates that this relationship is present across a model hierarchy.

2.1 INTRODUCTION

The eddy-driven jet stream has long been of interest to the scientific community due to its tight association with the storm tracks and synoptic weather (e.g. Hoskins and Valdes 1990; Cione et al. 1993; Hartmann 2007; Eichelberger and Hartmann 2007; Yoshiike and Kawamura 2009; Woollings et al. 2018). Because storm tracks gain energy from highly baroclinic regions they are most often associated with warm ocean currents and land-sea contrast, placing them in proximity

[1]This chapter contains material that has been published in the *Journal of Climate* as: Ronalds, B., E.A. Barnes, and P. Hassanzadeh 2018: A Barotropic Mechanism for the Response of Jet Stream Variability to Arctic amplification and Sea Ice Loss. *J. Climate*, **31**, 7069-7085, `https://doi.org/10.1175/JCLI-D-17-0778.1`.

to heavily populated coastlines (e.g. Hoskins and Valdes 1990; Held 1993; Brayshaw et al. 2009). Many environmental factors are expected to impact the jet and, recently, great interest has been placed on the warming of the Arctic and associated sea ice loss (e.g. Magnusdottir et al. 2004; Deser et al. 2004, 2010; Francis and Vavrus 2012; Barnes 2013; Screen et al. 2013; Deser et al. 2015; Smith et al. 2017). Specifically, in recent decades the Arctic near-surface has warmed at an accelerated rate, almost double that of the globally averaged temperature (e.g. Holland and Bitz 2003; Serreze and Francis 2006; Screen and Simmonds 2010). This accelerated warming is commonly referred to as Arctic amplification, and is due, in part, to cryospheric feedbacks associated with changes in sea ice concentration and thickness (e.g. Serreze and Francis 2006; Winton 2006), and high-latitude cloud cover (e.g. Graversen and Wang 2009), to name a few. Recent studies examining the impact of Arctic amplification and sea ice loss on the eddy-driven jet have found the response to be a weakening due to thermal wind balance and an equatorward shift (e.g. Fletcher et al. 2009; Francis and Vavrus 2012; Liu et al. 2012; Peings and Magnusdottir 2014; Francis and Vavrus 2015; Petrie et al. 2015). These studies suggest that as a result of this weakening, the jet stream becomes “wavier", though other studies have failed to find this relation in either observations or models (e.g. Barnes 2013; Screen 2014; Hassanzadeh et al. 2014; Hassanzadeh and Kuang 2015). Many of these studies focus on the North Atlantic jet stream, comparing its response to Arctic amplification to its leading mode of variability, commonly called the North Atlantic Oscillation (NAO; e.g. Deser et al. 2004; Screen et al. 2013; Petrie et al. 2015). The NAO is characterized by a north-south shifting of the jet: in its positive phase the jet is shifted further poleward, and vice versa (e.g. Wittman et al. 2005). For the purposes of this work we refer to the meridional shifting of a relatively zonal jet as jet positional variability, using the zonal-mean jet position over time as a metric. In this study, we explicitly quantify the response of the jet positional variability to Arctic amplification and sea ice loss in a hierarchy of models, and propose a barotropic mechanism explaining the resulting behaviour. Our aim is to understand fundamental barotropic mechanisms that are applicable to zonal jets, and so this work inherently ignores mechanisms associated with zonal asymmetries, such as land-sea contrast and their associated stationary waves.

Jet stream dynamics research over the last decade suggests that an equatorward shift and weakening of the eddy-driven jet could result in an increase in jet positional variability (e.g. Kidston and Gerber 2010; Barnes et al. 2010; Woollings et al. 2018). Using a barotropic model with stirring representing eddy forcing, Barnes and Hartmann (2011) showed that jets closer to the equator have greater positional variability than jets placed closer to the pole. This is in keeping with research showing the sensitivity of jet stream dynamics to jet latitude (e.g. Kidston and Gerber 2010; Kidston and Vallis 2010, 2012; Garfinkel et al. 2013; Barnes and Polvani 2013; Burrows and Chen 2017). Additionally, Woollings et al. (2018) showed that a weaker jet is also related to higher positional variability. The mechanisms described in these papers are rooted in barotropic Rossby wave dynamics. Rossby waves are tightly coupled to the jet stream's variability: Rossby wave breaking affects both jet position and speed through their eddy momentum transport (e.g. Thompson 1980; Robinson 2006). When a jet is further poleward, wave breaking on the poleward flank is suppressed due to Earth's sphericity, minimizing the deposition of momentum and thereby decreasing jet positional variability (e.g. Barnes et al. 2010). When a jet strengthens, Rossby waves can become trapped near the jet core, also decreasing Rossby wave breaking and associated jet variability (Hoskins and Ambrizzi 1993; Woollings et al. 2018). Given the simulated response of the eddy-driven jet to Arctic amplification and sea ice loss, we may expect the resulting jet to be closer to the equator and weaker, and thus have greater positional variability according to these mechanisms.

In this work, we first highlight results from a fully coupled general circulation model (GCM), namely, how both the mean state and, more importantly, the variability of the eddy-driven jet responds to sea ice loss. From there, we work down the model hierarchy to a barotropic model, which we use to examine one possible barotropic mechanism at play in the jet stream response to Arctic amplification and sea ice loss. Previous studies have shown that the atmospheric circulation can be recreated surprisingly well using only barotropic theory, and barotropic models have been used extensively in studies of the jet and its response to external forcing (e.g. Vallis et al. 2004; Kidston and Vallis 2010; Barnes et al. 2010; Kidston and Vallis 2012). Our results indicate that even when there is an apparent equatorward shift and weakening of the jet in response to sea ice loss and

Arctic amplification, jet positional variability decreases, rather than increases, as one might expect from previous studies. We explain this decrease in jet positional variability via changes in Rossby wave propagation. We place this work in the context of past studies relating the response of the midlatitude circulation to sea ice loss/Arctic amplification to the annular modes.

It is important to note that our chosen metric does not quantify the meandering of the jet stream over space, that is, the waviness of the flow, but rather, quantifies the zonal-mean jet position over time. Further, our idealized experiments contain no topography and therefore neglect stationary wave mechanisms, previously discussed in the literature as critical for the atmospheric response to sea ice loss (e.g. Petoukhov and Semenov 2010; Sun et al. 2015; Wu and Smith 2016). This highlights that the mechanism which we are proposing, which relies solely on the horizontal propagation of synoptic scale waves, is one of many.

2.2 MODELS

2.2.1 CCSM4

To assess how sea ice loss may impact eddy-driven jet variability, we first analyze experiments run with a fully coupled GCM. Monthly results from a set of sea ice loss experiments run by Deser et al. (2015) (hereafter $D15$) using the Community Climate System Model version 4 (CCSM4) were made available. CCSM4 is a fully coupled GCM with a horizontal resolution of 0.90^{o} latitude and 1.25^{o} longitude, 26 vertical levels, and a full oceanic component. The specifics of the experiments can be found in $D15$, but we include relevant details here for reference. The seasonal cycle of Arctic sea ice is artificially controlled in order to match an ensemble mean of six CCSM4 historical runs over the period 1980-1999 for the control simulation (*CONTROL*), and six CCSM4 RCP8.5 simulations for the period 2080-2099 for the experiment simulation (*LOWICE*). The radiative forcing conditions for both simulations are constant, with values taken from the year 2000. What differentiates *CONTROL* and *LOWICE*, however, is that an additional longwave radiative flux is prescribed only to the ice model component in the *LOWICE* simulation, with values chosen so that the resulting sea ice loss is similar to that seen in the 2080-2099 CCSM4 RCP8.5 ensemble mean. This flux is spatially invariant with a seasonal dependence (see appendix of $D15$ for more

details). Both simulations are then run for 360 years, with the first 100 years removed for spin-up of the Atlantic meridional overturning circulation. The data is saved at a monthly time resolution, giving us 260 years of monthly zonal wind data from each experiment.

2.2.2 Dry dynamical core model

Next, we step down the model hierarchy to a much simpler model, namely a dry dynamical core with no topography. Here, we analyze the response of jet stream variability to an imposed polar thermal forcing, which mimics the Arctic amplification signal. We use the Geophysical Fluid Dynamics Laboratory (GFDL) spectral dry dynamical core model, which is run with the Held and Suarez (1994) physics, using T63 resolution, 40 vertical levels, 900s timesteps, and no topography (Hassanzadeh and Kuang 2016). This basic state set-up comprises the control simulation (*CTRL*) and is run for 15,000 days under perpetual equinox conditions. The data is saved in zonal averages, and the first 500 days are discarded for spin-up, giving us 14,500 days of 6-hourly measurements of zonal-mean wind fields for our analysis. In order to simulate the low-level polar warming associated with sea ice loss and Arctic amplification, a zonally symmetric Gaussian thermal forcing is applied at the 1000 hPa pressure level (standard deviation of 250 hPa) at both 90^{o}N and 90^{o}S (standard deviation of 16^o latitude). The amplitude of the heating is equal to 1.0 K day^{-1}. This forcing is identical to the one used in POLAR experiment in McGraw and Barnes (2016), with the exception that the polar heating is applied here to both hemispheres. The Arctic amplification simulation (*AAMP*) branches off of the *CTRL* and is run for another 15,000 days, and again, the first 500 days are discarded. We calculate the daily mean values for the 14,500 days from both simulations, and consider the hemispheres to be independent, allowing for doubling of the data. This gives us 29,000 daily mean, zonal-mean, zonal wind values for each experiment.

2.2.3 Barotropic Model

The barotropic model is one of the simplest in the atmospheric model hierarchy (Shaw et al. 2016), giving us an ideal framework in which to analyze Rossby wave dynamics and the eddy-driven jet. We use an initial model set-up identical to that of Vallis et al. (2004), where the non-divergent vorticity equation is integrated on the sphere:

$$\frac{\delta \zeta}{\delta t} + J(\psi, \zeta + f) = S - r\zeta + \kappa \nabla^4 \zeta \tag{2.1}$$

The Lagrangian change in absolute vorticity, defined as relative vorticity, ζ, plus the planetary vorticity, f, is balanced by a parameterized representation of the baroclinic eddies that stir the barotropic flow, S, plus a damping term $r\zeta$, with damping parameter r, and diffusion ($\kappa\nabla^4\zeta$). Values for S, r and κ are identical to those used in Barnes et al. (2010). Additionally, following Vallis et al. (2004), we impose a Gaussian spatial mask, i.e. the global stirring field is multiplied by a Gaussian curve which damps the stirring away from a chosen central latitude, ϕ_s, with a specified standard deviation, σ_s. For all simulations the value of σ_s remains unchanged at 12^o. All other parameters of the model follow Vallis et al. (2004), with a resolution of T42 and a time step of 3600 seconds. Each simulation is spun up for 100 days and run an additional 32,000 days for analysis.

The single-layer barotropic model is interpreted to represent a vertical integration of the atmosphere, thus, any forcing represented within the model must not be surface-constrained. In order to approximate a sea ice loss forcing in this model we assume that the initial, localized zonal wind response to the sea ice loss then forces a remote zonal wind response. Previous studies, as well as our own analysis of the CCSM4 and dry dynamical core models discussed above, have shown that the most consistent response of the mean jet to sea ice loss and Arctic amplification is anomalous easterlies on the poleward flank of the jet. This results from the locally weakened temperature gradients along the climatological sea ice edge, and is thus a surface-driven response that extends throughout the depth of the troposphere (see high latitude blue shading in Fig. A.1 in Appendix A). Previous work by Deser et al. (2007) showed a robust response in geopotential heights at 300 hPa to Arctic sea ice loss within five days, suggesting that this vertical extension of the easterly

wind anomalies is at least partly the initial response. Thus, these easterly wind anomalies can be represented within the single-layer barotropic model, as they are not constrained to the surface.

We assume that the initial response to the surface forcing is a barotropic, easterly zonal wind anomaly at high latitudes, and that the midlatitudes respond in turn to the forcing by the zonal wind anomalies. In order to approximate the results from this forcing in a barotropic model, we run a variety of simulations with an additional angular momentum forcing term applied on the poleward flank of the stirred jet, similar to that used by Ring and Plumb (2007), and later by Barnes and Thompson (2014). This angular momentum forcing acts as an easterly torque on the flow, affecting the tendency of the winds at every time step. The easterly torque is Gaussian in latitude, centered at latitude ϕ_f with a standard deviation of σ_f= 8^o. By setting the amplitude of the forcing to be negative it acts as an easterly torque. We set ϕ_f to be poleward of ϕ_s, thus giving us a representation of the easterly forcing from both sea ice loss and Arctic amplification, as seen in the CCSM4 and the dry dynamical core results, respectively.

The first set of experiments consists of a control simulation (*NoTRQ*) with the forcing turned off and the stirring latitude placed at ϕ_s=35^{o}N. The experimental simulation (*TRQ10*) has stirring placed at the same latitude, and an easterly torque located at ϕ_f=55^{o}N, with an amplitude of -1.0 ms^{-1}day^{-1}. The distance of 20^o between ϕ_s and ϕ_f is motivated by the climatological jet profiles from the CCSM4 and the dry dynamical core, where it represents the distance from jet core to where the zonal wind goes to zero on the poleward flank. The changes in jet variability from this set of barotropic model experiments is used to compare directly to the results from the CCSM4 and the dry dynamical core. In addition, we also run another control simulation, *NoTRQ33*, with no easterly torque and the stirring placed at ϕ_s=33^{o}N. This is done to simulate a very small equatorward shift, found when comparing *TRQ10* with *NoTRQ*, in order to isolate the impact of changing the latitude of wave generation.

The next two sets of barotropic model experiments are composed of a suite of simulations, one with varying torque amplitudes, with ϕ_f and ϕ_s held constant, and the other with varying stirring latitude, ϕ_s, while the easterly torque remains constant and fixed in latitude.

(1) *VaryAmp*: This set of simulations is run with varying torque amplitudes, with an easterly torque, from -0.2 to -2.0 $ms^{-1}day^{-1}$, and a westerly torque, from 0.2 to 2.0 $ms^{-1}day^{-1}$. Both the stirring and torque latitudes remain fixed, with ϕ_s=35°N and ϕ_f=55°N.

(2) *VaryStir*: In this set of simulations, the torque latitude and amplitude are set at the same conditions as *TRQ10*, with ϕ_f=55°N and torque amplitude of -1.0 $ms^{-1}day^{-1}$. However, the stirring latitude ϕ_s is increased by 5°N from the equator to 50°N. Thus, for each individual simulation, there is a new control run with the same ϕ_s and no forcing.

2.3 METHODS

2.3.1 Defining the jet

The primary focus of this work is on the impacts of sea ice loss on eddy-driven jet variability. CCSM4 includes full topography, therefore the storm tracks occur primarily over the ocean basins, where the eddy-driven jets are strongest and have the greatest flow variability (e.g. Blackmon 1976; Hoskins and Valdes 1990; Woollings et al. 2010). Motivated by previous studies examining the response of the North Atlantic jet stream, we restrict our analysis to the North Atlantic basin (0-70°W), whose leading mode of variability has been referred to as a “wobble" in meridional position (e.g. Wittman et al. 2005). Using the 850 hPa zonal winds as representative of the eddy-driven jet (Woollings et al. 2018), and looking only at boreal winter (January-March; JFM), we take both a zonal and seasonal mean across the basin. The seasonal mean provides additional smoothing of the data, and results in 260 seasonal mean jet profiles. Results and conclusions resulting from analysis of three definitions of winter season (December-March, December-February, and January-March) were very similar, therefore we chose JFM so as utilize all 260 years of data. The latitude and magnitude of the seasonal mean maximum zonal-mean zonal winds, i.e. jet position and speed, is identified for each year (Woollings et al. 2010; McGraw and Barnes 2016), with a northerly limit of 75°N. The climatological jet profiles from both simulations are plotted in Fig. 2.1.

In the dry dynamical core experiment, topography was not included in order to examine the zonally symmetric response to polar thermal forcing. Here, the 775 hPa zonal winds are considered to be representative of the eddy-driven jet (McGraw and Barnes 2016). Again, the zonal-mean of

the zonal winds is calculated, and the 29,000 daily mean jet positions and speeds are identified for *CTRL* and *AAMP*. The climatological jet profiles for both simulations are shown in Fig. 2.4.
Finally, in the barotropic model there is no topography and no vertical levels. Taking the zonal-mean of the zonal winds, we again identify the 32,000 daily maximum wind latitudes and magnitudes for *NoTRQ*, *TRQ10*, and all of the simulations within the *VaryAmp* and *VaryStir* experiments. The climatological jet profiles of *NoTRQ* and *TRQ10* are plotted in Fig. 2.7.

2.3.2 Quantifying jet variability

Our focus here is on quantifying changes in jet variability in response to sea ice loss and Arctic amplification. To do this, we plot the distributions of the jet speeds and positions identified in each of the following model experiments: CCSM4 *CONTROL* vs. *LOWICE* (Fig. 2.2), dry dynamical core *CTRL* vs. *AAMP* (Fig. 2.5), and the barotropic model *NoTRQ* vs. *TRQ10* (Fig. 2.8). We assess changes in variability by comparing the standard deviations of each simulation's distribution to their respective control simulations. The distributions are smoothed for plotting using a Gaussian kernel function, where the bandwidth was chosen to be as small as possible in order to remove the noise while still retaining the important features of the distributions. The CCSM4 bandwidth is 0.4 for both jet speeds and positions, while the dry dynamical core and the barotropic models use 0.2 for the position distributions and 0.1 for the speed. The standard deviation of each distribution is included in the legends of each figure, and the value is bolded if it is significantly different from the control at confidence level greater than 95% (one-sided variance F-test).

2.3.3 Refractive Index

Interactions between the mean flow and synoptic-scale eddies greatly impact jet stream variability. This interaction is essentially rooted in Rossby wave propagation and the associated momentum fluxes, particularly with regards to the convergence of westerly momentum in the jet core

via Rossby wave breaking on its flanks. We map out the wave breaking associated with a certain climatological jet profile using the refractive index, K^* (see equation 3.2; Hoskins and Karoly 1981).

$$K^* = cos(\phi)\sqrt{\frac{\hat{\beta}}{\bar{u}-c}}, \quad \text{and} \quad K^{*2} = k^2 + l^2, \tag{2.2}$$

where k and l are the zonal and meridional wavenumbers, respectively. $\hat{\beta}$ is the meridional gradient of absolute vorticity, $\bar{u}$ is the zonal-mean zonal wind, and c is the phase speed (Hoskins and Karoly 1981; Barnes et al. 2010). The additional factor of $cos(\phi)$ accounts for the fact that the specific wavelength associated with a zonal wavenumber k decreases with latitude (Barnes and Hartmann 2012). As long as the zonal wavenumber, k, is smaller than K^* the waves may propagate freely. Once $k = K^*$ (i.e. $l = 0$; Hoskins and Karoly 1981) the waves are reflected, or if K^* gets very large the waves break (Barnes et al. 2010; Barnes and Hartmann 2012). The refractive index in (3.2) can then be used to calculate the reflective and critical latitudes, which are the two distinct limits mentioned above (Lorenz 2014a,b, 2015). Rossby waves created within the jet core propagate away from their source region until they meet one of these two latitudes (e.g. Hoskins and Karoly 1981; Hartmann 2007; Barnes et al. 2010). When $k = K^*$ the waves turn without breaking (reflective latitude). When K^* instead goes to infinity the waves break (critical latitude) and deposit easterly momentum. In the linear limit, both refractive latitudes (critical and reflective) depend upon the upper-level zonal winds and wave phase speeds, however the reflective latitude has an additional dependence on wavelength and the vorticity gradient, as given by $\hat{\beta}$ for midlatitude, tropospheric Rossby waves in (3.2) (e.g. Hoskins and Karoly 1981).

Both the reflective and the critical latitudes contribute to variability in jet position and speed through their impact on wave propagation (e.g. Benedict et al. 2004; Woollings et al. 2008; Lorenz 2014a; Woollings et al. 2018). These refractive latitudes depend on the zonal wind profile (see equation 3.2; Barnes et al. 2010), and therefore will be affected by changes in the zonal-mean zonal wind in response to an external forcing, such as sea ice loss and Arctic amplification. Changes in the refractive latitude profiles, in turn, impact jet variability by adjusting the local Rossby wave propagation (e.g. Kidston and Gerber 2010; Barnes et al. 2010).

It is important to note that K^* is based on linear assumptions and does not distinguish between

irreversible wave breaking and other processes (such as wave absorption and reversible wave breaking). However, it was demonstrated by Barnes and Hartmann (2012, see their Figure 4) to be an approximate measurement of where waves preferentially break, as well as providing appropriate wave breaking limits away from the jet core.

For the purposes of this work we analyze changes in both the critical and reflective latitudes in each model experiment. Tropospheric Rossby wave breaking occurs predominantly at upper levels, with the momentum transfer also impacting the lower-level eddy-driven jet (Robinson 2006; Hartmann 2007). Therefore, in order to calculate the two refractive latitude profiles derived from K^*, we use the 300 hPa level zonal-mean zonal winds for both the CCSM4 and dry dynamical core model, while for the barotropic model we continue to use the zonal-mean zonal wind field. For the reflective level, we look at a range of zonal wavenumbers within the Rossby wave spectrum, i.e. synoptic wavenumbers (generally defined as $k \geq 4$; Hoskins and Karoly 1981). In order to easily compare the simulations from each experiment we define a simple metric, the wave propagation width, which is the distance between the critical latitudes on either side of the jet core, i.e. the maximum distance a wave may travel out of the jet core, both poleward and equatorward, before breaking. If one flank of the jet has a reflective latitude placed closer to the jet, then the waves are turned back and we calculate the wave propagation width as twice the distance to the critical latitude on the other flank. If, on both flanks, waves of a certain phase speed only encounter reflective latitudes then we define wave propagation width as being zero.

2.4 RESULTS

While the key insights of this study revolve around the barotropic model experiments, we initially motivate these results and model setup by analyzing changes in jet variability in CCSM4 and dry dynamical core model.

2.4.1 CCSM4

Focusing on the boreal winter (JFM), we examine the impact of sea ice loss on the North Atlantic eddy-driven jet in the CCSM4, a fully coupled GCM. We start by looking at changes in the

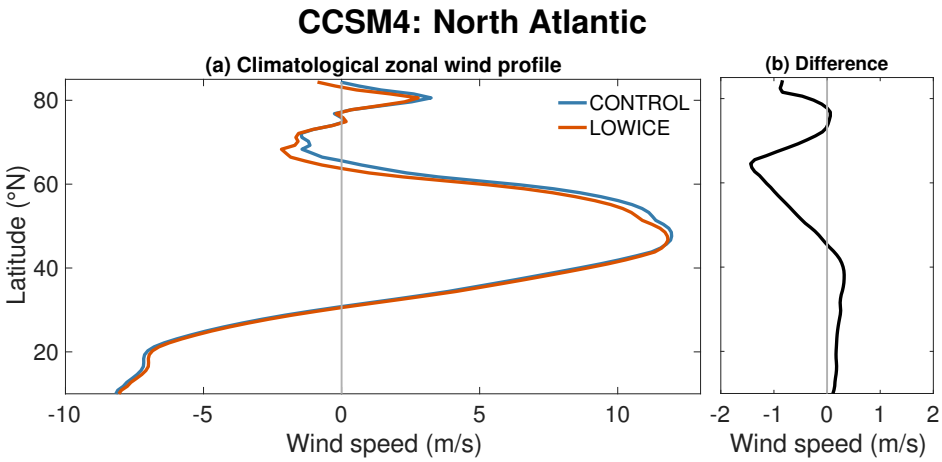

Fig. 2.1. The North Atlantic January-March seasonal mean (a) 850 hPa zonal-mean zonal wind profiles and (b) corresponding zonal-mean wind anomalies. The CCSM4 control simulation (*CONTROL*) is shown in blue and the sea ice loss experiment (*LOWICE*) in red.

climatological zonal-mean zonal wind profile over the North Atlantic basin (Fig. 2.1). Fig. 2.1a shows both the *CONTROL* (blue) and *LOWICE* (red) wind profiles, while Fig. 2.1b shows the anomalies, defined as *LOWICE*-*CONTROL*. While we do see the expected changes (a small decrease in wind speeds within the jet core and a very slight equatorward shift), the clearest response is in the anomalous easterlies on the poleward flank of the jet and little to no change on the equatorward flank, causing a narrowing of the jet profile and an enhancement of the pre-existing easterlies.

The distributions of seasonal mean jet position and speed give us an objective way to evaluate any changes in variability, as demonstrated in Fig. 2.2. The distributions have been centered around their respective means so as to make visual comparison easier between *CONTROL* (blue) and *LOWICE* (red). When sea ice declines, the jet position distributions narrows, with the biggest fractional changes occurring in the tails (Fig. 2.2a): in *LOWICE*, the seasonal mean jet position remains relatively close to its climatological position, corresponding to lower jet positional variability. This decrease in variability is corroborated by the significant decrease in standard deviations of jet position in both basins (noted in the legends), at a confidence level of 95%. There is essentially no change in the distribution of jet speeds (Fig. 2.2b).

To summarize, in the fully coupled GCM the main change in the North Atlantic mean state is an asymmetrical narrowing of the jet due to anomalous easterlies on the poleward flank, and

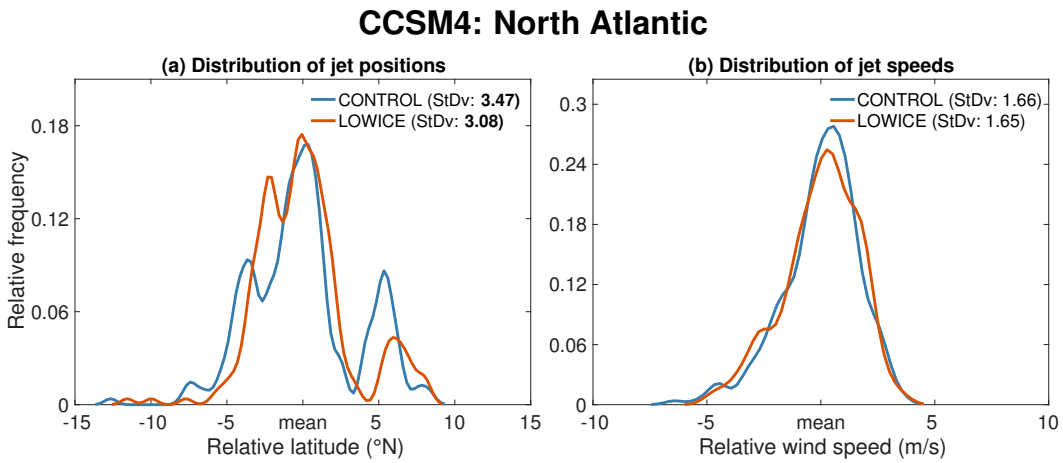

Fig. 2.2. Distribution of North Atlantic January-March seasonal mean (a) jet positions and (b) jet speeds. All distributions are centered on their mean value. The CCSM4 control simulation (*CONTROL*) is shown in blue and the sea ice loss experiment (*LOWICE*) in red. Distributions are smoothed using a kernel method, and standard deviations of each distribution are included in the legends. Standard deviations that are significantly different between the two simulations are printed in bold. See Methods for more details.

decreasing jet variability, as quantified by the jet position variance. These two results may both be explained by Rossby wave breaking (Lorenz 2015; Woollings et al. 2018). As stated previously in the Methods section, from linear theory, the determining factor for wave breaking is the latitude where the phase speed, c, is equal to the upper-level zonal wind, $\bar{u}$, i.e. the critical latitude (see Eq. 3.2). Therefore, if the mean zonal wind profile changes throughout the column, so too will the latitude of Rossby wave breaking. Additionally, if there are any changes in absolute vorticity, either through wind shear changes (relative vorticity) or changes in mean jet position (planetary vorticity) this can also lead to changes in K^* and therefore changes in the reflective latitude, where $k = K^*$.

In Fig. 2.3, we examine the zonal profiles of both critical and reflective latitudes for the upper-level jet for wavenumber $k = 3$ waves and measure the change in wave propagation width between *LOWICE* (red) and *CONTROL* (blue). This wavenumber was chosen as representative of the results for analyses conducted on a large range of $k = 2-10$. This range was based, in part, on Figure 3 of Randel and Held (1991), which showed the power of the Northern Hemisphere December-March transient eddies as a function of both phase speed and wavenumber. They showed that hemisphere-wide power is concentrated in phase speed range $c = 0-18$ ms^{-1} and wavenumbers $k = 3-9$. The

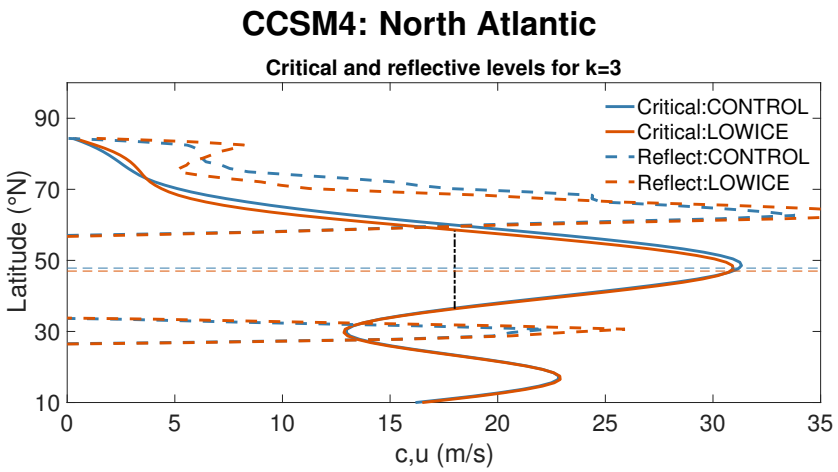

Fig. 2.3. The North Atlantic critical (reflective) level profiles at 300 hPa in solid (dashed) for wavenumber $k = 3$. The CCSM4 control simulation (*CONTROL*) is shown in blue and the sea ice loss experiment (*LOWICE*) in red. The mean 850 hPa jet position is indicated by the thin dashed lines. The thin, black vertical line represents the wave propagation width for a wave with phase speed $c = 18\text{ms}^{-1}$ in the *LOWICE* run.

thin, vertical, black line included in our Fig. 2.3 is a visual representation of the wave propagation width for waves of $k = 3$ and $c = 18$ ms^{-1} for the *LOWICE* run. If the wave propagation width decreases in the *LOWICE* simulation, then the ability for waves to travel out of the jet core and influence the jet position via the depositing of easterly momentum on the flanks will be limited. That is, a narrowing of the jet can decrease the distance Rossby waves may propagate before breaking or reflecting. Similar to previous arguments of how Rossby wave propagation impacts jet speed and position (e.g. Barnes et al. 2010; Barnes and Hartmann 2011, 2012), the limitation on wave propagation distance means a decrease of eddy momentum flux convergence on the flanks of the jet, outside of the jet core. This would imply greater persistence of the jet at its current latitude, restricting its ability to shift, thus ultimately leading to a decreased latitude range of jet position. Upon examination of Fig. 2.3 we see a narrowing of the wave propagation width in response to sea ice loss.

The difference in wave propagation width from *CONTROL* to *LOWICE* was also measured for phase speeds $c = 5-30$ ms^{-1} at wavenumbers $k = 2-10$ (not shown). While there are a few wavenumber/phase speed combinations where the wave propragation width increases due to a switch from reflective to critical latitudes being felt, the general conclusion of **decreased wave propagation width** in the *LOWICE* simulation is consistent across most wavenumbers.

Based on previous studies linking changes in both the mean-state and the variability of the eddy-driven jet with the barotropic mode of Rossby wave breaking (e.g. Barnes et al. 2010; Barnes and Hartmann 2011, 2012; Woollings et al. 2018), we propose a barotropic mechanism linking our two main results: the decreased wave propagation width and the decreased jet positional variability. This mechanism, which will be further explored and tested in subsequent sections, can be summarized by the following for the CCSM4 experiment results:

(1) Anomalous easterlies on the poleward flank of the jet leads to a narrowing of the jet profile.

(2) This narrowing results in a decrease in wave propagation width across most Rossby wavenumbers and phase speeds.

(3) The decreased wave propagation width limits the jet's positional variability, as Rossby waves break closer to the jet core, leading to the significantly decreased standard deviations seen in the jet position distributions.

This barotropic mechanism implies that the response will be felt by jet position variability, rather than jet speed variability. It has been previously stated that jet speed variability is dependent on the mean jet speed itself (e.g. Klink 1999; May and Bourassa 2011), making it possible that any changes we see in jet speed variability may be entirely due to the change in mean jet speed. To that end, we will primarily focus on the jet positional variance for the rest of this article. However, we will continue to show the jet speed distributions for completeness as they result directly from our jet position calculations.

2.4.2 Dry dynamical core model

Our findings from the fully coupled GCM suggest a possible barotropic mechanism for decreased jet positional variability through changes in Rossby wave propagation. We next use the results from the GFDL dry dynamical core Arctic amplification experiment to further explore our hypothesis. We compare the 29,000 daily zonal-mean zonal wind data from the Arctic amplification simulation (*AAMP*) to that of the control simulation (*CTRL*).

Beginning once more with the climatological profiles (Fig. 2.4), we immediately see simi-

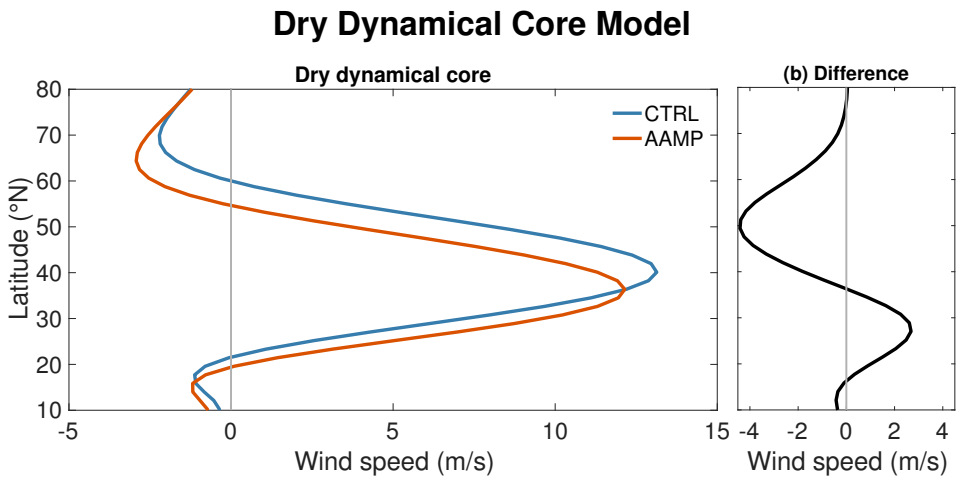

Fig. 2.4. (a) The 750 hPa zonal-mean zonal wind profiles for the dry dynamical core model control simulation (*CTRL*; blue) and the polar heating experiment (*AAMP*; red). (b) The corresponding zonal wind response anomaly.

larities to the CCSM4 North Atlantic jet results, with the biggest response being the anomalous easterlies on the poleward flank. This results in a narrowing of the jet profile and, therefore, our mechanism would suggest a decrease in jet position variability. In addition to the narrowing, however, the difference in the temporal mean zonal-mean zonal wind profiles between *AAMP* (red) and *CTRL* (blue) also shows a clear equatorward shift and slowing down of the jet. An equatorward shift of the jet profile could be linked with increased jet position variability (Barnes et al. 2010; Barnes and Hartmann 2011), as could the decreased jet speed (Woollings et al. 2018). While this would indicate competing dynamical effects, it is important to note that the results from Barnes and Hartmann (2011) do not extend further south than 35° N, and Woollings et al. (2018) are looking at internal variability, not changes in internal variability in response to an external forcing. Thus, the results from these two studies may not truly represent a dynamical competition to our proposed mechanism.

To quantify the change in jet variability, we again look at the change in standard deviation of the distributions of daily mean jet positions and speeds from *CTRL* and *AAMP*. Both jet speed and position distributions narrow and show significantly decreased variability, this time at over 99% confidence (Fig. 2.5). The decrease in jet position variance is consistent with the response seen in the CCSM4 results, and suggests that the narrowing of the jet profile is of greater significance than the small equatorward shift. The significant decrease in jet speed variability could suggest that it

is not only the jet position which is impacted by a narrowing of the jet, or it could be as simple as weaker winds have less variance.

Since we see decreased jet positional variability between *AAMP* and *CTRL*, we next analyze

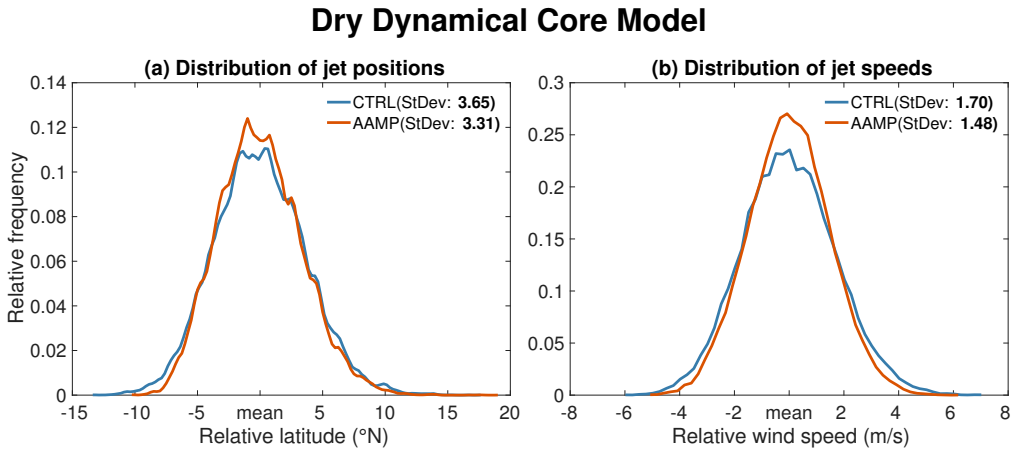

Fig. 2.5. Distributions of daily (a) jet positions and (b) jet speeds in the dry dynamical core model. All distributions are centered on their mean value. The control simulation (*CTRL*) is in blue and the polar heating experiment (*AAMP*) is in red. The standard deviations of each distribution are included in the legends. Standard deviations that are significantly different between the two simulations are printed in bold. See Methods for more details.

the refractive latitudes from each simulation, in order to determine if there is a decrease in the wave propagation width. Fig. 2.6 shows the changes in the critical and reflective latitudes,where we plot results for wavenumber $k = 4$ (Fig. 2.6a) and $k = 6$ (Fig. 2.6b), in order to demonstrate the robustness of our conclusions with the zonal wavenumber range of interest, $k = 4-10$. This specific range was found to have the most power in the barotropic model results, and was also chosen for the dry dynamical core, since neither contains topography and thus have little to no power at wavenumbers less than $k = 4$. Fig. 2.6 also includes thin, vertical, black lines representing the wave propagation width of a wave of (a) $k = 4$ and $c = 15$ ms^{-1}, and (b) $k = 6$ and $c = 18$ ms^{-1}.

For wavenumber $k = 4$, we find decreased wave propagation width for all phase speeds, including those below 10 ms^{-1}, which encounter a reflective latitude on the poleward flank. This is also true for wavenumber $k = 6$, except for phase speeds of less than about 3 ms^{-1} for *AAMP* and about 5 ms^{-1} for *CTRL*. For slower moving waves at synoptic scales it appears the waves cannot exit the jet core, essentially remaining trapped with a wave propagation width of zero.

The results from the dry dynamical core further support the hypothesis that an impact of sea

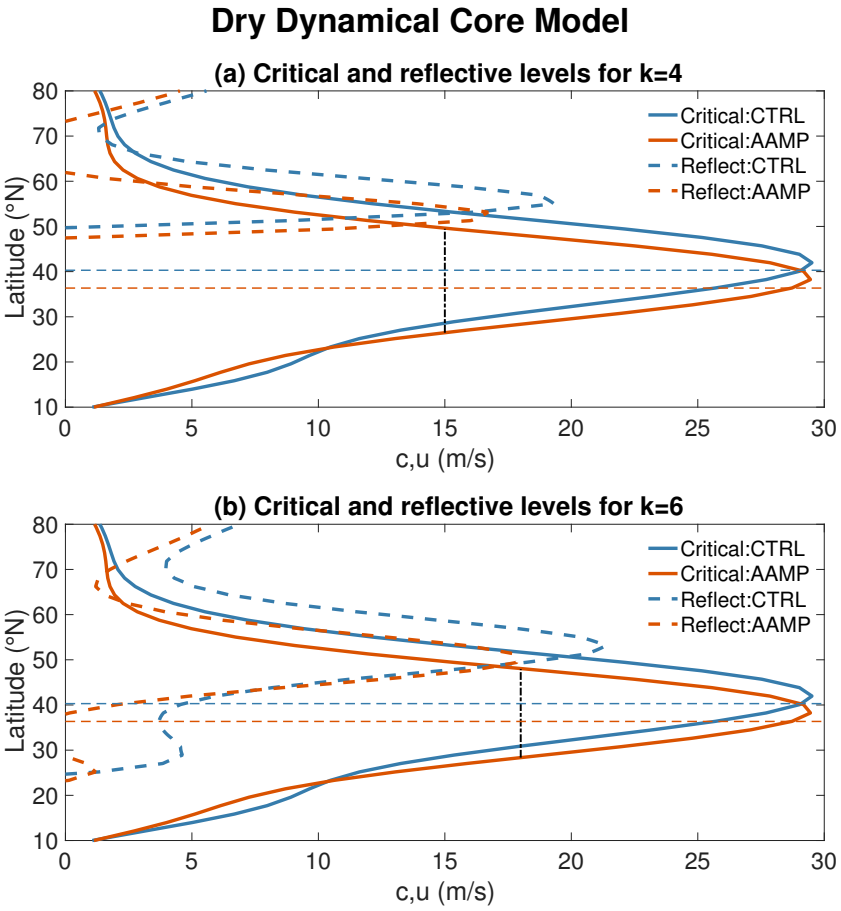

Fig. 2.6. Critical (reflective) level profiles at 300 hPa in heavy solid (dashed) for wavenumbers (a) $k = 4$, and (b) $k = 6$. The control simulation (*CTRL*) is in blue and the polar heating experiment (*AAMP*) is in red. The 775 hPa mean jet position is indicated by the thin dashed lines. The thin, vertical, black line represents the wave propagation width in the *AAMP* run for phase speeds (a) $c = 15$ ms^{-1}, and (b) $c = 18$ ms^{-1}.

ice loss and Arctic amplification on the eddy-driven jet may be decreased variability due to a narrowing of the jet and restricted Rossby wave propagation.

2.4.3 Barotropic Model

2.4.3.1 *TRQ10*

Based on the consistent anomalous easterly response on the poleward flank of the jet to sea ice loss (CCSM4) and polar heating (dry dynamical core), we represent the direct effect of sea ice loss and Arctic amplification as an easterly torque poleward of the jet core in the barotropic model. The set of experiments we show in Fig. 2.7, Fig. 2.8 and Fig. 2.9 use stirring placed at 35°N, and easterly torque placed at 55°N with an amplitude of -1.0 ms^{-1}day^{-1}. A range of torque amplitudes

will be explored further on.

The zonal-mean zonal wind response seen in Fig. 2.7 consists mainly of a narrowing of the

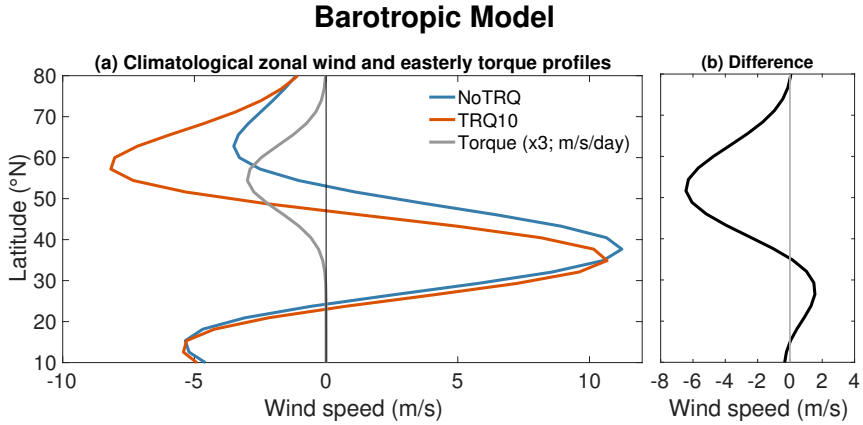

Fig. 2.7. (a) The zonal-mean zonal wind profiles for the barotropic model control simulation (*NoTRQ*; blue) and the easterly torque experiment (*TRQ10*; red), as well as a profile of the applied torque multiplied by 3 to aid comparison (Torque; grey). (b) The corresponding zonal wind response anomaly between *TRQ10* and *NoTRQ*. The stirring is located at 35°N, and the torque at 55°N with an amplitude of 1.0 $ms^{-1}day^{-1}$.

jet due to the imposed easterly torque. This narrowing causes the position of maximum winds to shift slightly equatorward. However, there is no true displacement of the entire jet profile,since the shift of the maximum westerlies is caused by asymmetrical narrowing on the poleward flank. There is also a decrease in maximum wind speed, similar to the results seen in both the CCSM4 North Atlantic basin and the dry core experiment.

In order to quantify the change in jet variability we compare distributions of the 32,000 daily jet positions and speeds for *TRQ10* (red) and *NoTRQ* (blue; Fig. 2.8). These distributions show a similar story as the dry core, with significant decreases in the standard deviation of both jet speed and position at more than 99% confidence. The narrowing of the distributions is most evident at the tails. Therefore, we have very similar results to those seen in both the dry dynamical core and CCSM4, with an asymmetrical narrowing of the jet on the poleward flank, very little change on the equatorward flank, and significantly decreased jet position variability in response to an easterly torque.

The transient eddy momentum flux has little power at planetary wave scales within the barotropic model, therefore the range chosen for this portion of the analysis is $k = 4-10$, the same as in the dry dynamical core model. For the barotropic model we chose wavenumbers $k = 4$

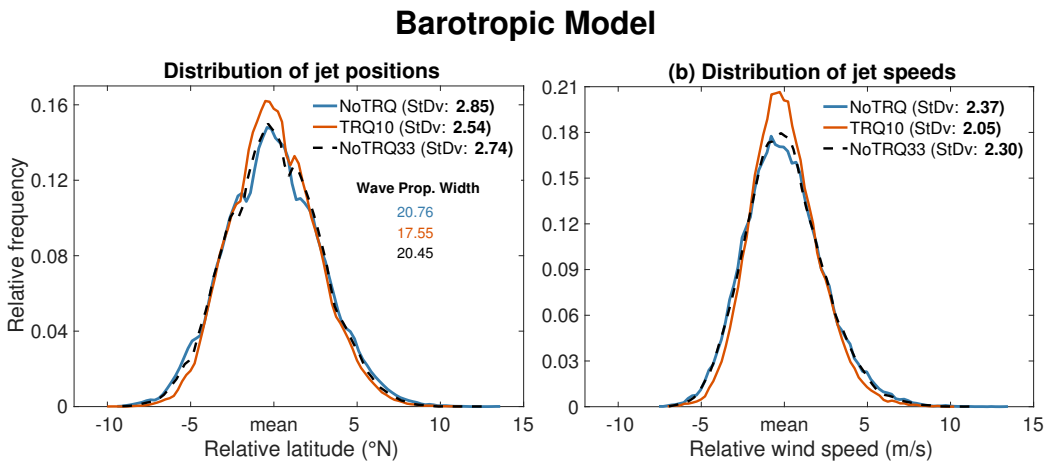

Fig. 2.8. Distributions of (a) jet positions and (b) jet speeds in the barotropic model for stirring located at 35°N and torque at 55°N with an amplitude of -1.0 $ms^{-1}day^{-1}$. The control simulation (*NoTRQ*) is in blue and the easterly torque experiment (*TRQ10*) is in red, while another control simulation, *NoTRQ33*, is shown in black dashed. The standard deviations of each distribution are included in the legends. Standard deviations that are significantly different between the all three simulations are printed in bold. The wave propagation widths for a wave with wavenumber $k = 4$ and phase speed $c = 4$ ms^{-1} are included below the legend, the colors of each corresponding to the distributions. See Methods for more details.

and $k = 8$ as our representative examples. Again, the conclusions are consistent across a range of wavenumbers ($k = 4-10$) and phase speeds ($c = 0-10$ ms^{-1}). The critical (solid) and reflective (dashed) latitude profiles for waves of wavenumber $k = 4$ are shown in Fig. 2.9a, and wavenumber $k = 8$ in Fig. 2.9b for both *NoTRQ* (blue) and *TRQ10* (red). The thin, vertical, black lines both represent the wave propagation width for the *TRQ10* run for waves of phase speed $c = 4$ ms^{-1}.

Fig. 2.9a shows that for waves on the bigger end of the synoptic scale and stirring at 35° N, the reflective latitude is not seen by waves, and so the wave propagation width is dictated by the critical latitude alone. This is also true for most phase speeds in Fig. 2.9b, with a zonal wavenumber of $k = 8$. Recall that the critical latitude is defined as when the phase speed is equal to the zonal wind speed, thus, as the jet narrows, the wave propagation width decreases. Again, this is consistent with our proposed theory: the jet narrows due to anomalous easterlies on the poleward flank, which in turn decreases the wave propagation width, decreasing the jet's ability to vary its position as effectively as it had previously.

When looking at the climatological jet profiles in Fig. 2.7, we do see a small equatorward shift of the jet. In order to determine whether this small shift alone may cause changes in jet positional

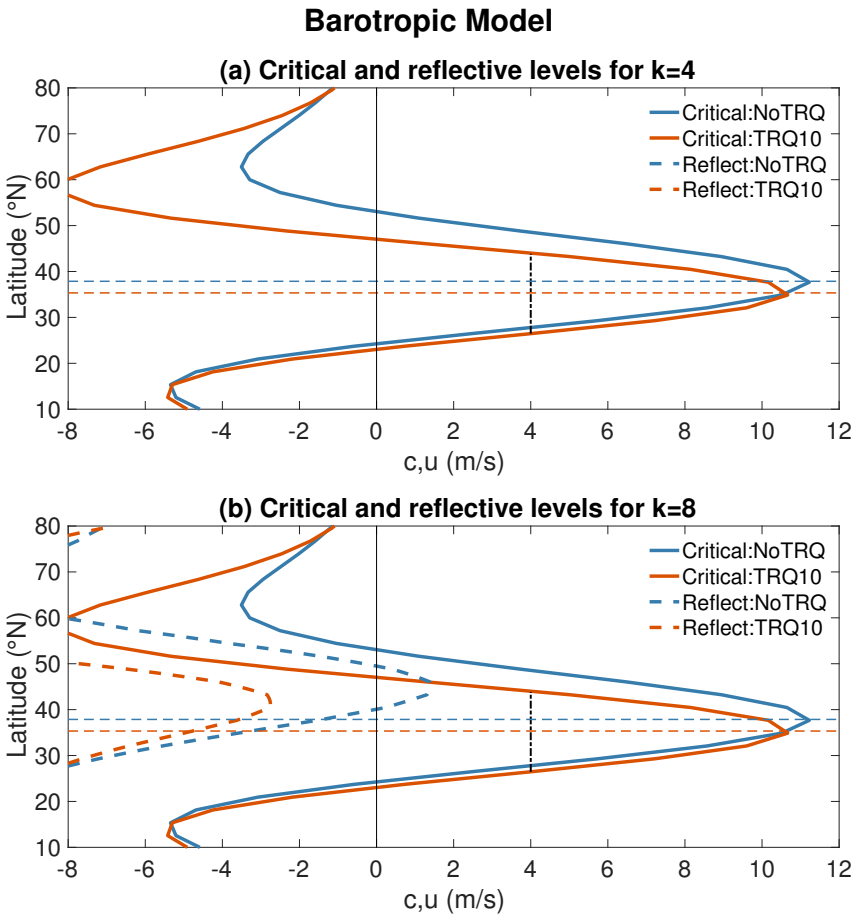

Fig. 2.9. Critical (reflective) level profiles in solid (dashed) for wavenumber (a) $k = 4$, and (b) $k = 8$. The control simulation (*NoTRQ*) is in blue and the easterly torque experiment (*TRQ10*) is in red. The thin, vertical, black lines indicate the wave propagation width for the *TRQ10* experiment at phase speeds $c = 4$ ms^{-1}. The mean jet position is indicated by the thin dashed lines. The stirring is located at 35°N, and the torque at 55°N with an amplitude of -1.0 ms^{-1}day^{-1}.

variability, we include an additional control run, *NoTRQ33*, with stirring at 33°N and no easterly torque. This additional run allows us to analyze the change in jet position and speed distributions resulting from a pure shift of the zonal wind profile alone, i.e. changing the latitude of wave generation, as compared to the changes resulting from the asymmetrical narrowing and subsequent modification of the wave breaking dynamics. The jet positional and speed variability are shown as black dashed lines in Fig. 2.8. The mean jet position of *NoTRQ* is approximately 37.9°N, while both *TRQ10* and *NoTRQ33* are at about 35.5°N, giving us a comparison between simple changes in latitude of wave generation (*NoTRQ33*) versus the additional narrowing by the easterly torque

(*TRQ10*). The variance in jet position for *NoTRQ33* decreases slightly compared to *NoTRQ*, however, we note that the jet positional variability decreases even more in *TRQ10*.

In order to explain this small decrease in jet positional variability when the jet is shifted equatorward, we refer to results from Kidston and Vallis (2010), where it was found that as the stirring in the barotropic model is moved equatorward, the jet profile narrows. This would indicate a decreasing wave propagation width, and is thus consistent with our proposed mechanism. We calculated the wave propagation widths for wavenumber $k = 4$ and phase speed $c = 4$ ms^{-1} for all three simulations, and included them in Fig. 2.8: *NoTRQ* in blue (20.76^{o}), *TRQ10* in red (17.55^{o}) and *NoTRQ33* in black (20.45^{o}). The wave propagation width in *NoTRQ33* is slightly less than in *NoTRQ*, consistent with a narrower jet as described in Kidston and Vallis (2010). However, the values for both wave propagation width and standard deviation of jet position for the *TRQ10* simulation are significantly smaller than in either *NoTRQ* or *NoTRQ33*. This indicates that the significant narrowing on the poleward flank of the jet resulting from the easterly torque appears to contribute to a larger decrease in jet positional variability than can be accounted for by a mere jet shift.

2.4.3.2 *VaryAmp*

An advantage of studying a barotropic model is the ease at which a large variety of experiments can be run. We examine the impact of increasing the easterly torque amplitude from -0.2 to -2.0 ms^{-1}day^{-1} in a suite of simulations (*VaryAmp*), analyzing the changes in jet speed, position, positional standard deviation, and wave propagation width between *VaryAmp* and *NoTRQ* as a function of the easterly torque amplitude (Fig. 2.10). The wave propagation width is calculated for wavenumber $k = 4$ for two phase speeds, $c = 0$ ms^{-1} and $c = 4$ ms^{-1} and is shown in Fig. 2.10b. Fig. 2.10a demonstrates that the mean jet speed (orange) is a weak function of torque amplitude, decreasing slightly with increasing easterly torque. Mean jet position (green) also decreases more as the torque amplitude increases, however this does not represent a displacement of the entire jet profile (as previously discussed). The main impact of the easterly torque is felt on the poleward

flanks, with very little to no change on the equatorward flank, meaning that the equatorward movement of the jet's position is merely an artifact of the asymmetrical narrowing of the jet. This is demonstrated by the decreasing wave propagation widths seen in Fig. 2.10b, which are a strong function of torque amplitude. Consistent with our previous results, the standard deviation of the jet position (purple; Fig. 2.10a) also continues to decrease with increasing easterly torque.

Now we take this a step further: if the narrowing of the jet caused by the easterly torque

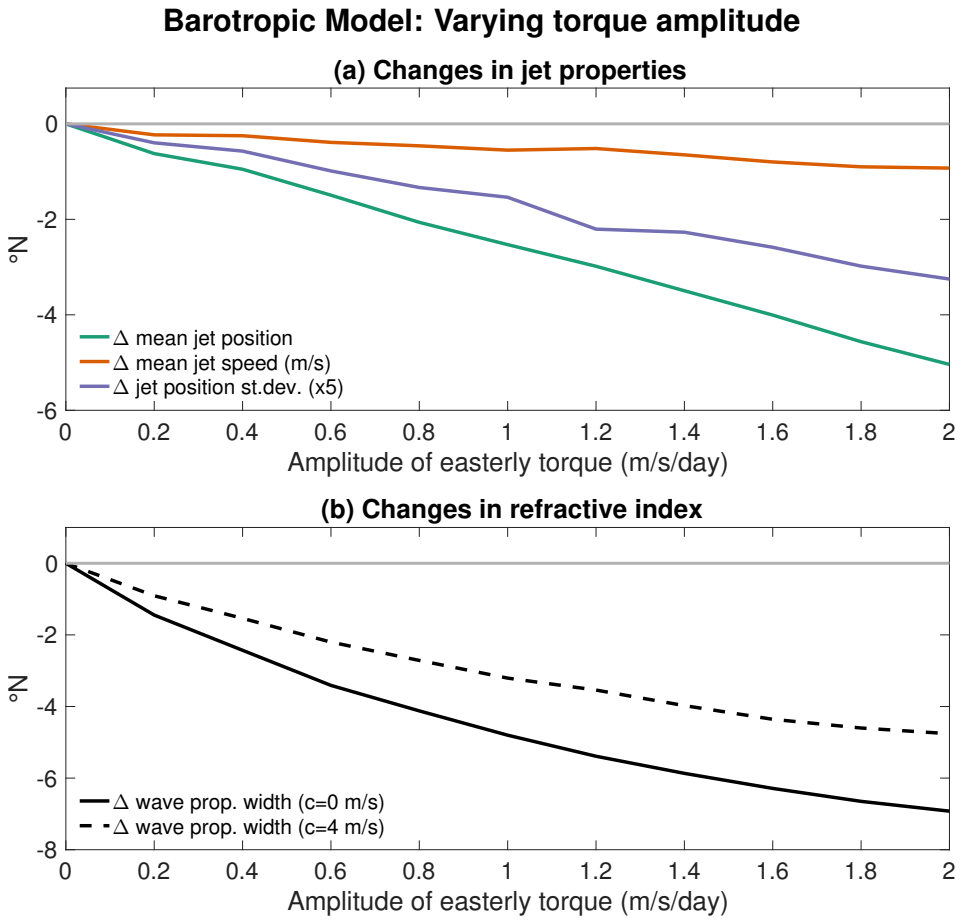

Fig. 2.10. (a) Changes in the mean jet position (green), jet speed (orange), and standard deviation of daily jet position (purple) between the torque and control simulations with the barotropic model under varying easterly torque amplitude. (b) Changes in the wavenumber $k = 4$ wave propagation width for phase speed $c = 0$ ms^{-1} (black solid) and $c = 4$ ms^{-1} (black dashed). For all experiments the torque is held constant at 55°N and stirring at 35°N.

decreases the wave propagation width which then decreases jet position variability, does a widening of the jet due to a westerly torque do the opposite? We run the same set of experiments as in *VaryAmp* but for a westerly torque on the poleward flank, with amplitudes 0.2 to 2.0 ms^{-1}day^{-1}.

The results are shown in Fig. 2.11, along with those for easterly torques, where we plot changes in jet position standard deviation and changes in wave propagation width for wavenumber $k = 4$ and phase speed $c = 4$ ms^{-1}. The negative amplitudes (blues) represent the easterly torque simulations already discussed, and positive amplitudes (reds) represent the westerly torque experiments. Fig. 2.11 demonstrates that as a westerly torque is applied and the amplitude is increased both the wave propagation width and the standard deviation of jet position increase, opposite to what happened with the easterly torque. The relation between changes in wave propagation width and jet position standard deviation is relatively linear for torques of 2.0 ms^{-1}day^{-1} down to approximately -1.0 ms^{-1}day^{-1}. From there, the increasing easterly torque amplitude results in a very large section of easterlies on the poleward flank of the jet. The wave propagation width continues to decrease, though not as strongly, as the easterlies become larger, and the jet positional variability also continues to decrease. Despite this limit on the wave propagation width decrease, the relationship between jet positional variance and wave propagation width appears consistent for both easterly and westerly torques, further strengthening the relationship between wave propagation width and jet variability.

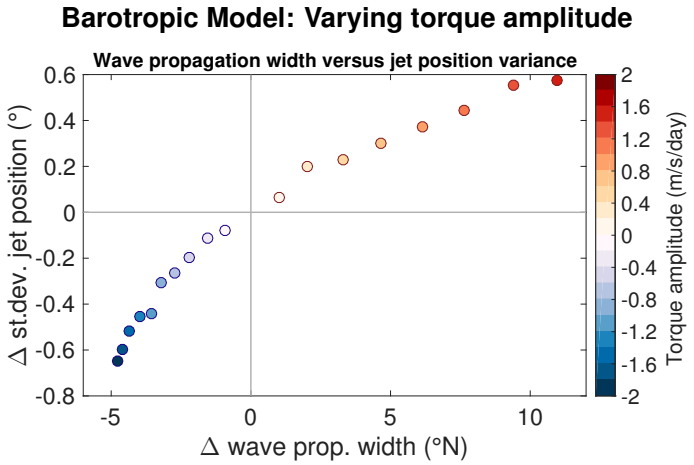

Fig. 2.11. The relationship between changes in the wavenumber $k = 4$ wave propagation width for phase speed $c = 4$ ms^{-1} and the standard deviation of jet position. The blue dots represent the same set of experiments as in Figure 2.10, with increasing easterly torque amplitude as the colors get darker. The red dots represent a similar set of experiments for increasing westerly torque amplitude. For all experiments the stirring is held fixed at 35°N and torque at 55°N.

2.4.3.3 *VaryStir*

Fully coupled models have a well known bias with regards to the mean jet position, placing it further equatorward than observations (e.g. Kidston and Gerber 2010; Barnes and Polvani 2013; Simpson and Polvani 2016). It has been argued that the response of the atmospheric circulation to various external forcings, including sea ice loss and Arctic amplification, could differ due to these biases (Barnes and Simpson 2017). In order to test the role of model bias, we run a set of experiments in the barotropic model with the easterly torque latitude and amplitude held fixed at 55^{o}N and -1.0 ms^{-1}day^{-1} respectively, while the stirring latitude is moved north from the equator to simulate model biases in the position of the climatological jet. For each new stirring latitude there is a control run (*NoTRQ*) and an experimental run (*TRQ10*), and the differences between the two (*TRQ10-NoTRQ*) are calculated. The resulting changes in mean jet position (green), speed (orange), positional standard deviation (purple) and wave propagation width (black solid and dashed) in response to the easterly torque are shown in Fig. 2.12. The location of the torque +/- one standard deviation is shown in grey shading. Note that all variables are plotted as a function of stirring latitude, and that the control jet position is generally consistently 2-3^o north of the stirring for stirring south of 40^o N. This was also noted in Barnes et al. (2010).

The mean jet position, represented in Fig. 2.12a by the green line, moves further equatorward as the stirring moves north towards the torque and the asymmetrical narrowing becomes more pronounced. The response of the mean jet speed (orange) is initially an increase for stirring from 10^{o}N to 35^{o}N, with seemingly no dependence on the stirring latitude within that range (i.e. the increase from control is generally by the same amount, even as the control itself is changing as it moves north), then plummets as the stirring get closer to the torque. Figure 2.12a also shows the jet position standard deviation (purple) decreasing fairly steadily for all stirring north of the equator, with a dependence on the stirring latitude. The decrease of jet position variability becomes smaller at stirring at 40^{o}N, showing a possible upward trend in the decrease of variability, though it still represents a decrease. We posit that this could be due to the jet being almost on top of the torque, at which point the likelihood of bimodality of the jet position increases, making our chosen metric for variability (standard deviation) no longer optimal (not shown). From Fig. 2.12b we see that

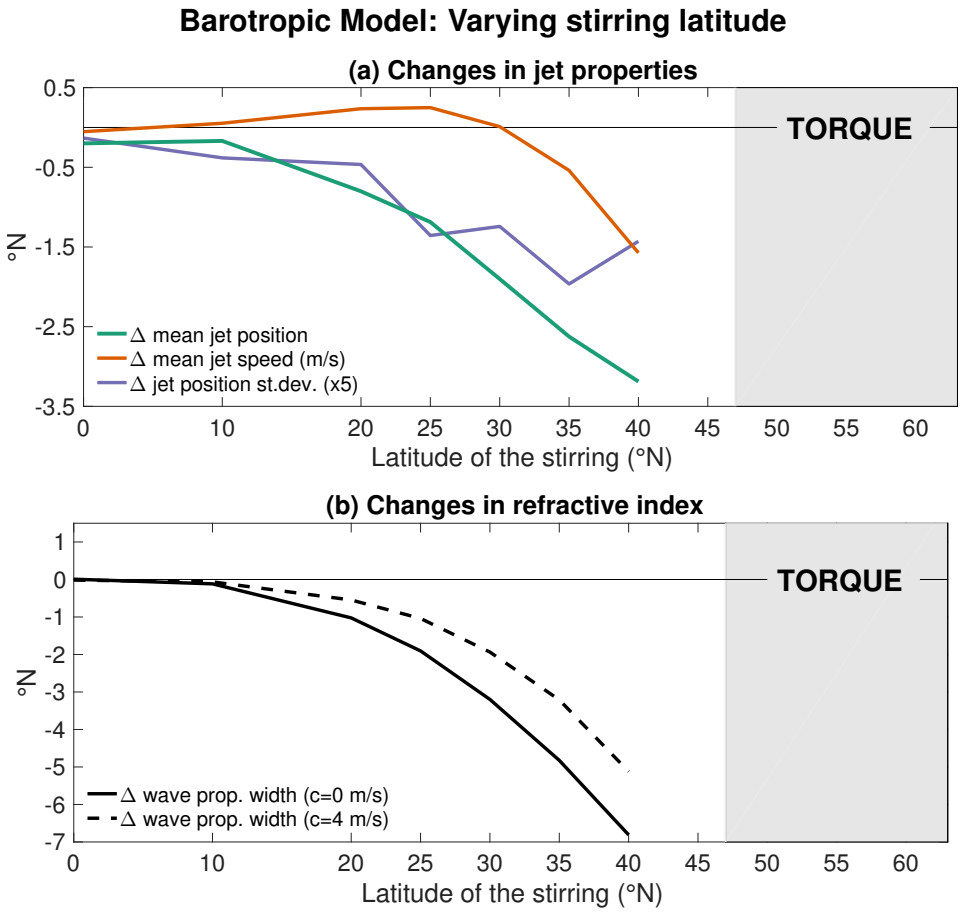

Fig. 2.12. (a) Changes in the mean jet position (green), jet speed (orange), and standard deviation of daily jet position (purple) between the torque and control simulations with the barotropic model under varying stirring latitudes. (b) Changes in the wavenumber $k = 4$ wave propagation width for phase speed $c = 0$ ms^{-1} (black solid) and $c = 4$ ms^{-1} (black dashed). For all experiments the torque is held fixed at 55^{o}N with an amplitude of -1.0 ms^{-1}day^{-1}. The grey shading represents the easterly torque from its center out to its half width.

the wave propagation width decreases very slightly for stirring at 10^{o}N, then steadily decreasing further as the stirring moves north (again, only shown for $k = 4$ and $c = 0, 4$ ms^{-1}). This decrease correlates highly with the apparent equatorward shift due to asymmetrical narrowing and the decrease in standard deviation, even for stirring as far south as 10^{o}N.

These results demonstrate how differently the mean jet responds to the torque on the poleward flank due only to changes in the jet's initial position, even in a simple barotropic model. While many of the responses are the same sign no matter the distance of the jet from the external forcing, their magnitudes are strongly dependent on jet proximity to the easterly torque. Interestingly, there is a range of latitudes across which jet speed increases, something which has previously been

noted in the CMIP5 models by Barnes and Simpson (2017). In analyzing the seasonality of the jet response to Arctic amplification, Barnes and Simpson (2017) found that the wind anomalies forced by the changing Arctic temperatures remained fairly stationary annually, with the jet moving in and out of the region of anomalous easterlies throughout the seasonal cycle, especially in the North Pacific. This suggests that our approach of keeping the torque fixed and varying the stirring is not only realistic, but also potentially important for understanding the effect of the climatological jet position on the jet's response to polar forcing.

2.5 DISCUSSION AND CONCLUSIONS

Here, we explore a possible mechanism for why jet positional variability, defined as the variance in location of the maximum zonal-mean zonal winds, decreases with sea ice loss and Arctic amplification. The key insights from this work can be summarized as follows:

- The response of the mean eddy-driven jet to sea ice loss and polar warming in both a fully coupled GCM and a dry dynamical core is an asymmetrical narrowing on the poleward flank of the zonal-mean eddy-driven jet (zonal-mean taken over the North Atlantic in the GCM and hemisphere-wide in the dry dynamical core). In both the CCSM4 and dry dynamical core experiments, the jet also exhibits decreased positional variability.
- Using a barotropic model, we find very similar responses in both the mean jet and the jet variability when an easterly torque is placed on the poleward flank of the jet.
- We propose and test a mechanism whereby the asymmetrical narrowing of the jet limits Rossby wave propagation out of the jet core, which in turn may be responsible for the decreased jet position variability.

We find decreased jet positional variability in all three models in response to polar forcing. Using a barotropic model we posit that decreased wave propagation width is a possible barotropic mechanism for this decreased variability, by acting to meridionally constrain the Rossby wave breaking and therefore the variability in zonal jet position. If the jet narrows in response to anomalous easterlies on the poleward flank, either due to sea ice loss, polar heating, or an easterly torque, Rossby waves will encounter a critical latitude closer to the jet core, which implies the deposition

of easterly momentum is closer to the jet core and therefore the jet is less likely to shift. This, in turn, decreases the variability in the jet position. Our results suggest that this change in Rossby wave breaking may be present across a model hierarchy, including a fully coupled GCM. While we believe this mechanism to be present in the real atmosphere, it is likely one of many dynamical mechanisms at play. For example, our idealized experiments do not take into account the role of stationary waves, which have been identified as important players in determining the atmospheric response to Arctic amplification and sea ice loss.

Both the dry dynamical core and the barotropic models showed a clear decrease in wind speeds within the climatological jet core (Figures 2.4, and 2.7 respectively). Results from Woollings et al. (2018) suggested a clear link between slower jets and **increased** jet positional variability. However, we again note that while their study focused on internal variability, we looked at changes in internal variability in response to an external forcing. The fact that we noted **decreased** jet positional variability suggests that the wave propagation response due to an external forcing and the subsequent narrowing seen in all three model setups has a greater influence on the jet variability response than the decrease in mean jet speed (which is also a result of the external forcing and associated feedbacks).

Upon examining Fig. 2.8a, specifically comparing the *NoTRQ* and *NoTRQ33* experiments in the barotropic model (stirring at 35^{o} N and 33^{o} N, respectively), we found that a jet shifted slightly equatorward, with no easterly torque, has decreased jet positional variability. This appears contrary to what was found by Barnes and Hartmann (2011), where jets equatorward of approximately 55^{o}N were shown to have similar jet positional variability (their Figure 8c). There are two reasons for this apparent discrepancy. First, Barnes and Hartmann (2011) did not show results for jets further south than 35^{o} N, and when we expand their previous methodology to stirring at these lower latitudes we find a similar decrease in jet “wobbling" as was found in our study. Second, Barnes and Hartmann (2011) used Empirical Orthogonal Functions in order to separate the variability into orthogonal modes of variability, with the leading mode generally being referred to as a “shift" unless the jet is placed too close to the pole. As such, any shifting of the jet position based upon this leading mode of variability may not capture all of the jet’s meridional movement, whereas our

metric is exactly that: the change in the mean jet position as the stirring latitude is changed.

We also note a decrease in both the climatological jet core speeds and the jet speed variability in both the dry dynamical core and the barotropic models. We posit that as the jet narrows, more waves break within the jet core itself, depositing easterly momentum there, which leads to the decrease in mean speed. As the zonal wind speed decreases, the variance in speed also goes down (Klink 1999; May and Bourassa 2011). Thus, the decrease in jet speed variability may have more to do with the mean speed decrease, rather than our barotropic wave breaking argument, though this also warrants further study.

The results of this study imply that when considering the impact of sea ice loss and/or Arctic amplification on the jet stream, it is important to consider changes in the width of the jet stream and associated Rossby wave propagation, and not just the jet position or speed. An apparent shift of jet position could either be a displacement of the entire jet profile, impacting both flanks of the jet, or it could be due to an asymmetrical narrowing of the jet, as is the case here. The resulting changes in jet stream variability are sensitive to this distinction.

Further, the precise nature and amplitude of the response of the zonal wind to sea ice loss and Arctic amplification likely depends on the position of the climatological jet relative to where the forcing is located. Ring and Plumb (2007, 2008) found in an idealized dry dynamical core GCM that the exact nature of the atmospheric response to an imposed torque was dependent on the location of the torque, particularly in regards to how well the response projected onto the annular modes. Barnes and Thompson (2014) also imposed torques at varying latitudes in both an idealized GCM and a barotropic model, with similar findings. The idea that the structure of the atmospheric response, as well as the magnitude of the response, are dependent on the initial position of the jet with respect to the position of the external forcing is crucial when discussing the differences in the responses from different climate models, as many have the jet placed further equatorward than observed (Kidston and Gerber 2010; Bracegirdle et al. 2013).

Many studies define jet positional variability as a measurement of jet amplitude, or “waviness", over space, and have argued that this variability increases with sea ice loss and Arctic amplification (e.g. Francis and Vavrus 2012; Liu et al. 2012; Peings and Magnusdottir 2014; Francis and Vavrus

2015). Here, we define jet positional variability as changes in the location of the zonal-mean zonal wind maximum over time, and, when we do so, we find the opposite response: a decrease in jet positional variability. Though the decrease in positional variability is small, it is consistent across a model hierarchy, leading us to believe that this response is robust. This suggests that further work examining the difference between spatial and temporal jet variability in response to external forcing is important for broader understanding of the mechanisms at play.

The authors would like to thank Lantao Sun for providing the CCSM4 data, Ding Ma for his insightful discussions, and three anonymous reviewers for their constructive evaluations. BR and EAB are supported by the Climate and Large-scale Dynamics Program of the National Science Foundation under Grant AGS-1545675. PH is supported by NASA grant 80NSSC17K0266.

3 A role for barotropic eddy-mean flow feedbacks in the zonal wind response to sea ice loss and Arctic Amplification[2]

Previous studies have suggested that, in the zonal mean, the climatological Northern Hemisphere winter-time eddy-driven jet streams will weaken and shift equatorward in response to Arctic amplification and sea ice loss. However, multiple studies have also pointed out that this response has strong regional differences across the two ocean basins, with the North Atlantic jet stream generally weakening across models and the North Pacific jet stream showing signs of strengthening. Based on the zonal wind response with a fully coupled model, this work sets up two case studies using a barotropic model to test a dynamical mechanism which can explain the differences in zonal wind response in the North Pacific versus the North Atlantic. Results indicate that the differences between the two basins are due, at least in part, to differences in the proximity of the jet streams to the sea ice loss, and that in both cases the eddies act to increase the jet speed via changes in wave breaking location and frequency. Thus, while baroclinic arguments may account for an initial reduction in the midlatitude winds through thermal wind balance, eddy-mean flow feedbacks are likely instrumental in determining the final total response and actually act to strengthen the eddy-driven jet stream.

3.1 INTRODUCTION

A great deal of contemporary research looking at the midlatitude circulation has focused on how the eddy-driven jet stream will respond to external forcing associated with climate change (e.g. Peings et al. 2017; Iqbal et al. 2018; Peings et al. 2018; Ronalds et al. 2018; Screen et al. 2018a,b; Whittleston et al. 2018). One of the prominent signals of climate change is the amplified warming in the Arctic, approximately twice the globally averaged warming rate (e.g. Holland and Bitz 2003; Serreze and Francis 2006; Screen and Simmonds 2010). This phenomenon, commonly

[2]This chapter contains material that has been published in the *Journal of Climate* as: Ronalds, B. and E.A. Barnes, 2019: A role for barotropic eddy-mean flow feedbacks in the zonal wind response to sea ice loss and Arctic Amplification. *J. Climate*, **32**, 7469-7481, https://doi.org/10.1175/JCLI-D-19-0157.1.

referred to as Arctic amplification, has implications for Northern Hemisphere extreme weather events, in addition to ecological and economic repercussions (e.g. Meier et al. 2014; Cohen et al. 2018; Kretschmer et al. 2018; Zhang et al. 2018). It has been proposed that Arctic amplification will both directly and remotely affect the eddy-driven jet stream (e.g. Peings and Magnusdottir 2014; Hoskins and Woollings 2015; Petrie et al. 2015; Peings 2018; Screen et al. 2018b; Ronalds et al. 2018), a large-scale circulation phenomenon which steers the storm tracks (e.g. Hoskins and Valdes 1990). However, studies attempting to diagnose these impacts have widely varying results across models (as shown in Screen et al. 2018b), and also strong regional and seasonal differences (e.g. McGraw and Barnes 2016; Barnes and Simpson 2017; Ronalds et al. 2018), with recent studies finding that the largest circulation response occurs in late winter (e.g. Zappa et al. 2018). Furthermore, studies using reanalysis data struggle with causally linking the observed changes in the Arctic to any trends in the midlatitude circulation response because of the inherent noisiness of the climate system and the brevity of the climate record (e.g. Manney and Hegglin 2018; Gu et al. 2018). Due to these complications, and the large internal variability of the system, there remains a lack of dynamical understanding of the exact mechanisms linking Arctic change directly to a midlatitude response (e.g. Hoskins and Woollings 2015; Shepherd 2016; Cohen et al. 2018).

The majority of studies looking at the Arctic's ability to impact the midlatitude circulation use models of varying complexity, and diagnose changes in the large-scale zonal wind field in response to imposed sea ice loss or low-level warming (e.g. Magnusdottir et al. 2004; Deser et al. 2004, 2010; Screen and Simmonds 2013; Cohen et al. 2014; Peings and Magnusdottir 2014; Deser et al. 2015; Shepherd 2016; Screen et al. 2018b, among others). In the zonal mean, most models show the boreal winter Northern Hemisphere eddy-driven jet stream weakening in response to sea ice loss and Arctic amplification, and some show a slight equatorward shift as well (e.g. Screen et al. 2018b; Peings 2018; Zappa et al. 2018). While this appears to be true of the North Atlantic jet (e.g. Deser et al. 2010; Barnes and Simpson 2017; Ronalds et al. 2018; Sun et al. 2018; Zappa et al. 2018), a recent study found that many climate models project an increase in jet speed in the North Pacific in response to sea ice loss and Arctic amplification, with little to no shift in jet latitude (Barnes and Simpson 2017). Multiple studies have specifically investigated dynamical

mechanisms which may explain why and how the circulation responds to external forcing (e.g. Vallis et al. 2004; Strong and Magnusdottir 2010; Barnes et al. 2010; Ring and Plumb 2007; Kim et al. 2014; Kretschmer et al. 2016; Gu et al. 2018; Ronalds et al. 2018). These proposed dynamical mechanisms are often based in Rossby wave dynamics and eddy-mean flow feedbacks, with changes in wave propagation, dissipation, breaking and generation (i.e. baroclinic zones) leading to changes in the large-scale circulation (e.g. Strong and Magnusdottir 2010; Barnes et al. 2010; Schubert et al. 2011; Coumou et al. 2014; Kim et al. 2014; Wu and Smith 2016; Ronalds et al. 2018). For example, Kim et al. (2014) found that the Arctic warming signal in specific regions causes an enhancement of vertically propagating waves, thus leading to a weakened stratospheric polar vortex, which then feeds-back onto the tropospheric circulation. Other studies have examined the impact of horizontally propagating Rossby waves, where changes in jet latitude and horizontal wind shear can cause Rossby waves to reflect rather than break (e.g. Strong and Magnusdottir 2010; Barnes et al. 2010), or vice versa.

Understanding and applying these mechanisms directly to the observations, reanalyses or model simulations remains difficult, as it is hard to separate out cause and effect from the background noise (e.g. Cohen et al. 2014; Hoskins and Woollings 2015; Samarasinghe et al. 2018). A common approach to isolating and studying specific mechanisms is using idealized models (e.g. Vallis et al. 2004; Ring and Plumb 2007; Barnes et al. 2010; Ronalds et al. 2018). This is especially useful when studying Rossby wave dynamics, which can be well represented in a simple barotropic model set-up, as demonstrated by Vallis et al. (2004). It is well appreciated that Rossby wave dynamics and their resulting feedbacks with the mean flow are foundational to large-scale dynamics and will be at play in the fully coupled climate system (e.g. Strong and Magnusdottir 2010; Vallis 2017). Thus, this work, while inspired by results from a sea ice loss experiment in a fully coupled model, is focused on studying an essential, barotropic mechanism: the response of the zonal-mean flow driven by changes in eddy propagation and breaking in response to changes in the meridional wind shear. The proposed mechanism is supported by the work of Strong and Magnusdottir (2010), where they showed that changes in Rossby wave breaking bridge the gap between the initial, local, baroclinic zonal wind response to a sea ice anomaly and the longer timescale, hemisphere-wide,

equivalent barotropic zonal wind response. In their study, the impact of Rossby wave breaking changes on the mean zonal wind field was estimated to account for approximately 80% of the zonally averaged zonal wind response in a fully coupled model, supporting the theory that these eddy-mean flow feedbacks are critical in understanding the real-world, midlatitude, large-scale circulation response to climate forcing.

We propose that sea ice loss and Arctic amplification directly affects the local mean flow through weakening of the surface temperature gradient, resulting in localized anomalous, low-level easterlies at high latitudes (Strong and Magnusdottir 2010). We are interested in how the eddies then respond to the initial zonal wind response, driving future changes in the large-scale circulation. Here, we explicitly represent the direct effect of the sea ice loss on the zonal flow and study the eddy response using a non-divergent barotropic model. Through this approach, we can explain both the climatological zonal wind response to Arctic amplification in a fully coupled model, and the regional differences across the two Northern Hemisphere ocean basins. Since the proposed mechanism is barotropic in nature, its effects would be present in all models and observations, though this work does not specifically address its relative importance or magnitude in the fully coupled system.

3.2 MODEL DATA

3.2.1 CCSM4

We are interested in how the zonal winds respond to sea ice loss. In order to motivate our idealized model experiments, we analyze sea ice loss simulations with a fully coupled global climate model, the Community Climate System Model version 4 (CCSM4; Deser et al. 2015). The model is run at a horizontal resolution of 0.90^{o} latitude and 1.25^{o} longitude, with 26 vertical levels, and a full oceanic component. Full details of the experiment can be found in Deser et al. (2015), and a brief overview is also provided in Ronalds et al. (2018). We use 260 years of monthly data for both a control simulation (*CONTROL*), with sea ice concentration based on an ensemble mean of six historical CCSM4 runs over the period 1980-1999, and an experiment simulation (*LOWICE*), with sea ice concentration based on an ensemble mean of six RCP8.5 CCSM4 runs over the period

2080-2099. The model uses a ghost radiative flux felt only by the ice model component to melt the sea ice to the respective ensemble mean concentrations. The variable analyzed is monthly 700 hPa zonal winds.

3.2.2 Barotropic Model

As in Ronalds et al. (2018), we utilize a non-divergent barotropic model in order to begin understanding the mechanisms at play in the remote wind response to sea ice loss. We use an initial model set-up identical to that of Vallis et al. (2004), where the non-divergent vorticity equation is integrated on the sphere:

$$\frac{\partial \zeta}{\partial t} + J(\psi, \zeta + f) = S - r\zeta + \kappa\nabla^4\zeta \tag{3.1}$$

The left hand side of (3.1) represents the Lagrangian change in absolute vorticity (relative vorticity, ζ, plus planetary vorticity, f). The right hand side consists of a parameterized representation of the baroclinic eddies that stir the barotropic flow, S. The amplitude of S is randomly chosen in a given range, here $[-12, 12] \times 10^{-11}$. There is also a damping parameter, r, and a diffusion term, κ. Values for r and κ are identical to those used in Barnes et al. (2010).

Baroclinic instability in the model is represented by the imposed stochastic stirring, S, generating waves within the total wavenumber range of $n = 8 - 12$. Therefore larger waves are not specifically forced by the stirring (see Vallis et al. 2004, for more details). In order to simulate a meridionally confined jet we then impose a Gaussian spatial mask, damping the parameterized stirring away from a chosen latitude, ϕ_s, with a specified width, σ_s (e.g. Vallis et al. 2004). For all experiments here we set $\sigma_s = 12^o$ and vary ϕ_s. We use a resolution of T42 and a time step of 1800 seconds. Each simulation is run for 32,100 days, with the first 100 days discarded for spun up.

As the Arctic warms, the sea ice melts and the surface temperature gradient is weakened in the region of sea ice loss. The winds must respond to the decreased temperature gradient, and we expect them to initially locally weaken in keeping with thermal wind balance arguments. We interpret this initial weakening of the zonal winds as the direct effect of sea ice loss and the associated weakening of the temperature gradient (e.g. Strong and Magnusdottir 2010). We explicitly

represent this initial impact as a meridionally constrained easterly torque acting on the zonal wind field (i.e. Ronalds et al. 2018). From there, we analyze the subsequent eddy response to the locally weakened winds. The easterly torque is a Gaussian in latitude with an amplitude of -2.0 $ms^{-1}day^{-1}$ and a standard deviation of σ_f= 8° latitude (see also Ronalds et al. 2018). The Gaussian forcing is centered at latitude ϕ_f , which we adjust depending on the experimental setup. We run the model three times for each setup. The first run has no torque, and only the stirring, which gives us a control jet, and is referred to as *NoTRQ*. The second run has both stirring and torque turned on in the model, and gives us a jet resulting from the imposed torque plus any feedbacks associated with eddies reacting to the torque. We refer to this run as *TOTAL*. Finally, we run the model with the stirring turned off, and only the torque acting on the wind field at every time step. This results in a zonally symmetric wind field directly produced by the torque. We then add this wind field to the *NoTRQ* jet, giving us a resulting wind field that is the direct response of the zonal flow to the imposed torque, in the absence of eddy feedbacks. We call this run *NoEDDIES*, and it allows us to separate between the direct response of the zonal wind and the evolution of the wind field when eddy-mean flow feedbacks are present (*TOTAL*).

3.3 ROSSBY WAVE ANALYSIS

In the barotropic model, changes in the mean wind field driven by the imposed forcing are a combination of (1) a direct response to the forcing and (2) eddy-mean flow feedbacks resulting from changes in Rossby wave propagation and breaking/dissipation. We separate out the direct effect using the *NoEDDIES* simulation, and the difference between *NoEDDIES* and *TOTAL* gives us the impact of the eddies. The eddy contribution to the response is primarily controlled by changes in the convergence of eddy momentum fluxes, as well as damping and diffusion effects responding to the mean flow changes caused by the eddies. In our setup, any changes in the convergence of eddy momentum flux implies changes in wave breaking locations and/or frequencies of the eddies. We diagnose changes in wave breaking in the barotropic model using refractive indices and an

algorithm to count wave breaking events, the details of which are given below.

3.3.1 Critical and reflective profiles

Rossby wave breaking theory states that waves propagating out of the jet core will be forced to break as their phase speed approaches the background zonal mean zonal wind (e.g. Hoskins and Karoly 1981; Strong and Magnusdottir 2010). The latitude at which this occurs is referred to as the critical latitude, and can be found using the climatological zonal mean zonal wind profile. This profile sets the critical latitudes for waves of all zonal wavenumbers as a function of phase speed. While in reality Rossby waves can break anywhere between the source and the critical latitudes, they favor the critical latitudes defined by the climatological jet profiles, as demonstrated in Barnes and Hartmann (2012). Depending on the gradient of absolute vorticity through which the wave is traveling (a function of both the background zonal wind and latitude), a wave may be forced to turn before it can break, generally on the poleward flank of the jet. In order to calculate these regions of turning, called the reflective latitudes, we use the refractive index (K^*), e.g. Hoskins and Karoly (1981):

$$K^* = cos(\phi)\sqrt{\frac{\hat{\beta}}{\bar{u}-c}}, \quad \text{and} \quad K^{*2} = k^2 + l^2, \tag{3.2}$$

where k and l are the zonal and meridional wave numbers, respectively. $\hat{\beta}$ is the meridional gradient of absolute vorticity, $\bar{u}$ is the zonal-mean zonal wind, and c is the phase speed (Hoskins and Karoly 1981; Barnes et al. 2010). The additional factor of $cos(\phi)$ accounts for the fact that the specific wavelength associated with a zonal wave number k decreases with latitude (Barnes and Hartmann 2012). The waves will reflect when their zonal wave number is equal to K^* (i.e. $l = 0$). We can therefore rearrange (3.2) to give the phase speed as a function of zonal wave number, k, for when a wave reaches its turning latitude.

$$c = \bar{u} - cos(\phi)\frac{\hat{\beta}}{k^2} \tag{3.3}$$

Equation (3.3) allows us to map out where waves of different sizes will be forced to turn (reflective latitude) and compare to where they prefer to break (critical latitude). The $\hat{\beta}$ term in (3.3) represents a dependence of the reflective profiles on both the latitude and meridional wind shear of the climatological jet profile. By analyzing the changes in reflective and critical profiles in *NoEDDIES* versus *NoTRQ*, we can evaluate exactly how the imposed torque directly affects where waves are breaking or turning. Any changes in *TOTAL* relative to *NoEDDIES* represent further adjustments by the eddies.

Since K^* depends on phase speed and the reflective profiles depend on wave number, we must determine the most important combinations of the two. To do so, we calculate the power spectra of the eddy momentum fluxes in both the *NoTRQ* and *TOTAL* runs as a function of both phase speed and zonal wavenumber. The space-time spectral analysis is conducted using a chunk length of 256 days, with a Hamming window and an overlap of half the chunk size. The structure of the resulting average power spectra allows us to determine which specific waves are crucial for the eddy-mean flow interactions. Further, an analysis of the difference in power between *TOTAL* and *NoTRQ* shows how the induced torque and resulting eddy feedbacks actually change which waves contribute the most to the overall eddy momentum fluxes.

3.3.2 Wave breaking counts

While the use of the refractive index has been shown to be highly accurate in predicting *where* wave breaking will occur in a climatological sense (Barnes and Hartmann 2012), it does not provide the frequency of wave breaking. There are many existing algorithms which attempt to identify and categorize wave breaking events. For the purposes of this work, we utilize the algorithm of Barnes and Hartmann (2012) (see their section 2.3), using the daily output wind field data from each barotropic model experiment (*NoTRQ* and *TOTAL* from two experimental set-ups). To define a wave breaking event, the algorithm follows a contour of absolute vorticity and identifies a location where a meridian intersects the contour at least three times, called the overturning points (Barnes and Hartmann 2012, see their Fig. 2). These daily overturning point locations are then grouped into events of varying size, location and duration. We define the location of mixing as the

centroid of the overturning points. Note that this algorithm, similarly to others, identifies all wave breaking events as those that are in the process of overturning, and assumes that each event irreversibly mixes (fully breaks), which may not always be the case. This caveat is often considered to be negligible (e.g. Barnes and Hartmann 2012; Garfinkel and Waugh 2014), though further work quantifying this assumption is needed.

3.4 RESULTS

Our interest here is of the role of the eddies in determining the zonal wind response to changes in surface temperature gradients caused by Arctic amplification and sea ice loss. In order to motivate our idealized experiments we begin our analysis with the sea ice loss experiment conducted using the CCSM4 (Deser et al. 2015), comprised of a sea ice loss run (*LOWICE*) and a control run (*CONTROL*). Specifically, we examine the change in the late boreal winter Northern Hemisphere ocean basin eddy-driven jet streams, as this is the season with the largest expected large-scale atmospheric circulation response (Zappa et al. 2018). Using the January-February-March (JFM) 700 hPa zonal wind field we define two regions of interest, where the largest changes in zonal wind occur (changes considered significant at 95% confidence level using a Student's t-test). The two regions are defined as the North Pacific downstream jet region (180-225^{o}E), and the North Atlantic downstream jet region (310-355^{o}E). The sector-averaged 700 hPa zonal winds across these two regions are plotted in Fig. 3.1, with *CONTROL* in black, and *LOWICE* in red.

The dominant change in the zonal mean zonal flow in both the North Pacific (Fig. 3.1a) and the North Atlantic (Fig. 3.1b) is the easterly anomalies on the poleward flank of the jet. Both basins exhibit a region of enhanced easterlies and weakened westerlies poleward of the jet core in *LOWICE* (red) versus *CONTROL* (black). For both cases, the weakening of the winds is limited to north of 45^{o}N. In the North Atlantic, this means the decreased zonal mean zonal wind speeds extend into the jet core, both weakening the jet and asymmetrically narrowing it. This narrowing also causes a very small equatorward shift of the jet latitude of 0.7^o. There are no changes to the winds south of 45^{o}N in the North Atlantic case. Conversely, the North Pacific basin exhibits strengthened wind speeds south of 45^{o}N, with the anomalous easterlies limited to the poleward flank of the jet. The

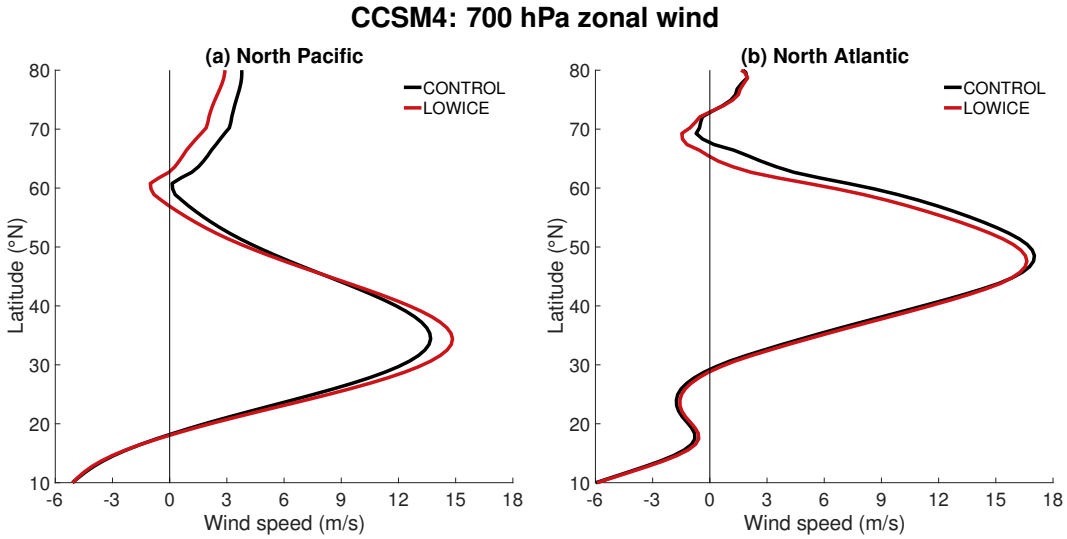

Fig. 3.1. Zonal mean zonal wind profiles at 700 hPa for (a) the North Pacific, and (b) the North Atlantic downstream jet regions. The control experiment, *CONTROL*, is in black and the sea ice loss experiment, *LOWICE*, is in red.

changes in both basins' zonal mean jet speeds and locations are considered significant at a 95% confidence level, according to a Student's t-test.

The North Atlantic and North Pacific basins in the CCSM4 sea ice loss experiment have opposing responses within the jet core to sea ice loss. One possible explanation for this is that differences in jet proximity to the region of sea ice loss lead to differences in eddy-mean flow feedbacks. In the North Pacific the jet is further south than in the North Atlantic (e.g. Hoskins and Valdes 1990), and the sea ice edge is, on average, further north (e.g. Bitz et al. 2005), implying that the North Pacific jet is much further from where the sea ice loss is occurring than the North Atlantic jet. We use the barotropic model to test the theory that these differences in jet latitude and distance from the region of sea ice loss drive differing eddy-mean flow feedback responses.

3.4.1 Barotropic model

The CCSM4 results show two regions with very different changes to the overall jet structure resulting from sea ice loss and the associated Arctic warming. From these two cases, we build an idealized model setup to explore the role of eddies in these different regional responses. The

experiments use a meridionally confined stirring region to simulate the midlatitude baroclinic zone and thus drive a jet stream, and an easterly torque on the poleward flank of the jet to represent the initial circulation response to sea ice loss (see Section 3.2 for more details). The choice of where to place the stirring and the torque are inspired by the two CCSM4 cases: the North Pacific experiment (NPAC) has the stirring placed at $\phi_s = 30^o$N and the torque at $\phi_f = 70^o$N, while the North Atlantic experiment (NATL) has $\phi_s = 45^o$N and $\phi_f = 60^o$N. The results shown here are those with the largest magnitude and those which clearly demonstrate the mechanisms involved, although the results are considered robust across ϕ_s, $\phi_f \pm 5^o$, and the conclusions are consistent across all midlatitude stirring latitudes with $\phi_f > \phi_s$ (not shown). The zonal mean zonal wind profiles for the barotropic model are plotted in Fig. 3.2 for (a) NPAC and (b) NATL. For both, the *NoTRQ* run is in black, *NoEDDIES* in orange, and *TOTAL* in red. The difference between *TOTAL* and *NoEDDIES* can be interpreted as the eddy contribution to the mean flow response and is plotted in Fig. 3.2c for NPAC and Fig. 3.2d for NATL. The horizontal lines in Fig. 3.2c and d represent the torque latitude (orange) and the stirring latitude (red).

The *NoEDDIES* (orange) response indicates the direct response of the zonal mean zonal winds to the imposed easterly torque. The torque forces decreased wind speeds in the vicinity of the torque center, with no effect further south (Fig. 3.2a and b, orange versus black). The *NoEDDIES* run in both cases exhibits a region of significantly stronger easterlies to the north of the jet compared to *NoTRQ*, as intended. In the NPAC case (Fig. 3.2a), the torque only directly affects the poleward flank, increasing the pre-existing, weak easterlies. In the NATL case (Fig. 3.2b), the direct effect of the imposed forcing extends into the jet core, leading to strong easterlies to the north, and decreased wind speeds along the poleward flank and in the jet core.

The *TOTAL* (red) response represents the direct effect plus the eddy-feedback response to the imposed torque. The *TOTAL* zonal mean zonal wind maximum increases in the NPAC case (Fig. 3.2a), and decreases in the NATL (Fig. 3.2b), compared to the *NoTRQ* run (black). This closely resembles the behavior seen in CCSM4. The NATL *TOTAL* wind profile shows increased wind speeds on the equatorward flank, suggesting a larger equatorward shift of the wind profile

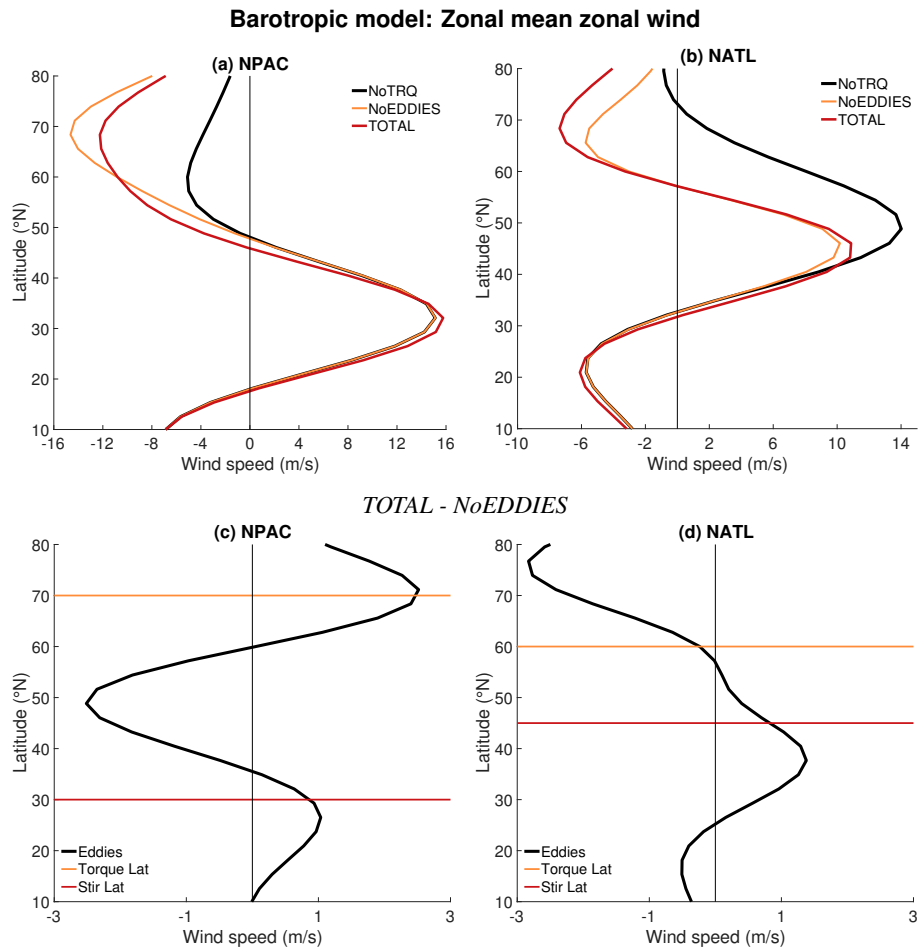

Fig. 3.2. Top row shows zonal mean zonal wind profiles from the (a) NPAC and (b) NATL setups. *NoTRQ* is in black, *NoEDDIES* in orange, and *TOTAL* is in red. Bottom row shows the difference in the zonal mean zonal wind field between *TOTAL* and *NoEDDIES* in black solid for (c) NPAC and (d) NATL. The horizontal lines represent the torque and stirring latitudes (orange and red, respectively).

than seen in the CCSM4 North Atlantic results. Additionally, in the region of equatorward easterlies in NATL there is a decrease in wind speeds, opposite to what we saw in the North Atlantic mean from CCSM4 (Fig. 3.1b). However, the general behavior of both barotropic model simulations is very similar to the CCSM4 results.

Comparing *TOTAL* (red) to *NoEDDIES* (orange) instead of *NoTRQ* (black) in Fig. 3.2 gives us the eddy response to the imposed torque. If there was no eddy response the two wind profiles would look identical, however, this is not the case. In order to more clearly see the full role of the eddies we plot the difference between *TOTAL* and *NoEDDIES*, shown in black solid in Fig. 3.2c and d. In both setups the eddies *increase wind speeds in the jet core*, both centered-on and south

of the stirring location, and decrease the winds to the north. In the NPAC case the decreased wind speeds occur relatively close to the jet core, thus narrowing the jet on the poleward side. The high latitude wind decrease in the NATL setup occurs well north of the jet, and we do not see any poleward flank narrowing of the jet caused by the eddies. However, we do see a small widening of the jet on the equatorward flank due to the eddies, with strengthened wind speeds extending south to around 25 ^{o}N. Another difference between the NPAC and NATL eddy response is seen in the region of increased wind speeds in NPAC north of 65^{o}N, which is not seen in the NATL case. The strengthening of the northerly winds in NPAC represents less intense easterlies in that region, rather than positive wind speeds, and an explanation for this will be discussed later in the text.

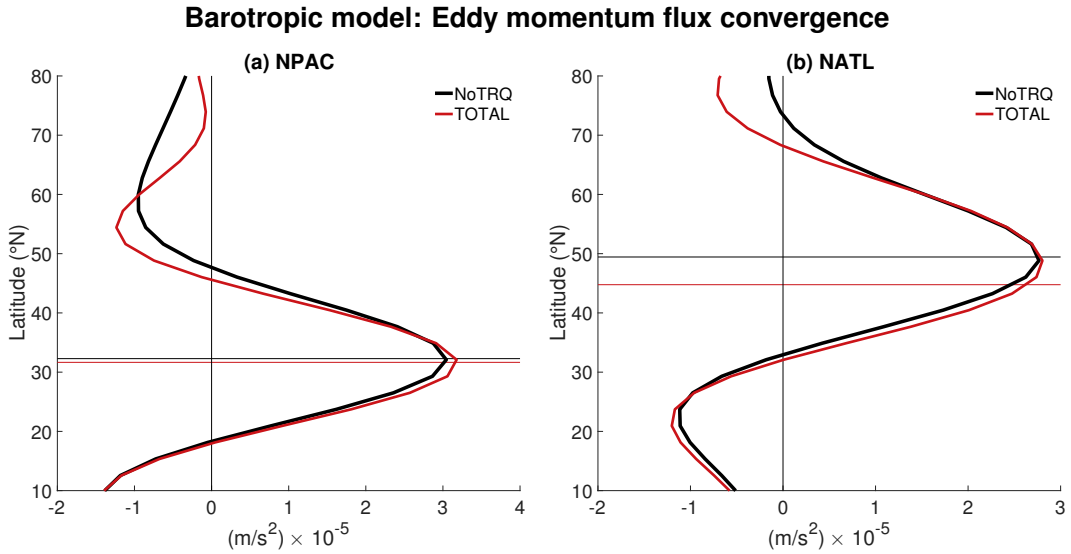

Fig. 3.3. The eddy momentum flux convergence (a) NPAC and (b) NATL, with *NoTRQ* in black and *TOTAL* in red. The thin, horizontal lines represent the respective jet latitudes.

The eddy-induced changes in the climatological zonal mean zonal wind field are nearly completely explained by the eddy momentum flux convergence (Fig. 3.3). By definition, the simulations without stirring and only the torque acting on the zonal wind have no eddy activity, and thus, comparing *TOTAL* (red) to *NoTRQ* (black) gives us the net eddy momentum flux response to the imposed torque. For both NPAC (Fig. 3.3a) and NATL (Fig. 3.3b) there is increased eddy

momentum flux convergence at the jet core, and decreased convergence to the north. The latter indicates decreased wind speeds on the poleward side of the jet, while the former indicates increased jet speeds. This is consistent with our analysis from Fig. 3.2. The small differences between the changes to the *TOTAL* wind field versus *NoEDDIES* in Fig. 3.2 and the changes to the eddy momentum flux convergence in Fig. 3.3 are due to the damping and diffusion of the portion of the mean flow altered by the eddies via the momentum fluxes.

Figure 3.3 shows that the eddies respond to the imposed torque through changes in momentum fluxes. By analyzing the power spectrum of the eddy momentum fluxes as a function of both phase speed and zonal wavenumber we can determine which waves are most important for the transport of momentum. The power spectra at the mean jet latitude is calculated for the *NoTRQ* and *TOTAL* runs from both experiments and plotted in Fig. 3.4. The conclusions drawn remain unchanged if we calculate the power spectra at the stirring latitudes, or calculate the average power across the stirring regions.

In the NPAC case the power spectra in *NoTRQ* (Fig. 3.4a) and *TOTAL* (Fig. 3.4b) both show peaks in power for phase speeds around -9 ms^{-1} to 5 ms^{-1}, and wavenumbers $k = 5-9$. The spectra is similar between *TOTAL* and *NoTRQ*, indicating that in the NPAC case the imposed torque does not change which waves are most important for fluxing momentum. In the NATL case (Fig. 3.4c, d), the power is generally shifted to smaller wavenumbers than in NPAC. This is due to the higher latitude stirring in NATL, which has been previously shown to shift the power to larger wavelengths (e.g. Barnes and Hartmann 2011). For the NATL *NoTRQ* run (Fig. 3.4c) the waves primarily responsible for the flux of momentum are generally within the zonal wavenumber range of $k = 4-7$, peaking at $k = 6$, and phase speeds of -6 ms^{-1} to about 9 ms^{-1}. In the *TOTAL* run (Fig. 3.4d), however, the peak power shifts significantly, and is concentrated at negative phase speeds and slightly smaller wavenumbers. The biggest changes occur around wavenumbers $k = 5-6$, where there is almost no power remaining for waves with positive phase speeds in *TOTAL* and there is a significant increase in power at negative phase speeds. That is, the imposed torque changes which waves are most important for the transportation of easterly momentum out of the jet core. This response is similar to that seen in Strong and Magnusdottir (2010), where they observe a shift in power to

smaller phase speeds and zonal wavenumber in response to imposed sea ice loss in a fully coupled climate model.

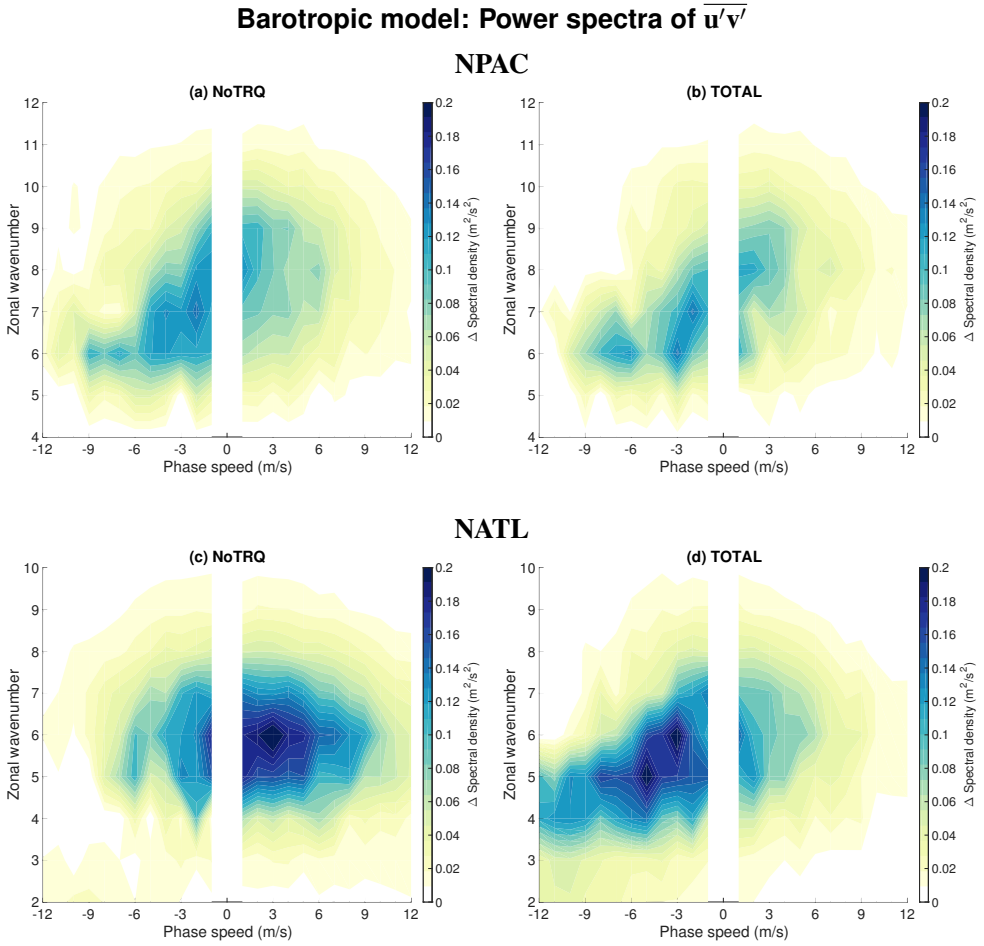

Fig. 3.4. The power spectra density of the eddy momentum fluxes for the NPAC (a) *NoTRQ* and (b) *TOTAL* experiments, and the NATL (c) *NoTRQ* and (d) *TOTAL* experiments. The spectra are evaluated at the respective jet latitudes, and are a function of both phase speed and wavenumber. The wavenumber range for NPAC (a, b) is $k = 4-12$, and for NATL (c, d) it is $k = 2-10$.

Changes in eddy momentum flux convergence in response to an imposed torque, as shown in Fig. 3.3, imply changes in the eddy activity, specifically changes in the propagation and breaking of waves. Similar to previous work, (e.g. Barnes and Hartmann 2012; Lorenz 2014a; Ronalds et al. 2018), we use the critical and reflective profiles associated with each run to analyze changes in wave propagation and the locations of wave breaking. Figure 3.4 shows which waves have the most power in fluxing momentum, allowing us to objectively pick the reflective profiles of interest

in both experiments, and focusing our analysis on the crucial phase speeds. We further supplement the information provided by the refractive index profiles with counts of *NoTRQ* and *TOTAL* wave breaking events for both NPAC and NATL in the sections below.

3.4.1.1 Eddy activity: North Pacific

In the NPAC case we found the reflective profile associated with $k = 6$ to be the clearest representation of the eddy response to the imposed torque. The NPAC critical (solid) and reflective (dotted) profiles for zonal wavenumber $k = 6$ are shown in Fig. 3.5a, with *NoTRQ* in black, *TOTAL* in red and *NoEDDIES* in orange. The grey shading represents the one standard deviation extent of the Gaussian-shaped stirring mask. Remember that while there are no eddies responding to the altered zonal mean zonal wind profile in the *NoEDDIES* run, we can still use its critical and reflective profiles to tell us how the eddies would respond to the torque, if they were present. Fig. 3.5b shows the NPAC wave breaking frequencies for the *NoTRQ* (black) and *TOTAL* (red) runs, as a function of latitude. The thin, horizontal lines represent the jet latitudes from both runs.

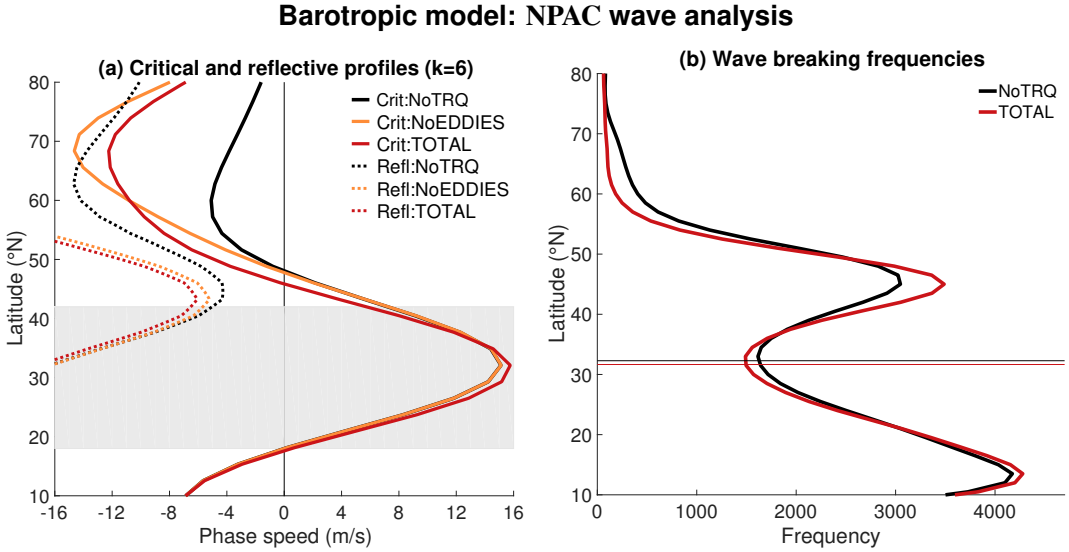

Fig. 3.5. (a) The NPAC critical (solid) and reflective (dotted) profiles for zonal wavenumber $k = 6$. *NoTRQ* is in black, *NoEDDIES* in orange, and *TOTAL* is in red. The thin, grey, horizontal lines indicate the $\phi_s \pm 1\sigma_s$ extent of the Gaussian stirring mask. (b) The NPAC wave breaking frequencies for both *NoTRQ* (black) and *TOTAL* (red). The position of maximum climatological zonal mean zonal winds is indicated by the thin, horizontal lines.

From Fig. 3.2c and Fig. 3.3a, we know that the eddies respond to the torque and act to increase the speed of the jet via increased convergence of westerly momentum into the jet core. Furthermore, from Rossby wave arguments, this could either indicate increased wave breaking on the flanks of the jet in *TOTAL* relative to *NoTRQ*, or decreased wave breaking within the jet itself. We are therefore interested in how the imposed torque changes both the reflective and critical profiles in *NoEDDIES* relative to *NoTRQ*. Looking first at the reflective profiles (dotted curves), we note a small reduction in the *NoEDDIES* reflective profile relative to the *NoTRQ* profile (orange versus black dotted curves). There is a small range of phase speeds, between -5.2 ms^{-1} and -4.3 ms^{-1}, where waves are reflected in *NoTRQ* but would be able to propagate poleward until reaching a critical latitude and breaking in *NoEDDIES*. Therefore, we expect there to be an increase in wave breaking on the poleward flank, and looking at Fig. 3.5b, we see a significant increase in wave breaking on the poleward flank, consistent with the changes to the reflective profiles. There is also a decrease in wave breaking in the jet core due to the same changes in reflective profiles. In *NoTRQ* the reflected waves likely broke once they re-entered the stirring region, whereas in *TOTAL* these waves instead break on the poleward jet flank. While the torque causes the initial relaxation of the reflective profile, the increased wave breaking on the poleward flank decreases the wind speeds and further alters the meridional shear of the zonal wind, relaxing the reflective profile further (red dotted), so that waves with negative phase speeds up to -6.1 ms^{-1} are now able to break on the poleward flank of the jet. While small, this range of phase speeds exhibits a peak in power at $k = 6$ (Fig. 3.4a and b), and thus is considered crucial to the total eddy response.

The imposed torque also changes the critical profiles by enhancing the easterlies north of 50 ^{o}N (Fig. 3.5a, orange versus black solid), meaning waves break at lower latitudes in *TOTAL* than in *NoTRQ*. This change results in even more wave breaking on the poleward flank, at around 45^{o}N, and less wave breaking at higher latitudes, closer to 60^{o}N, as seen in Fig. 3.5b. This decrease in wave breaking at high latitudes is the reason we see increased wind speeds there in Fig. 3.2c.

3.4.1.2 Eddy activity: North Atlantic

For the NATL, Fig. 3.4c and d show that the eddy momentum flux power spectra significantly changes between *NoTRQ* and *TOTAL*, and we found that wavenumber $k = 5$ most clearly demonstrates the eddy response and the reasons for the shift in power from positive to negative phase speeds. We one again focus our analysis on negative phase speeds, as this is where the power is most concentrated when the torque is imposed. As in NPAC, we plot the corresponding critical (solid) and reflective (dotted) profiles in Fig. 3.6a, and the wave breaking frequencies in Fig. 3.6b.

Looking at Fig. 3.6a, we note some similarities to the NPAC experiment. In both experiments,

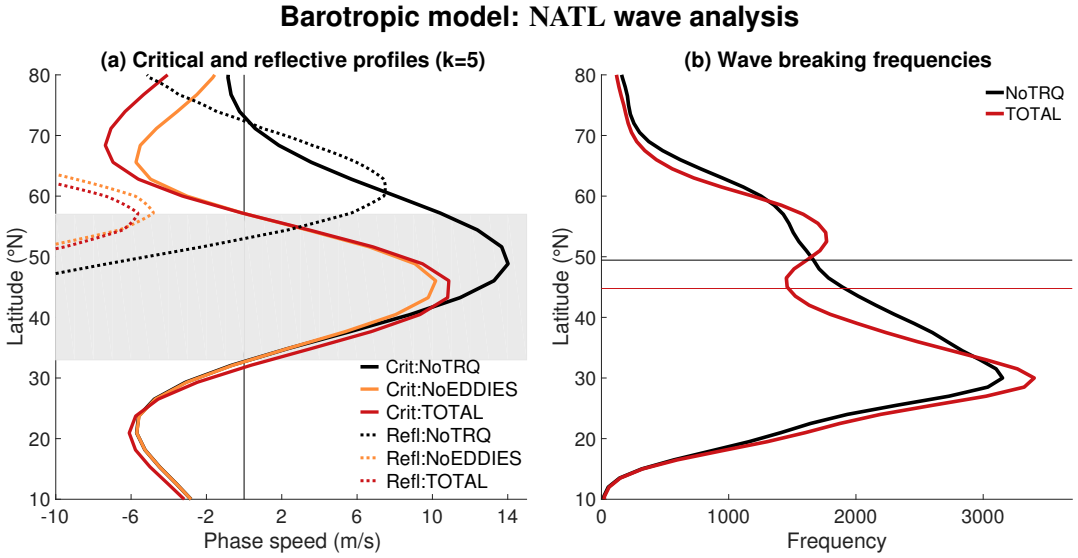

Fig. 3.6. (a) The NATL critical (solid) and reflective (dotted) profiles for zonal wavenumber $k = 5$. *NoTRQ* is in black, *NoEDDIES* in orange, and *TOTAL* is in red. The thin, grey, horizontal lines indicate the $\phi_s \pm 1\sigma_s$ extent of the Gaussian stirring mask. (b) The NATL wave breaking frequencies for both *NoTRQ* (black) and *TOTAL* (red). The position of maximum climatological zonal mean zonal winds is indicated by the thin, horizontal lines.

the biggest changes in reflective and critical profiles occur on the poleward flank of the jet, with enhanced critical profiles in *NoEDDIES* as compared to *NoTRQ* (orange versus black solid) and a relaxed reflective profile (orange versus black dotted). As in NPAC, a reduction in the reflective profile in *NoEDDIES* relative to *NoTRQ* means that waves propagating poleward are able to reach a critical latitude and break, rather than being turned back. This suggests increased wave breaking on the poleward flank of the jet, and decreased wave breaking within the stirring region in *TOTAL* relative to *NoTRQ*, both of which are seen in Fig. 3.6b. In the NATL case, however, the decreased

wave breaking in the jet core in *TOTAL* relative to *NoTRQ* in Fig. 3.6b is much larger and more extensive than in NPAC, and there is a significant increase in wave breaking on the equatorward flank as well.

In the NATL case, the reflective profile in *NoTRQ* (black dotted) is so strong that many waves, especially those with negative phase speeds, are trapped and break within the stirring region. This occurs where the generation region (grey shading) is bounded by the reflective profile (black dotted curve). As a result, the NATL *NoTRQ* case has a great deal of wave breaking occurring within the jet core, as seen in Fig. 3.6b (black curve), with no clear local minima at the jet latitude. The imposed torque narrows the jet significantly on the poleward flank, greatly increasing the meridional wind shear, resulting in a large reduction of the reflective profiles. This means that waves with negative phase speeds are no longer trapped in the generation region in *TOTAL* and can propagate both poleward and equatorward, resulting in increased wave breaking on both flanks of the jet, and decreased wave breaking in the stirring region itself, as evident in Fig. 3.6b (red curve). In addition, in *TOTAL* it is *only* waves with negative phase speeds that can propagate out of the stirring region before encountering a critical latitude (Fig. 3.6a, red curve). Only if a wave breaks outside the generation region is there a net momentum flux, further emphasizing the increased power at negative phase speeds in *TOTAL* relative to *NoTRQ* seen in Fig. 3.4c and d, and explaining the reduction in power at positive phase speeds.

Waves with negative phase speeds exhibit decreased wave breaking in the stirring region in *TOTAL* versus *NoTRQ*, and increased wave breaking outside the stirring region on both flanks of the jet. Both of these changes in wave breaking lead to increased jet speeds via the convergence of westerly momentum into the stirring region. The increased convergence of westerly momentum into the stirring region is associated with increased wave breaking on both flanks of the jet, further enhancing easterlies in these two regions (Fig. 3.2b red versus black). The *TOTAL* wave breaking frequencies now have a clear, local minima in the jet core, a distinct peak on the poleward flank of the jet and an enhanced peak on the equatorward flank (Fig. 3.6b, red curve). The decrease in wave breaking within the stirring region is mostly confined south of the jet latitude (thin, horizontal, red

line), accounting for the increased wind speeds in that region and the slight, equatorward shift of the

3.5 DISCUSSION AND CONCLUSIONS

Using only a zonally symmetric barotropic model, we are able to replicate key aspects of the fully coupled CCSM4 model Northern Hemisphere ocean basin jet stream responses to sea ice loss. Specifically, in the CCSM4, the North Atlantic jet weakens and shifts slightly equatorward, while the North Pacific jet strengthens and extends eastward. The nature of the barotropic model allows us to separate the changes into the direct, forced response, and the response due to eddy feedbacks. Utilizing two experimental setups that represent the two basins, we find that in *both* cases the barotropic eddy-mean flow feedbacks are working to *increase* jet speeds, and that the *net* zonal wind response strongly depends on the jet latitude relative to the imposed forcing. In the North Pacific setup the jet is far enough away from the forcing that the net effect is an increase in jet speed due to the eddies, and the direct response is isolated to the poleward flank. In the North Atlantic setup the jet is closer to the imposed forcing and the net effect is a decrease in jet speed due to the direct response, counteracted by the eddy response. In both cases the eddy response is the same, working to increase the jet speeds and further enhance the easterlies on the poleward flank of the jet via increases in westerly momentum convergence in the jet core. These eddy responses are driven primarily by changes to the reflective profiles, which dictate which waves are turned back and which reach a critical latitude and break. Changes to the critical profiles also affect where waves are preferentially breaking on the poleward flank, and thus, also contribute to the total eddy response.

The two simulated cases shown in this work were chosen for their similarities to the CCSM4 ocean basin jet streams. In testing the sensitivity of the barotropic model results to the placement of the stirring and torque latitudes, we found the eddy response to be consistent for all midlatitude stirring and imposed easterly torques poleward of the jet. In all cases, the eddies strengthen the westerlies in the jet core and to the south, and induce a region of easterly wind anomalies on the poleward flank of the jet. The precise location of the maximum eddy impact on the mean flow

depends on both the latitude of the stirring and how close it is to the torque. Both of these factors strongly influence the reflective profiles, either via planetary or relative vorticity, which, in turn, controls which waves propagate far enough from the jet to break and contribute to the net convergence of eddy momentum flux into the stirring region.

The barotropic eddy-mean flow feedbacks found in this work support the CCSM4 result of increased jet speeds in the North Pacific in response to sea ice loss, although we do not expect them to be the full story in the more complex system. As seen in the highly idealized barotropic model, the application of a strong easterly torque only results in small increases in jet speeds in the North Pacific experiment, nowhere near the increase seen in the CCSM4. However, baroclinic feedbacks between changes in wave propagation and wave generation are almost certainly at play within the coupled system, and are not included in our barotropic model set-up. Barnes and Thompson (2014) showed that adding a baroclinic feedback by allowing for slight shifts of the stirring region is key in determining the magnitude of the zonal wind response to forcing, with barotropic feedbacks setting the structure and sign of the response. It is also possible that there are additional feedbacks associated with a change in the strength of the baroclinic zone in response to external forcing, which would be of interest to examine further.

The level of complexity in the CCSM4 experiment suggests that there may be many additional mechanisms at play, and the wide range of model responses to climate forcings shown in previous work mean that one model may not be considered representative of the true atmospheric circulation response (e.g. Zappa et al. 2018). However, the findings of this work and the increased understanding of the barotropic mechanisms involved highlight the role of barotropic eddy-mean flow feedbacks in driving the jet stream response to Arctic amplification and sea ice loss. Further, the same eddy-mean flow feedbacks are present in two very different experimental set-ups, and the results stress the importance of jet latitude in determining the net response to forcing.

The authors would like to thank Lantao Sun for providing the CCSM4 data, and the four anonymous reviewers whose comments were exceedingly helpful in improving this work. The authors are supported by the Climate and Large-scale Dynamics Program of the National Science Foundation under Grant AGS-1545675.

4 North Pacific zonal wind response to sea ice loss in the Polar Amplification Model Intercomparison Project and its downstream implications[3]

Recent studies suggest that the wintertime North Pacific eddy-driven jet stream will strengthen and extend eastward in response to Arctic sea ice loss. Using output from the Polar Amplification Model Intercomparison Project we examine both the mean change of the North Pacific wintertime zonal winds, as well as the change in sub-seasonal, wintertime variability in zonal winds between experiments with future Arctic sea ice concentrations relative to a pre-industrial run. Further, given the relationship between the North Pacific jet stream and North American weather regimes, we also examine the changes in surface temperature variability over North America. The four climate models investigated here exhibit robust agreement in both sign and structure of the atmospheric responses, with a strengthened wintertime North Pacific jet, an increase in anomalously strong and extended jet events, and a decrease in weakened and equatorward-shifted jet events in response to reduced Arctic sea ice. Consistent with the changes seen in the North Pacific, the models also show an increase in the frequency of the North American temperature dipole, with anomalously warm temperatures in the west or northwest, and anomalously cold temperatures in the east or southeast, and a decrease in anomalously cold temperatures over North America.

4.1 INTRODUCTION

Many recent studies have examined the impacts of Arctic warming and sea ice loss on both the Northern Hemisphere large scale circulation (e.g. Ronalds et al. 2018; Screen et al. 2018b,a; Zappa et al. 2018; Blackport and Screen 2019; Ronalds and Barnes 2019) and midlatitude weather regimes (e.g. Sellevold et al. 2016; Cohen et al. 2018; Overland and Wang 2018a,b; Li and Luo 2019). Much of the work looking at the midlatitude eddy-driven jet streams has shown that, both in the zonal mean and over the North Atlantic basin, the eddy-driven jet stream weakens and shifts equatorward in response to Arctic amplification (e.g. Screen et al. 2018b). Recent work by

[3]This chapter contains material which will be submitted.

Ronalds and Barnes (2019), however, showed that the midwinter (January-February) mean North Pacific eddy-driven jet stream strengthens and extends in response to Arctic amplification in a fully coupled climate model, with no change in jet latitude. The exact mechanisms leading to this North Pacific response have not been determined, though certain changes in wavebreaking have been shown to cause a strengthened jet in idealized modeling experiments (Ronalds and Barnes 2019). If the wintertime mean North Pacific jet does indeed strengthen and extend in response to Arctic amplification, this could have downstream impacts on North American temperatures and precipitation (e.g. Strong and Davis 2008), particularly if any mean changes in the wintertime jet stream are also associated with changes in the storm track's sub-seasonal variability.

One hypothesis concerning the possible impacts of Arctic sea ice loss on the atmospheric circulation is that it will lead to changes in Northern Hemisphere midlatitude weather regimes via alteration of the large-scale atmospheric circulation (e.g. Kug et al. 2015; Lee et al. 2015; Cvijanovic et al. 2017; Li and Luo 2019). Of growing interest is the role of Arctic sea ice loss in the North American wintertime temperature dipole, defined as anomalously warm temperatures in the west and severe cold to the east (e.g. Wang et al. 2015a,b; Lee et al. 2015; Cvijanovic et al. 2017; Wang et al. 2017; Chien et al. 2019). This temperature pattern occurs when the wintertime climatological North American geopotential height ridge/trough pattern becomes strongly amplified and persistent, leading to anomalously warm and dry weather conditions in the west and severe cold temperatures in the east (e.g. Wang et al. 2015a,b; Singh et al. 2016). While this ridge/trough pattern is associated with both topography and land-sea contrast, recent studies have argued that the North Pacific circulation is the dominant factor in its amplification and persistence (e.g. Teng and Branstator 2017; Swain et al. 2017), and others have showed an indirect link between Arctic sea ice loss and the amplified ridge/trough pattern (Lee et al. 2015; Cvijanovic et al. 2017). We therefore hypothesize that any changes to the North Pacific zonal wind field will have associated downstream impacts for North American weather. Specifically, changes in the North Pacific may lead to increased cold air outbreaks (e.g. Kug et al. 2015), or possibly increased frequency of the warm west/cold east temperature dipole (e.g. Lee et al. 2015; Chien et al. 2019).

Given the previous findings of a strengthened and extended North Pacific jet stream in response

to Arctic sea ice loss (Ronalds et al. 2018), and the work linking the atmospheric circulation in the North Pacific to North American weather regimes (e.g. Jaffe et al. 2011; Lee et al. 2015; Griffin and Martin 2017; Swain et al. 2017; Chien et al. 2019), we are interested in exploring the change in sub-seasonal variability of both the zonal winds over the North Pacific and the surface temperatures over North America in response to Arctic sea ice loss. While there has been numerous studies examining the regional atmospheric impacts of Arctic sea ice loss in recent decades, there is still considerable uncertainty in the possible consequences of Arctic warming and sea ice loss (see Screen et al. 2018b; Smith et al. 2019; Cohen et al. 2020, and references therein). While much of the uncertainty derives from poor understanding of the particular physical mechanisms and the large internal variability associated with atmospheric circulations and regional weather, there is also considerable uncertainty stemming from differences between modeling experiments (Smith et al. 2019). This is addressed in the sixth Coupled Model Intercomparison Project (CMIP6; Eyring et al. 2016) by coordinating a Polar Amplification Model Intercomparison Project (PAMIP; Smith et al. 2019). The goal of the project is to coordinate a multi-model sea ice loss and Arctic warming set of experiments. Each modeling centre is given identical forcing files and follows the same experimental protocol, giving an unprecedented set of coordinated sea ice loss experiments across multiple climate models (see Smith et al. 2019, for more information). This work aims to answer the following questions using output from PAMIP:

(1) How does the wintertime North Pacific eddy-driven jet stream respond to the same Arctic sea ice loss across multiple models?
(2) What changes in the internal variability make up the wintertime mean jet stream response?
(3) Do we see consistent changes in downstream surface temperatures associated with the changes to the North Pacific eddy-driven jet?

4.2 DATA AND METHODS

4.2.1 Data

The Polar Amplification Model Intercomparison Project (PAMIP) is a subset of ongoing CMIP6 experiments. The goal of the project is to identify the forced response of the global climate system

to changes in polar sea ice, as well as differentiate the relative roles of local sea ice concentrations (SIC) versus remote sea surface temperatures (SST) in driving polar amplification. To this end, numerous experiments were constructed, with tier classifications. Tier 1, the first experiments to be run, consist of atmosphere-only time slice experiments. All experiments are initialized using conditions from April 1st, 2000 and are run for 14 months, discarding the first two months as spin-up. Each climate model produces at least 100 ensemble members per run, and the method of ensemble generation differs between each model. Each experiment has one forcing change, either sea surface temperature (SST) conditions or sea ice concentration (SIC) conditions. There are three categories for both the SST and SIC conditions: pre-industrial, present day or future. The pre-industrial and future conditions are based on the multi-model ensemble historical and RCP8.5 runs from CMIP5, and present day conditions are taken from observations. For more information on the experimental set-ups and the derivations of the forcing files see Smith et al. (2019).

In this work we compare results from two of the Tier 1 experiments (labeled 1.5 and 1.6). Experiment 1.5 consists of present day SST's and pre-industrial Arctic sea ice, while experiment 1.6 also consists of present day SST's but with future Arctic sea ice. For the remainder of this work these two experiments will be referred to as piArcSIC (1.5) and futArcSIC (1.6). Four models provide daily data for these two experiments: CESM2 (Gettelman et al. 2019), CanESM5 (Swart et al. 2019), HadGEM3 (Walters et al. 2019) and SC-WACCM (Smith et al. 2014). More information for each model is provided in Table B.1 in Appendix B. CESM2, CanESM5 and SC-WACCM each contain 100 ensemble members per run, generated by perturbing the initial temperatures (perturbations are on the order of 10^{-14}K), while HadGEM3 has 150 members generated using the stochastic physics method (see Ciavarella et al. 2018, for more details).

We use daily zonal winds at 700 hPa (U700) over the North Pacific basin (5-85 ^{o}N, 120-240 ^{o}E) and daily surface temperatures (T_s) over North America (5-85 ^{o}N, 200-320 ^{o}E). Because our interest is in the sub-seasonal time scale, both the winds and surface temperatures are temporally smoothed using a 10-day low-pass Lanczos filter before we limit our data to midwinter only (January-February). The results are qualitatively similar when using either a 5-day or 7-day filter, although they are much noisier. We chose to omit December and March from the wintertime

analysis as the monthly mean North Pacific zonal wind fields were significantly different from the January-February means and so focus only on the consistent midwinter response. All four models have daily U700 data, but at this time we only have daily surface temperatures for CESM2, CanESM5 and HadGEM3. In order to test for significance when examining the change in North Pacific U700 we use the Wilks (2016) False Discovery Rate (FDR) method, which accounts for the large spatial autocorrelation in the data. To apply this method you must first define the α_{FDR}, which depends on the scale of autocorrelation. In this case we used $\alpha_{FDR} = 2\alpha_{global}$. Next, the p-value at all gridpoints is calculated using a Student's two-sample t-test. Using α_{FDR} we define the FDR criterion (eq. 4.1), which acts as a threshold for the new p_{FDR}-value, where the calculated p-values are no longer less than FDR_{crit}.

$$FDR_{crit} = \frac{i}{N}\alpha_{FDR}, \quad \text{where} \quad i = 1, ..., N \tag{4.1}$$

4.2.2 Cluster Analysis

In order to examine the modes of internal variability within our data we perform a cluster analysis technique known as k-means clustering (Hartigan and Wong 1979). K-means cluster analysis categorizes the entirety of a data set into a user-specified number of clusters (or centroids). Thus, there is some subjectivity in the number of centroids chosen, which will be discussed further below. The algorithm is straightforward to apply to large datasets, and there are no orthogonality constraints as in Empirical Orthogonal Functions, though the classification is more rigid, with each day belonging to a single centroid. The algorithm operates iteratively, assigning individual data points to the closest centroid, defined as the centroid with the minimum squared Euclidean distance (Hartigan and Wong 1979). At each iteration, the centroids move to the middle of the data points they represent, and the new minimum distances are calculated. This process is repeated until the centroids remain nearly stationary, at which point the algorithm stores the centroids and the distances. In this study, we repeat this entire training process 500 times in order to ensure that a global, rather than local, minimum is found. The resulting centroids chosen from the 500 iterations are from the iteration with the minimum summed distance.

Before performing the cluster analysis we first calculated the daily anomalies of both the piArcSIC (pre-industrial Arctic sea ice) and futArcSIC (future Arctic sea ice) experiments. This was done by removing the ensemble mean for each day, i.e. remove the ensemble mean for January 1st from all ensemble members, then do the same for January 2nd, and so on, in each experiment separately (piArcSIC versus futArcSIC). By removing the daily means rather than a single January-February climatology we eliminate any seasonality bias from the data, ensuring that the resulting clusters will not be skewed towards the beginning of January versus end of February. Doing this to both experiments separately also implies that we have removed the mean forced change and can combine the resulting anomalies. For CESM2, CanESM5 and SC-WACCM this means we have two experiments, each with 100 ensemble members of 59 days (January-February, no leap years), giving us 11,800 daily anomalies. For HadGEM3, we have 150 ensemble members of 60 days (30-day months), giving us 18,000 days. The k-means cluster analysis is then applied to the full pool of daily anomalies for each model separately. In order to choose the number of clusters we tested a range from 4-9 using the daily U700 anomalies and compared the resulting centroids from each model. Ultimately, six centroids appeared to be sufficient to account for the typical variability within the data while also ensuring the centroids remained distinct.

Applying this process to the North Pacific U700 daily anomalies results in six centroids that represent the six maps of zonal wind anomalies that best describe the main patterns of variability about the mean. The algorithm also outputs the categorization of each input day into its respective cluster. Separating the input days back into the two experiments, piArcSIC and futArcSIC, we can calculate the frequencies of occurrence of each cluster: how many days from each experiment look like each centroid? This allows us to compare the frequencies from piArcSIC and futArcSIC and see if certain clusters, or zonal wind anomaly patterns, become more or less frequently visited with Arctic sea ice loss. The significance of these frequency changes is tested using a bootstrapping approach whereby we shuffle days from both experiments together and randomly split the data in half and recalculate the cluster frequency change between each half. This process is repeated 10,000 times, and the resulting distribution of frequency changes define the null distribution. We then choose as our cutoff the two-tailed 80% and 90% confidence regions.

The same k-means cluster analysis is also applied to the North American daily anomalous surface temperatures from both experiments. For consistency with our North Pacific zonal wind analysis six centroids were again chosen, and significance was tested using the same bootstrapping approach.

4.3 RESULTS

4.3.1 North Pacific zonal wind variability

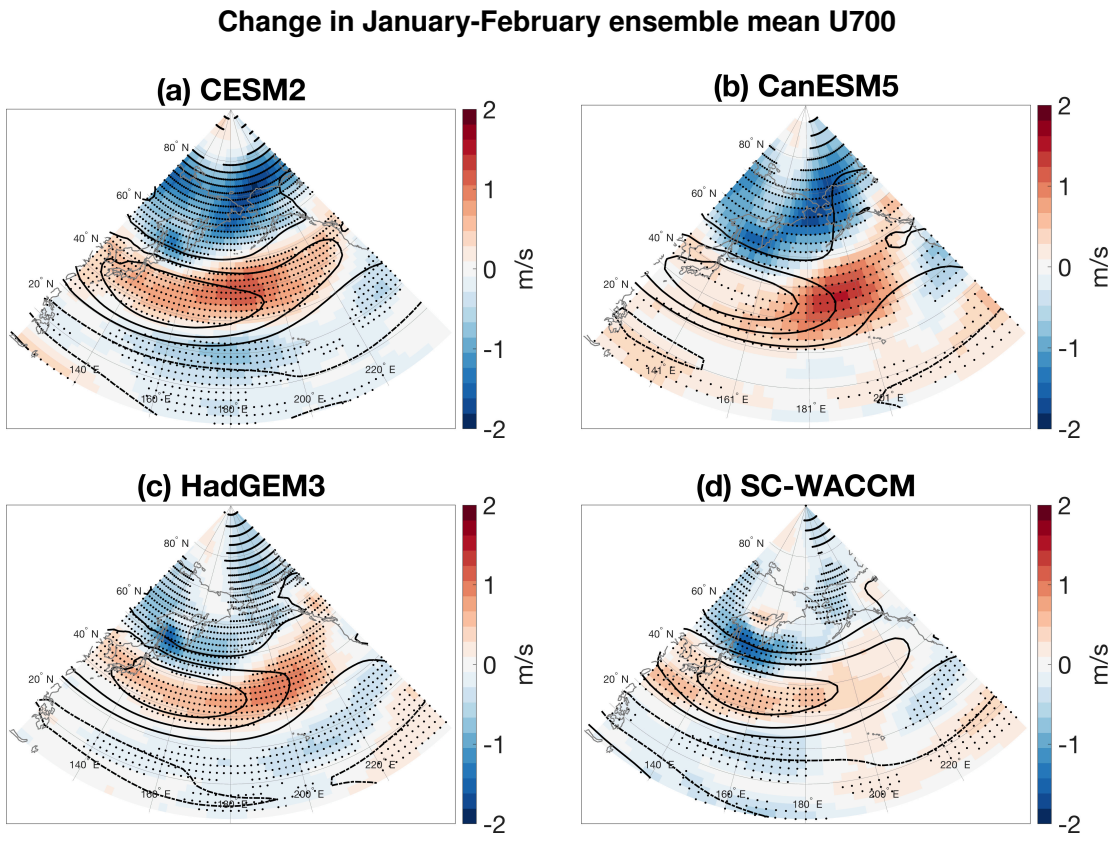

Fig. 4.1. The change in January-February ensemble mean zonal wind at 700 hPa across the North Pacific basin between futArcSIC and piArcSIC for (a) CESM2 ($n = 5900$), (b) CanESM5 ($n = 5900$), (c) HadGEM ($n = 9000$), and (d) SC-WACCM ($n = 5900$). Shading denotes wind change and contours denote the piArcSIC mean. Black dots represent FDR significance at the 99% confidence level.

The change in the ensemble mean January-February mean zonal winds at 700 hPa (U700) across the North Pacific basin is shown in Fig. 4.1, represented by the shading. The contours in Fig. 4.1 represent the piArcSIC mean U700, and the black dots represent the FDR significance at the 99% confidence level. All four models show a significantly strengthened and extended North

Pacific jet stream (red shading) in the futArcSIC experiment, with strong easterly anomalies along the poleward flank (blue shading). CESM2, HadGEM3, and SC-WACCM (Fig. 4.1a, c, d) also exhibit easterly anomalies along the equatorward flank of the jet. None of the models show evidence of a shifted jet in the North Pacific.

Next, we decompose the mean change in U700 into the change in sub-seasonal variability using the k-means clustering analysis described above (Hartigan and Wong 1979), and compare it to the k-means cluster analysis of the surface temperatures (see next section). This is done for all four models individually, and we find that all four result in broadly similar patterns in which we group the North Pacific U700 centroids. The k-means cluster analysis of North American T_s also result in similar centroids for CESM2, CanESM5 and HadGEM3, allowing us to broadly define the six main patterns of T_s variability across all of the models. Due to these strong similarities, we only show the results from CESM2 for the remainder of the paper as they are representative of all four models, though we include comparisons across models in Appendix B (Figures B.1-B.8).

The six centroids representing the main patterns of variability in the North Pacific daily anoma-

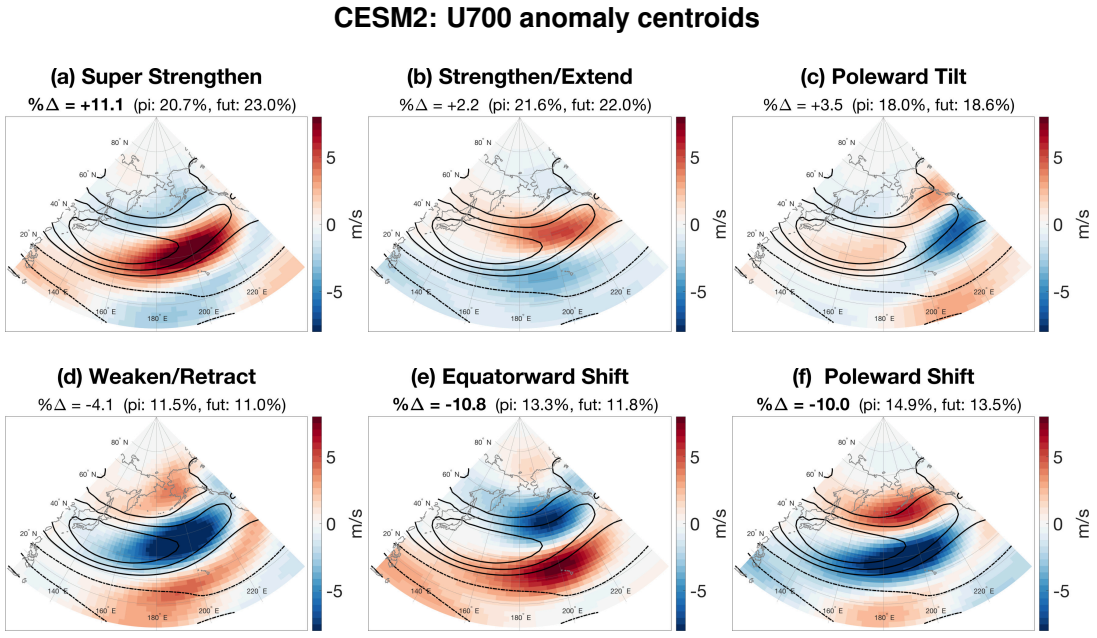

Fig. 4.2. The six main patterns of daily anomalous U700 variability for January-February (shading). Contours represent the piArcSIC January-February mean U700, and bold face on the %Δ represents significance at 90% confidence. All results are for CESM2.

lous U700 in CESM2 are shown in Fig. 4.2. Each pattern is given a descriptor which will be used throughout the remainder of this paper:

(a) Super Strengthen: jet is extremely strong, extended eastward, and more zonal and/or shifted equatorward slightly.

(b) Strengthen/Extend: jet is strong, extended eastward, and shifted slightly poleward, particularly in the exit region.

(c) Poleward Tilt: jet is strong, and the exit region is dominantly shifted poleward.

(d) Weaken/Retract: jet is retracted, confined mostly to the west Pacific, and weakened.

(e) Equatorward Shift: jet is shifted equatorward, and weakened in some models, particularly SC-WACCM (see Fig. B.2 in Appendix B).

(f) Poleward Shift: jet is weakened and shifted poleward.

In CESM2, the three strengthening patterns resulting from k-means cluster analysis all increase in frequency in futArcSIC relative to piArcSIC (Fig. 4.2a-c). Conversely, the three weakened and/or shifted jet patterns all decrease in frequency. While in CESM2 only the Super Strengthen, Equatorward Shift and Poleward Shift patterns (Fig. 4.2a, e, f) are considered significant at the 90% confidence level (indicated by the bold $\%\Delta$ in the titles), we can compare the changes in frequency of the similar patterns across all four models. We show these in Fig. 4.3, where each bar indicates the percent change in frequency of each pattern in futArcSIC relative to piArcSIC for all four models. We have included two thresholds for significance calculated using a bootstrapping approach: 80% confidence, denoted by the darker colour bars and the single asterisk, and 90%, denoted by the double asterisk. While 80% confidence is a lower threshold than commonly used, any multi-model agreement further increases our confidence in the changes in frequency. The three strengthened jet patterns are shown in Fig. 4.3a, while the three weakened jet patterns are shown in Fig. 4.3b.

All four models show sign agreement in the percent change of frequency for the Super Strengthen (increased, Fig. 4.3a), Poleward Tilt (increased, Fig. 4.3a), and Equatorward Shift (decrease, Fig. 4.3b) patterns. Further, the majority of the models show significance of at least 80% for these three patterns, increasing our confidence that this variability response is forced by the Arctic sea ice loss, rather than just noise. Of the other three patterns, we consider any changes

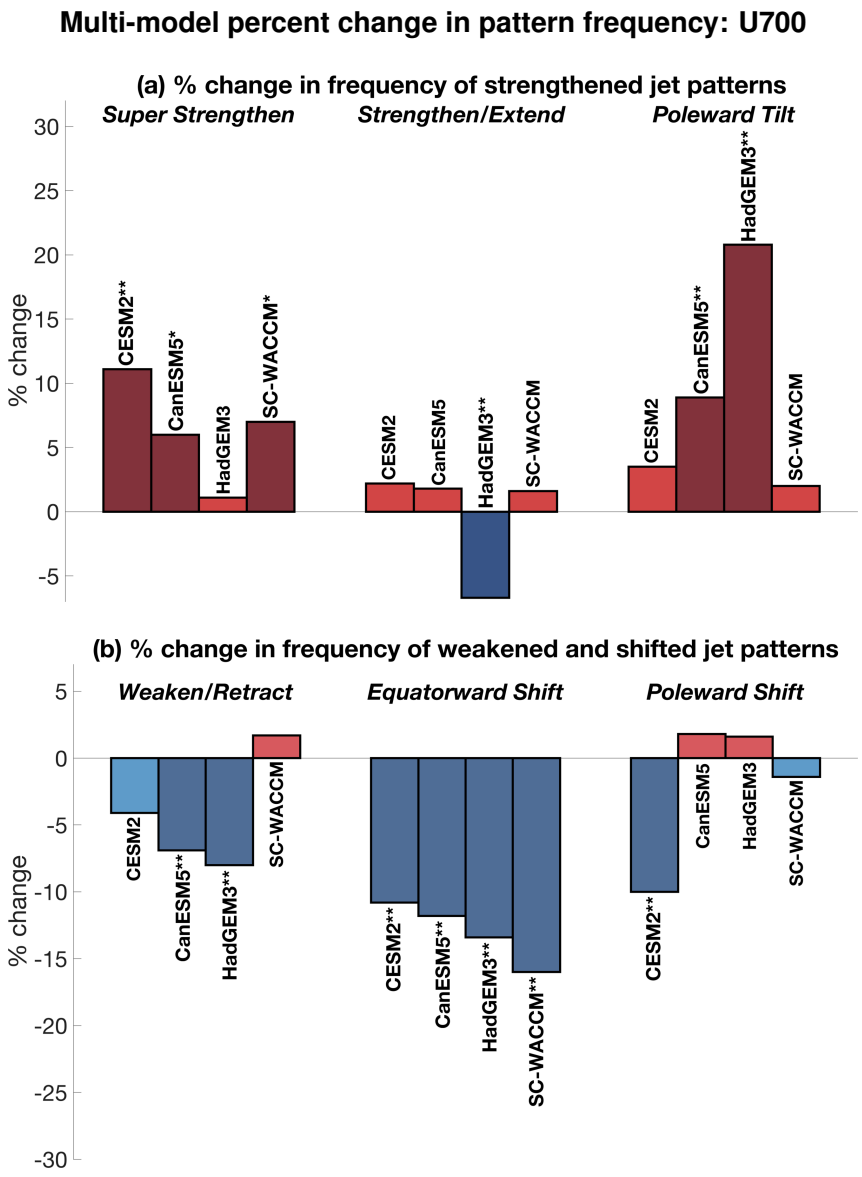

Fig. 4.3. The percent change in frequency between futArcSIC and piArcSIC of each pattern of daily anomalous U700 variability for all four models: CESM2, CanESM5, HadGEM3, and SC-WACCM (left to right). The centroids from each model's k-means analysis are grouped into types: (a) Super Strengthen, Strengthen/Extend, and Poleward Tilt, and (b) Weaken/Retract, Equatorward Shift, and Poleward Shift. Darker coloured bars and a single asterisk on the model name represent significance at the 80% confidence level, and the double asterisk represents significance at the 90% confidence level.

seen in Strengthen/Extend (Fig. 4.3a) and Poleward Shift (Fig. 4.3b) to not be significant as the changes in frequency are small and there is substantial model disagreement. The Weaken/Retract pattern (Fig. 4.3b), however, is complicated by the fact that in SC-WACCM there were two centroids that exhibited signifiant jet retraction and weakening, the one we labeled Weaken/Retract,

which increased very slightly, and the centroid we labeled Equatorward Shift, which decreased significantly (see Fig. B.2 in Appendix B). This, coupled with the 90% confidence in decreased frequency for both CanESM5 and HadGEM3, suggests that the decreased frequency of this pattern may also be a robust forced variability response to Arctic sea ice loss.

Figure 4.2 and Fig. 4.3 suggest that the strengthened and extended mean January-February

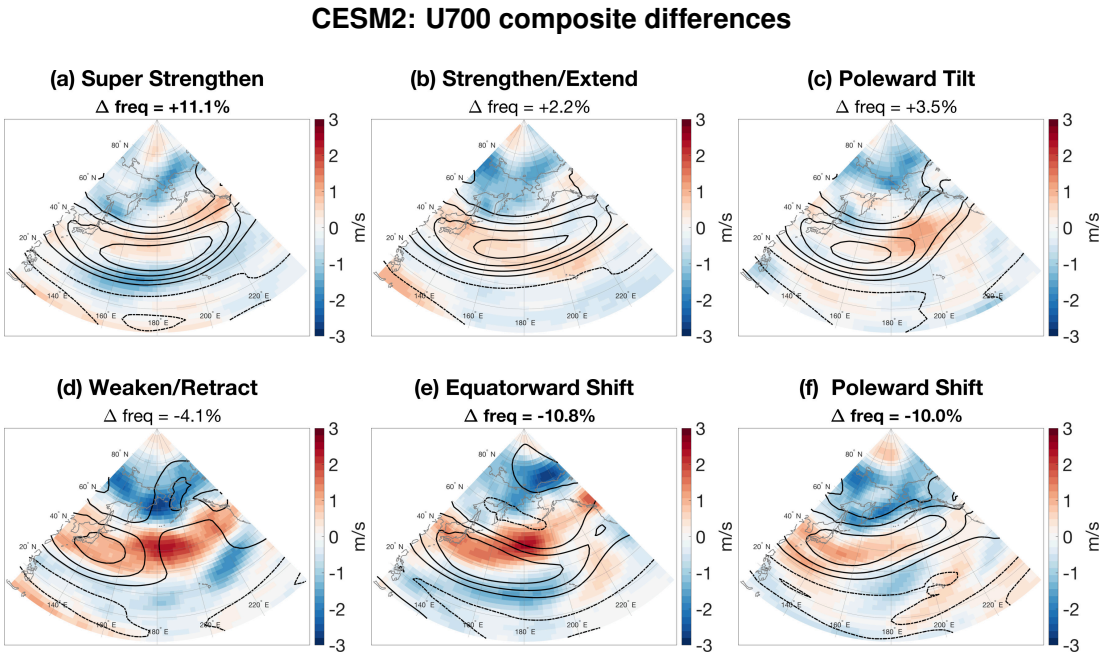

Fig. 4.4. Difference between futArcSIC and piArcSIC full field U700 composite maps, based on the daily anomalous U700 variability patterns (shading). Contours represent the piArcSIC daily U700 composite maps, and bold face on the Δfreq represents significance at 90% confidence. All results are for CESM2.

North Pacific jet seen in Fig. 4.1 is due to an increase in strengthened and extended jets (Super Strengthen and Poleward Tilt patterns, Fig. 4.2a, c), and a decrease in weakened and retracted jet events (Weaken/Retract and Equatorward Shift patterns, Fig. 4.2d, e). We can also use the output of the k-means cluster analysis to determine if, on any given day in futArcSIC, the winds are stronger than a similar day in piArcSIC. In other words, we want to know if the futArcSIC days assigned to each centroid have different full wind fields than the piArcSIC days, particularly in the jet region. To answer this, we use the classification of each day to a specific cluster to create composite maps of the full, North Pacific U700 field for each cluster for both piArcSIC and futArcSIC separately and take the difference. These are shown in Fig. 4.4, where shading represents the difference

in wind field composites and contours represent the piArcSIC composites. For all six patterns in CESM2 there are stronger winds in the vicinity of the jet in futArcSIC (red shading), and generally weakened winds elsewhere (blue shading). Again, this is true for each of the six patterns across all four models (see Figures B.3-B.4 in Appendix B). Further, the biggest differences in full wind fields occur in the three weakened jet patterns: Weaken/Retract, Equatorward Shift, and Poleward Shift (Fig. 4.4d-f). This suggests that not only is the jet generally stronger on a day-to-day basis in the futArcSIC experiment in response to Arctic sea ice loss, but that days characterized as retracted and weak jet events, or shifted jet events, have much faster jets than their piArcSIC counterparts.

In the January-February mean, the North Pacific jet is strengthened and extended in response to Arctic sea ice loss across all four models (Fig. 4.1). This increased jet strength represents not only a generally faster jet on a day-to-day basis (Fig. 4.4), but also an increase in individual strengthened jet events and a decrease in weakened and/or shifted jet events (Fig. 4.2). Based on the results shown in Fig. 4.3, and the level of model agreement, it appears that Arctic sea ice loss is leading to significant changes in frequency of certain sub-seasonal variability patterns. There is an increased frequency in Super Strengthen and Poleward Tilt patterns, and a decreased frequency in Weaken/Retract and Equatorward Shift patterns. This is of interest in terms of downstream impacts. As discussed previously, many studies have looked at the relationships between the North Pacific jet stream variability and North American weather regimes. Notably, Griffin and Martin (2017) found that a strengthened and extended North Pacific jet (similar to our Super Strengthen pattern) is associated with a strong ridge formation along the North American west coast, and the development of the North American temperature dipole, with anomalously warm temperatures in the west and anomalously cold temperatures in the east. Weaken/Retract jet events were found to be associated with the opposite temperature dipole, with a cold west coast and warm east coast, and the Equatorward Shift pattern was associated with anomalously cold air over the northern half of North America (Griffin and Martin 2017, their Figures 4, 5 and 7). These findings, in conjunction with our own, suggest that Arctic sea ice loss in these PAMIP experiments may lead to changes in North American surface temperature variability.

4.3.2 Downstream surface temperature variability

If the same relationships between the North Pacific jet stream and North American surface temperatures found by Griffin and Martin (2017) hold true in the PAMIP atmosphere-only experiments, we would expect that in futArcSIC there will be an increase in the North American temperature dipole and a decrease in both anomalous cold temperatures over North America as well as the opposite temperature dipole, with a cold west/warm east. In order to establish whether the relationships are found in the models we use the results of the North Pacific anomalous U700 k-means cluster analysis for CESM2, CanESM5 and HadGEM3. Once again, the CESM2 results are shown as representative of the three models (see Figures B.5-B.8 in Appendix B for all three models' T_s variability results). Using the days assigned to each pattern for the piArcSIC experiment, we calculate the composite maps of the downstream, North American surface temperature daily anomalies associated with each North Pacific U700 variability pattern (Fig. 4.5). The shading represents the composite daily anomalies of T_s, and the contours represent the piArcSIC January-February climatology. As in Fig. 4.2-Fig. 4.4 the three strengthened jet patterns are in the top row (Fig. 4.5a-c), and the three weakened jet patterns are in the bottom row (Fig. 4.5d-f). The patterns whose frequency changes were considered significant, and thus a forced response to Arctic sea ice loss, have the percent changes in frequency bolded in the title (Fig. 4.5a, c, d, and e).

Figure 4.5 shows that the relationships shown in Griffin and Martin (2017) are also found in the CESM2 PAMIP experiments, and the same is true of the other models (see Fig. B.5-B.6 in Appendix B). The Super Strengthen jet events are associated with the warm west/cold east North American temperature dipole (Fig. 4.5a), the Weaken/Retract jet events are associated with cold temperatures in the north and northwest and warm temperatures in the south and southeast (Fig. 4.5d), and the Equatorward Shift pattern is associated with cold temperature anomalies over most of the continent and anomalously warm temperatures over northern Alaska (Fig. 4.5e). The Poleward Tilt pattern is associated with anomalously warm temperatures over Alaska and western Canada, and cool temperatures to the south (Fig. 4.5c). Thus, we expect that in futArcSIC we would see an increased frequency of temperature patterns with warm temperatures to the west

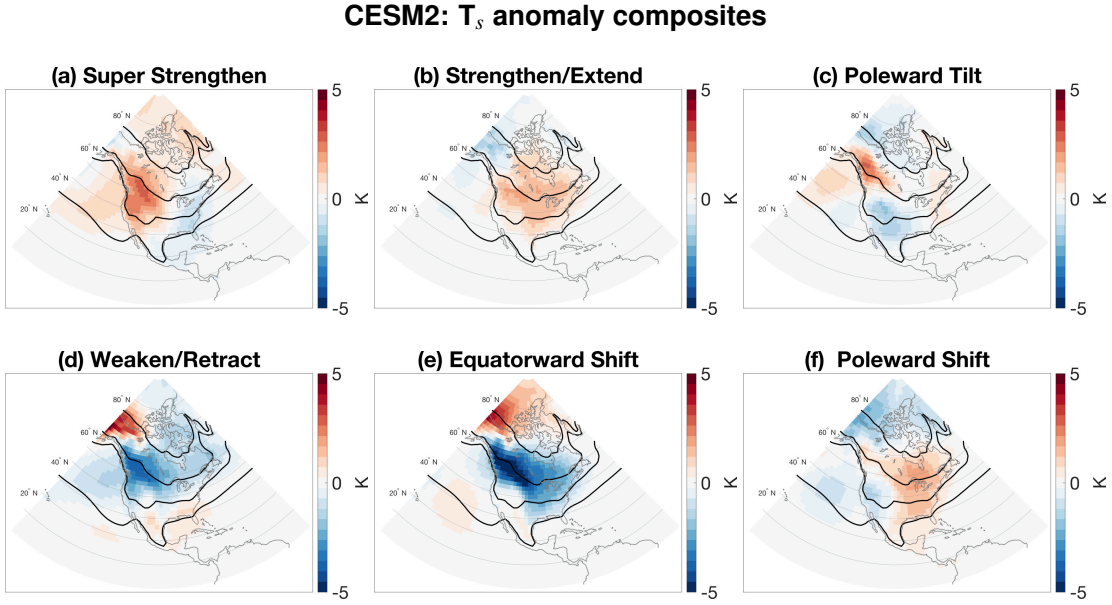

Fig. 4.5. Composite maps of daily anomalous North American T_s from the piArcSIC experiment, based on the daily anomalous U700 variability patterns (shading). Contours represent the piArcSIC January-February mean surface temperatures. All results are for CESM2.

and northwest and cold temperatures to the east and south (Fig. 4.5a, c). We also expect to see a decreased frequency of anomalously cold temperatures over North America (Fig. 4.5d, e). To test this we next apply our cluster analysis approach to the daily surface temperature anomalies over North America.

Similar to the k-means cluster analysis done for the North Pacific U700 anomalies, we remove the daily ensemble means from both piArcSIC and futArcSIC daily T_s fields and combine the resulting anomalies. For consistency, we again use six centroids to describe the six main patterns of variability within the North American surface temperatures, allowing for a comparison to the composite patterns shown in Fig. 4.5. Again, we show results from CESM2 as representative of all three models, since the centroids for each model were broadly similar for all six patterns (see Figures B.7-B.8 in Appendix B). The resulting patterns are shown in Fig. 4.6 for CESM2, with the top row resembling Fig. 4.5a-c and the bottom row closely resembling Fig. 4.5d-f. The shading represents the daily anomaly patterns associated with each centroid, and the contours are the piArcSIC January-February climatology. Frequency changes considered significant at the 90% confidence level are bolded in the titles. Each centroid is assigned to a distinct pattern, which will be used in

the remainder of this paper. The six main patterns of daily anomalous T_s variability over North America are as follows:

(a) Warm W/Cold E: warm temperatures in the west and cool temperatures in the east. This is the amplified Janaury-February climatology pattern, i.e. the North American temperature dipole.

(b) Warm Air Outbreak: strong warm temperature anomalies over Canada and northern U.S.A.

(c) Warm NW/Cold SE: anomalously warm temperatures over Alaska and northwest Canada, and anomalously cold temperatures over the rest of the continent.

(d) Cold NW/Warm SE: anomalously cold temperatures over Alaska and western Canada, with anomalously warm temperatures over most of U.S.A.

(e) Cold Air Outbreak: anomalously cold temperatures over most of North America, with warmer temperatures over northern Alaska.

(f) Warm East: anomalously warm temperatures over the eastern half of North America.

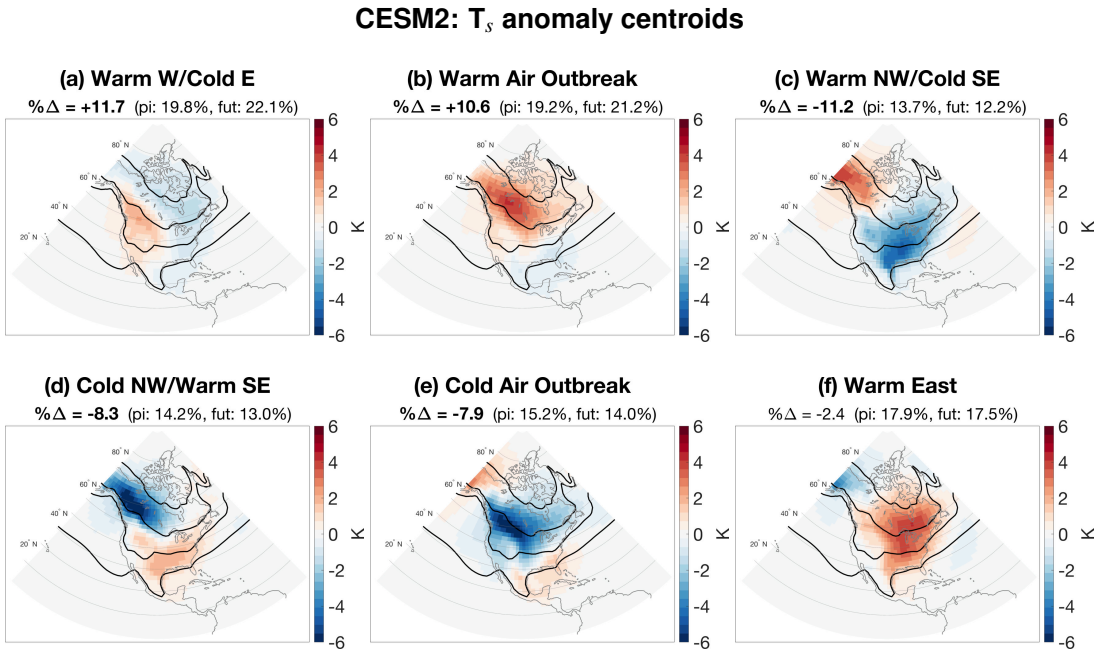

Fig. 4.6. The six main patterns of daily anomalous North American T_s variability for January-February (shading). Contours represent the piArcSIC January-February mean T_s, and bold face on the %Δ represents significance at 90% confidence. All results are for CESM2.

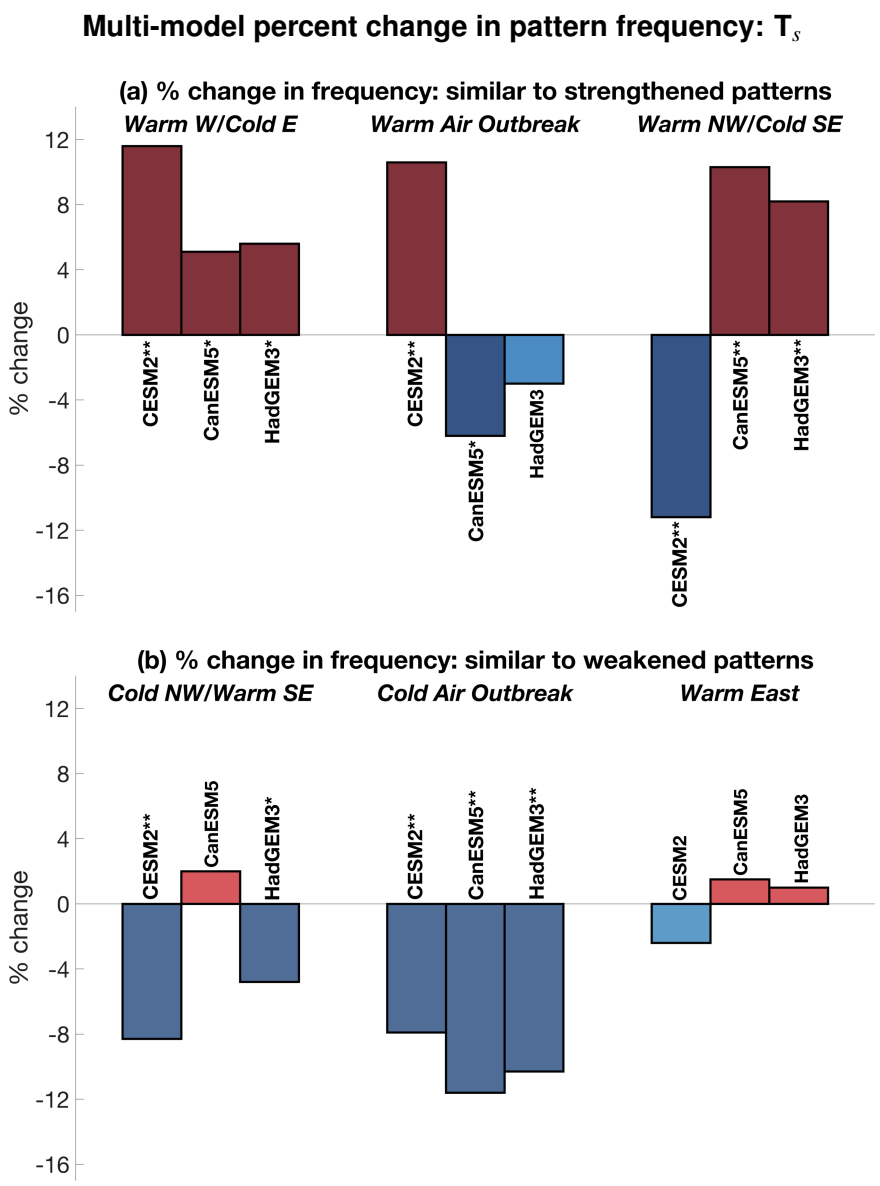

Fig. 4.7. The percent change in frequency between futArcSIC and piArcSIC of each pattern of daily anomalous T_s variability for three models: CESM2, CanESM5, and HadGEM3 (left to right). The centroids from each model's k-means analysis are grouped into types: (a) Warm W/Cold E, Warm Air Outbreak and Warm NW/Cold SE, and (b) Cold NW/Warm SE, Cold Air Outbreak and Warm East. Darker coloured bars and a single asterisk on the model name represent significance at the 80% confidence level, and the double asterisk represents significance at the 90% confidence level.

As expected, we see increased frequency of the Warm W/Cool E pattern (Fig. 4.6a), and decreased frequencies of both the Cold NW/Warm SE pattern (Fig. 4.6d) and the Cold Air Outbreak pattern(Fig. 4.6e). However, the Warm NW/Cold SE pattern in Fig. 4.6c, which most closely resembles the T_s composite from the Poleward Tilt pattern (Fig. 4.5c), significantly decreases in

frequency. This is opposite to what we had expected based on the increased frequency of the Poleward Tilt pattern across all models (Fig. 4.3a) and its associated T_s anomaly composite (Fig. 4.5c).

Figure 4.7 shows the percent change in frequencies for each of the six patterns for all three models. As in Fig. 4.3, darker colours and the single asterisk represent significance at 80% confidence, and the double asterisk represents significance at the 90% confidence level. The Warm W/Cold E pattern (first cluster in Fig. 4.7a) increases significantly across all three models, which is consistent with the increased frequency of the Super Strengthen pattern (Fig. 4.3a). Additionally, the Cold Air Outbreak pattern (second cluster in Fig. 4.7b) decreases in frequency in all three models at the 90% confidence level, again consistent with the decreased frequency of the Equatorward Shift pattern in Fig. 4.3b. Interestingly, both CanESM5 and HadGEM3 show a significant increase in frequency of the Warm NW/Cold SE temperature pattern (Fig. 4.7a), while, as previously noted, CESM2 shows a significant decrease (all are at 90% confidence). While this could be due to model differences, or differences between centroids grouped to the same pattern, it is interesting to note that CanESM5 and HadGEM3 were the only two models that showed significance, again at 90%, in the increased frequency of the Poleward Tilt pattern in Fig. 4.3a, which is consistent with their increased frequencies in the Warm NW/Cold SE pattern.

4.4 DISCUSSION AND CONCLUSIONS

This work uses recently available results from four models running the PAMIP atmosphere-only, time-slice experiments. We compare two sets of experiments, future versus pre-industrial, both with present day sea surface temperature forcing but differing Arctic sea ice concentrations. We examine the changes in sub-seasonal variability for both lower-level North Pacific zonal winds and North American surface temperatures between the two experiments, and identify changes caused by Arctic sea ice loss. While the changes in January-February mean North Pacific U700 are small across all of the models (on the order of 2 ms^{-1}, Fig. 4.1), they are still considered significant at a 99% confidence level. The large number of ensemble members for each experiment is what allows us to distinguish a forced response from the internal noise of the system. Further, the strong

model agreement in the mean U700 change adds to our confidence that the changes we are seeing, specifically a strengthened and extended North Pacific eddy-driven jet stream with negative wind anomalies along the poleward flank, are truly forced by the Arctic sea ice loss. Similar to the small mean changes, the changes in frequency of various sub-seasonal U700 variability patterns over the North Pacific are also generally small. Those we have considered significant at 80% confidence in individual models range from differences of only 0.8% - 3.88% of all days. However, by comparing these frequency changes across the four models, all of which show very similar patterns of internal variability (see Figures B.1-B.8 in Appendix B), we gain more confidence that some of the frequency changes, albeit small, are forced by Arctic sea ice loss:

- Super Strengthen: all four models show an increased frequency, and three of the models exhibit significance with at least 80% confidence.
- Poleward Tilt: all four models show an increased frequency, and two of the models exhibit significance of 90% confidence.
- Weaken/Retract: three of four models show a decreased frequency, two of which are significant at 90% confidence.
- Equatorward Shift: all four models show a decreased frequency, and all are significant at 90% confidence.

While we consider the changes in frequency of the above North Pacific U700 anomaly patterns to be directly forced by Arctic sea ice loss in these PAMIP experiments, it is important to consider the limitations of applying these findings to the observations. Not only are there fewer than 3000 Janaury-February days in the observational record (compared to the 5900 or even 9000 days in these experiments), there is also low-frequency variability not included here, such as ENSO, as well as atmosphere-ocean coupling. Further, the observed sea ice loss has inter-annual temporal variability, whereas these experiments are run forcing that only varies as a function of season. With that said, these experiments provide examples of what we may expect as consequences of Arctic sea ice loss, and these conclusions are strengthened by the consistency between models.

Arctic sea ice loss also leads to changes in North American surface temperature sub-seasonal variability. Again, using significance thresholds for individual models and comparing those to

the multi-model agreement increases our confidence that some of the changes we see are indeed forced by Arctic sea ice loss. Specifically, in the PAMIP futArcSIC experiment we see an increase in the number of days with anomalously warm temperatures to the west and cold temperatures to the east, i.e. the North American temperature dipole, and a decreased number of days with anomalous cold air outbreaks over much of North America. Both of these changes are consistent with the upstream changes in the North Pacific, as previously shown in Griffin and Martin (2017), supporting the theory that, since North American weather regimes depend, in part, on atmospheric activity over the North Pacific (e.g. Jaffe et al. 2011; Griffin and Martin 2017; Swain et al. 2017; Chien et al. 2019), Arctic sea ice loss can indirectly affect North American weather via changes in the North Pacific circulation patterns (e.g. Lee et al. 2015). While the forced response of the atmosphere to Arctic sea ice loss in the atmosphere-only time-slice PAMIP experiments is very small, particularly compared to the internal variability of the system, the large number of ensemble members allowed us to identify some robust responses. However, this set of experiments is not designed to aid in identifying underlying physical processes associated with the response seen (Smith et al. 2019). Thus, we are unable to comment on the mechanism(s) which may cause the North Pacific jet to strengthen in response to Arctic sea ice loss. A future subset of PAMIP experiments are planned, in particular the coupled ocean-atmosphere extended experiments, which may provide some insight (see Table 1 in Smith et al. 2019). Of particular interest are the possible changes in North Pacific wavebreaking associated with the sea ice loss, which previous work has linked to a strengthened jet (Ronalds and Barnes 2019).

The authors thank Rosie Eade at the UK Meteorological Office, Lantao Sun at Colorado State University, Michael Sigmond at the Canadian Centre for Climate Modelling and Analysis and Yannick Peings at UC Irvine for the use of the HadGEM3, CESM2, CanESM5 and SC-WACCM data, respectively. The authors are supported by the Climate and Large-scale Dynamics Program of the National Science Foundation under Grant AGS-1545675, and EAB is also supported under Grant AGS-1749261.

5 Conclusions

The work shown here focuses on the response of the Northern Hemisphere mid-latitude eddy-driven jet streams to the amplified Arctic warming and substantial sea ice loss resulting from climate change. Both the wintertime mean changes as well as the sub-seasonal, wintertime changes in variability are explored across a suite of modeling experiments, ranging from idealized atmospheric models to fully coupled climate models. While the focus is primarily on the behaviour of the eddy-driven jet streams over both the North Atlantic and the North Pacific ocean basins, the sub-seasonal variability of wintertime surface temperatures over North America is also discussed. The large-scale circulation responses to Arctic warming and sea ice loss are small, they are considered robust. The underlying dynamics responsible for these responses have been explored in depth in this work, bringing a new understanding to the research community.

5.1 CONSISTENCY AND DISCREPANCY OF THE JET STREAM RESPONSES

Throughout this dissertation we compare and contrast the wintertime eddy-driven jet stream response in the North Atlantic and North Pacific. Specifically, the North Atlantic jet weakens, narrows significantly on the poleward flank, and shifts equatorward slightly, whereas the North Pacific jet strengthens, narrows, and does not shift in latitude. While the jet speed and latitude responses clearly differ, in both cases the jet narrows in response to Arctic sea ice loss. This narrowing occurs primarily on the poleward flank of the jet, where the sea ice loss has weakened the local surface temperature gradients, leading to enhanced low-level easterlies or weakened westerlies, in keeping with thermal wind balance. While previous studies have attributed the total Northern Hemisphere jet stream response to this mechanism, citing the thermal wind balance associated with a weakened equator-to-pole temperature gradient (e.g. Francis and Vavrus 2012; Peings and Magnusdottir 2014; Barnes and Screen 2015; Deser et al. 2016), this work shows that this mechanism is strongest local to the sea ice loss. The resulting change in low-level winds along the poleward flank of the Northern Hemisphere jet streams is one of the few robust circulation responses to Arctic sea ice loss across a variety of modeling experiments (e.g. Strong and Magnusdottir 2010; Ronalds et al.

2018; Screen et al. 2018b; Ronalds and Barnes 2019).

The differences between the North Atlantic and North Pacific eddy-driven jet stream responses to Arctic sea ice loss emphasize the issue of regionality when discussing impacts. Additionally, the differences suggest that there are multiple mechanisms which control the remote circulation response to Arctic warming and sea ice loss, and that the weakened equator-to-pole temperature gradient is not necessarily dominant. By using the local, high-latitude wind response as the direct impact of sea ice loss, we show that the indirect circulation responses in both basins can be partly explained by changes in the locations and frequency of wave breaking. That is, the Arctic sea ice loss alters local surface temperature gradients, thus altering the low-level winds locally, which in turn changes the atmospheric wave breaking, which impacts the remote circulation, including the eddy-driven jets.

5.2 THE ROLE OF ATMOSPHERIC WAVE BREAKING

The majority of the work and conclusions drawn throughout this dissertation focus on the role of wave breaking in the wintertime eddy-driven jet stream response to Arctic sea ice loss. Both the mean jet response, as well as the changes to jet variability are discussed from this viewpoint. We find that the sea ice loss directly drives anomalous easterlies at high latitudes in a fully couple climate model. This direct effect is used within a suite of idealized modeling experiments in order to explore the eddy response to the direct sea ice loss forcing. The high latitude anomalous easterlies narrow the jet along the poleward flank, limiting the poleward extent that waves can travel before being forced to break or reflect (Ronalds et al. 2018; Ronalds and Barnes 2019). In the North Atlantic, where the climatological, wintertime jet is further north than in the North Pacific, this narrowing of the jet is substantial, and leads to a decrease in the variability of the monthly jet latitude, as well as reduced wind speeds in within the jet itself. In the North Pacific, the jet is too far south for the anomalous easterlies to directly impact the jet, and the narrowing is not as notable as in the North Atlantic.

The differences in how the jets respond in both basins, along with the differences in the role of wave breaking in that response, are investigated in an idealized modeling framework. We find

that changes in wave breaking in response to anomalous easterlies at high latitudes are similar in both basins, and that the differences stem from the differing jet latitudes relative to the forcing location. In both cases, the eddies respond to the forcing by altering wave breaking locations and frequencies, attempting to increase the jet speed in both cases. The sensitivity of the jet stream's net response to the sea ice loss forcing to the climatological jet latitude is substantial, and thus eliminating model biases in jet latitude is of utmost importance moving forward.

5.3 POLAR AMPLIFICATION MODEL INTERCOMPARISON PROJECT

The ongoing Polar Amplification Model Intercomparison Project (PAMIP) allows for the unique opportunity to investigate the forced response of the atmosphere to Arctic sea ice loss across a multitude of models, all with the same experimental design. It is important to note that the work presented within this dissertation represents some of the first results from this modeling project. The first tier of experiments are designed to identify the forced, atmospheric response to changes in Arctic sea ice concentrations and/or sea surface temperatures, and use large ensembles and short timescales to increase the signal-to-noise ratio (Smith et al. 2019). Because of the design, these experiments are not ideal for studying and identifying physical mechanisms, and thus we were unable to relate our previous work on barotropic, wave breaking mechanisms to the forced, low-level wind responses seen in PAMIP. However, many of the results remain consistent with our previous findings, further emphasizing that the responses are robust and deserve further study.

Consistent with our previous results, the four climate models' PAMIP future Arctic sea ice runs show a strengthened wintertime eddy-driven jet stream in the North Pacific, relative to the pre-industrial Arctic sea ice runs. When this mean response is decomposed into sub-seasonal variability changes we find an increase in strengthened and extended jet events, and a decrease in weakened, retracted, and equatorward shifted jet events. These changes are considered robustly forced by the Arctic sea ice loss. Analysis of North American surface temperatures confirmed that variability in North Pacific jet activity is closely linked with downstream, North American temperatures (e.g. Strong and Davis 2008; Jaffe et al. 2011; Lee et al. 2015; Griffin and Martin 2017; Swain et al. 2017; Chien et al. 2019). This relationship implies that changes in the sub-seasonal,

wintertime North Pacific jet stream variability forced by Arctic sea ice loss will lead to changes in sub-seasonal temperature patterns over North America. Specifically, we find an increased frequency of the North American temperature dipole, with anomalous warm temperatures in the west and cold to the east, which is associated with a strengthened and extended North Pacific jet. There is also decreased frequency of cold air outbreaks over North America, which are associated with both an equatorward-shifted and a weakened and retracted North Pacific jet.

5.4 MOVING FORWARD

The work contained within this dissertation has provided physical hypotheses linking Arctic warming and sea ice loss to changes in the midlatitude, large-scale circulation, both in the mean and in terms of variability. It has also highlighted sources of uncertainty that must be addressed within the research community. In particular, biases in the climatological, regional jet stream latitudes within the models can change how the jet responds to sea ice loss. Specifically, we show in Ronalds and Barnes (2019) that the net jet speed response in a simplified model configuration depends heavily on the jet latitude, and that jets further south can strengthen while jets further north weaken. This finding has particular relevance as there is an equatorward bias of the eddy-driven jet positions in climate models (e.g. Barnes and Polvani 2013; Bracegirdle et al. 2013; Pithan et al. 2016). Another source of uncertainty stems from the issue of regionality when exploring the circulation response to Arctic sea ice loss. Focusing on specific regions is of great importance, as this work has highlighted some differences in the North Pacific and North Atlantic jet stream responses. Future research should be aware that by taking a zonal mean approach, particularly in the Northern Hemisphere, the results may be skewed towards a certain region, or the responses may even cancel out.

One of the main components in physically understanding the atmospheric response to climate change is attributing forced circulation responses to a specific forcing via individual physical mechanisms. As the PAMIP experiments continue to become available, there is increased opportunity to investigate specific, physical mechanisms underlying the atmospheric circulation response to Arctic sea ice loss across climate models. While idealized modeling experiments, including those

in this dissertation, help identify and explain these mechanisms (e.g. Barnes et al. 2010; Strong and Magnusdottir 2010; Hassanzadeh et al. 2014; Hassanzadeh and Kuang 2015; Sellevold et al. 2016; McKenna et al. 2018; Ronalds et al. 2018; Ronalds and Barnes 2019; Ruggieri et al. 2019), linking these idealized experiments to more complex climate models is critical in furthering our understanding of the relative importance and interactions of each mechanism. Further, we can compare the atmospheric circulation responses in the Arctic warming and sea ice loss experiments in PAMIP to the increased greenhouse gas experiments in the Coupled Model Intercomparison Project (CMIP6; Eyring et al. 2016). The direct comparison between experiments, particularly those with nearly identical forcing, will aid in attributing certain responses to either the Arctic or the tropics, where upper-tropospheric warming is the main response to increased greenhouse gasses. The goal with climate modeling experiments is to recognize the combined role and interactions of the physical mechanisms controlling the circulation response to the full climate change forcing. This knowledge can then be applied to the observed circulation changes, something that has proven exceptionally difficult due to the brevity of the observational record and the scale of internal variability (e.g Gu et al. 2018; Cohen et al. 2020).

Historically, the impacts of Arctic warming and sea ice loss versus tropical warming on the large-scale circulation has been referred as a tug-of-war, with Arctic warming leading to a weakened and equatorward-shifted jet, and tropical warming leading to a poleward shifted jet (e.g. Woollings and Blackburn 2012; Barnes and Screen 2015; McGraw and Barnes 2016; Peings 2018; Screen et al. 2018b). Based on the work presented in this dissertation, this tug-of-war concept may not be accurate, particularly in certain regions, such as the North Pacific. Furthermore, if we examine jet width in addition to jet speed and latitude, the response to both Arctic and tropical warming may be the same: a narrowing of the eddy-driven jet streams. We showed that a narrowing of the jet on the poleward flank is a robust response to Arctic sea ice loss in a fully coupled climate model (Ronalds et al. 2018; Ronalds and Barnes 2019), and Peings (2018) showed that a narrowing of the North Atlantic jet is a robust response to the full climate change signal, again in a fully coupled climate model. Thus, in this case, there is no competition between the Arctic and tropics. This suggests that, moving forward, the tug-of-war concept does not accurately describe the large-scale

atmospheric circulation response to climate change. This also shows that regionality is again key in understanding both the circulation response and the consequences of that response to climate change as a whole.

Bibliography

Alvarez, J., D. Yumashev, and G. Whiteman, 2019: A framework for assessing the economic impacts of arctic change. *Ambio*.

Barnes, E. A., 2013: Revisiting the evidence linking Arctic amplification to extreme weather in midlatitudes. *Geophysical Research Letters*, **40**, 4734–4739, doi: 10.1002/grl.50880, arXiv:1011.1669v3.

Barnes, E. A. and D. L. Hartmann, 2011: Rossby Wave Scales, Propagation, and the Variability of Eddy-Driven Jets. *Journal of the Atmospheric Sciences*, **68 (12)**, 2893–2908, doi: 10.1175/JAS-D-11-039.1, URL http://journals.ametsoc.org/doi/abs/10.1175/JAS-D-11-039.1.

Barnes, E. A. and D. L. Hartmann, 2012: Detection of Rossby wave breaking and its response to shifts of the midlatitude jet with climate change. *Journal of Geophysical Research Atmospheres*, **117 (9)**, 1–17, doi: 10.1029/2012JD017469.

Barnes, E. A., D. L. Hartmann, D. M. W. Frierson, and J. Kidston, 2010: Effect of latitude on the persistence of eddy-driven jets. *Geophys. Res. Lett*, **37**, L11 804, doi: 10.1029/2010GL043199.

Barnes, E. A. and L. Polvani, 2013: Response of the midlatitude jets, and of their variability, to increased greenhouse gases in the CMIP5 models. *Journal of Climate*, **26**, 7117–7135, doi: 10.1175/JCLI-D-12-00536.1.

Barnes, E. A. and J. A. Screen, 2015: The impact of Arctic warming on the midlatitude jet-stream: Can it? Has it? Will it? *Wiley Interdisciplinary Reviews: Climate Change*, **6**, 277–286, doi: 10.1002/wcc.337.

Barnes, E. A. and I. R. Simpson, 2017: Seasonal sensitivity of the Northern Hemisphere jet-streams to Arctic temperatures on subseasonal timescales. *Journal of Climate*, JCLI–D–17–0299.1, doi: 10.1175/JCLI-D-17-0299.1, URL http://journals.ametsoc.org/doi/10.1175/JCLI-D-17-0299.1.

Barnes, E. A. and D. W. J. Thompson, 2014: Comparing the Roles of Barotropic versus Baroclinic Feedbacks in the Atmosphere's Response to Mechanical Forcing. *Journal of the Atmospheric Sciences*, **71**, 177–194, doi: 10.1175/JAS-D-13-070.1.

Benedict, J. J., S. Lee, and S. B. Feldstein, 2004: Synoptic View of the North Atlantic Oscillation. *Journal of the Atmospheric Sciences*, **61 (2)**, 121–144, doi: 10.1175/1520-0469(2004)061<0121:SVOTNA>2.0.CO;2.

Bitz, C. M., M. M. Holland, E. C. Hunke, and R. E. Moritz, 2005: Maintenance of the Sea-Ice edge. *J. Clim.*, **18 (15)**, 2903–2921.

Blackmon, M. L., 1976: A Climatological Spectral Study of the 500 mb Geopotential Height of the Northern Hemisphere. *Journal of the Atmospheric Sciences*, **33 (8)**, 1607–1623, doi: 10.1175/1520-0469(1976)033<1607:ACSSOT>2.0.CO;2.

Blackport, R. and J. A. Screen, 2019: Influence of arctic sea ice loss in autumn compared to that in winter on the atmospheric circulation. *Geophys. Res. Lett.*, **46 (4)**, 2213–2221.

Blythe, J., D. Armitage, G. Alonso, D. Campbell, A. C. Esteves Dias, G. Epstein, M. Marschke, and P. Nayak, 2019: Frontiers in coastal well-being and ecosystem services research: A systematic review. *Ocean Coast. Manag.*, 105028.

Bracegirdle, T. J., E. Shuckburgh, J. B. Sallee, Z. Wang, A. J. S. Meijers, N. Bruneau, T. Phillips, and L. J. Wilcox, 2013: Assessment of surface winds over the atlantic, indian, and pacific ocean sectors of the southern ocean in cmip5 models: Historical bias, forcing response, and state dependence. *Journal of Geophysical Research Atmospheres*, **118 (2)**, 547–562, doi: 10.1002/jgrd.50153.

Brayshaw, D. J., B. Hoskins, and M. Blackburn, 2009: The Basic Ingredients of the North Atlantic Storm Track. Part I: Land–Sea Contrast and Orography. *Journal of the Atmospheric Sciences*, **66**, 2539–2558, doi: 10.1175/2009JAS3078.1.

Burrows, D. A. and G. Chen, 2017: Barotropic and Baroclinic Eddy Feedbacks in the Midlatitude Jet Variability and Responses to Climate Change–Like Thermal Forcings. *Journal of the Atmospheric Sciences*, **74**, 111–132, doi: 10.1175/JAS-D-16-0047.1.

Chan, F. T., et al., 2019: Climate change opens new frontiers for marine species in the arctic: Current trends and future invasion risks. *Glob. Chang. Biol.*, **25 (1)**, 25–38.

Chien, Y.-T., S.-Y. S. Wang, Y. Chikamoto, S. L. Voelker, J. D. D. Meyer, and J.-H. Yoon, 2019: North american winter dipole: Observed and simulated changes in circulations. *Atmosphere*, **10 (12)**, 793.

Ciarli, T. and M. Savona, 2019: Modelling the evolution of economic structure and climate change: A review. *Ecol. Econ.*, **158**, 51–64.

Ciavarella, A., et al., 2018: Upgrade of the HadGEM3-A based attribution system to high resolution and a new validation framework for probabilistic event attribution. *Weather and Climate Extremes*, **20**, 9–32.

Cione, J. J., S. Raman, and L. J. Pietrafesa, 1993: The Effect of Gulf Stream-induced Baroclinicity on U.S. East Coast Winter Cyclones. *Monthly Weather Review*, **121**, 421–430.

Cohen, J., K. Pfeiffer, and J. A. Francis, 2018: Warm arctic episodes linked with increased frequency of extreme winter weather in the united states. *Nat. Commun.*, **9 (1)**, 869.

Cohen, J., et al., 2014: Recent arctic amplification and extreme mid-latitude weather. *Nat. Geosci.*, **7**, 627.

Cohen, J., et al., 2020: Divergent consensuses on arctic amplification influence on midlatitude severe winter weather. *Nat. Clim. Chang.*, **10 (1)**, 20–29.

Coumou, D., V. Petoukhov, S. Rahmstorf, S. Petri, and H. J. Schellnhuber, 2014: Quasi-resonant circulation regimes and hemispheric synchronization of extreme weather in boreal summer. *Proc. Natl. Acad. Sci. U. S. A.*, **111 (34)**, 12 331–12 336.

Cvijanovic, I., B. D. Santer, C. Bonfils, D. D. Lucas, J. C. H. Chiang, and S. Zimmerman, 2017: Future loss of arctic sea-ice cover could drive a substantial decrease in california's rainfall. *Nat. Commun.*, **8 (1)**, 1947.

Deser, C., G. Magnusdottir, R. Saravanan, and A. Phillips, 2004: The Effects of North Atlantic SST and Sea Ice Anomalies on the Winter Circulation in CCM3. Part II: Direct and Indirect Components of the Response. *Journal of Climate*, **17**, 877–889.

Deser, C., A. Phillips, V. Bourdette, and H. Teng, 2012: Uncertainty in climate change projections: The role of internal variability. *Climate Dynamics*, **38**, 527–546, doi: 10.1007/s00382-010-0977-x.

Deser, C., L. Sun, R. A. Tomas, and J. Screen, 2016: Does ocean coupling matter for the northern extratropical response to projected Arctic sea ice loss? *Geophysical Research Letters*, **43**, doi: 10.1002/2016GL067792.

Deser, C., R. Tomas, M. Alexander, and D. Lawrence, 2010: The seasonal atmospheric response to projected Arctic sea ice loss in the late twenty-first century. *Journal of Climate*, **23**, 333–351, doi: 10.1175/2009JCLI3053.1.

Deser, C., R. A. Tomas, and S. Peng, 2007: The transient atmospheric circulation response to north atlantic SST and sea ice anomalies. *J. Clim.*, **20 (18)**, 4751–4767.

Deser, C., R. A. Tomas, and L. Sun, 2015: The role of ocean-atmosphere coupling in the zonal-mean atmospheric response to Arctic sea ice loss. *Journal of Climate*, **28**, 2168–2186, doi: 10.1175/JCLI-D-14-00325.1.

Douglas, B. C., 1991: Global sea level rise. *J. Geophys. Res.*, **96 (C4)**, 6981.

Eichelberger, S. J. and D. L. Hartmann, 2007: Zonal jet structure and the leading mode of variability. *Journal of Climate*, **20**, 5149–5163, doi: 10.1175/JCLI4279.1.

Eyring, V., S. Bony, G. A. Meehl, C. A. Senior, B. Stevens, R. J. Stouffer, and K. E. Taylor, 2016: Overview of the coupled model intercomparison project phase 6 (CMIP6) experimental design and organization. *Geoscientific Model Development (Online)*, **9 (LLNL-JRNL-736881)**.

Falardeau, M. and E. M. Bennett, 2019: Towards integrated knowledge of climate change in arctic marine systems: a systematic literature review of multidisciplinary research. *Arctic Science*, 1–22.

Fatorić, S. and E. Seekamp, 2017: Are cultural heritage and resources threatened by climate change? a systematic literature review. *Clim. Change*, **142 (1)**, 227–254.

Fletcher, C. G., P. J. Kushner, A. Hall, and X. Qu, 2009: Circulation responses to snow albedo feedback in climate change. *Geophysical Research Letters*, **36 (9)**, 2–5, doi: 10.1029/2009GL038011.

Francis, J. A. and S. J. Vavrus, 2012: Evidence linking Arctic amplification to extreme weather in mid-latitudes. *Geophysical Research Letters*, **39**, L06 801, doi: 10.1029/2012GL051000, arXiv:1011.1669v3.

Francis, J. A. and S. J. Vavrus, 2015: Evidence for a wavier jet stream in response to rapid Arctic warming. *Environmental Research Letters*, **10 (1)**, 014 005, doi: 10.1088/1748-9326/10/1/014005, URL http://stacks.iop.org/1748-9326/10/i=1/a=014005?key=crossref.74581076f734b2377ec8042d3aebe25d.

Garfinkel, C. I. and D. W. Waugh, 2014: Tropospheric rossby wave breaking and variability of the latitude of the Eddy-Driven jet. *J. Clim.*, **27 (18)**, 7069–7085.

Garfinkel, C. I., D. W. Waugh, and E. P. Gerber, 2013: The effect of tropospheric jet latitude on coupling between the stratospheric polar vortex and the troposphere. *Journal of Climate*, **26**, 2077–2095, doi: 10.1175/JCLI-D-12-00301.1.

Gettelman, A., et al., 2019: High climate sensitivity in the community earth system model version 2 (CESM2). *Geophys. Res. Lett.*, **46 (14)**, 8329–8337.

Graversen, R. G. and M. Wang, 2009: Polar amplification in a coupled climate model with locked albedo. *Climate Dynamics*, **33 (5)**, 629–643, doi: 10.1007/s00382-009-0535-6.

Griffin, K. S. and J. E. Martin, 2017: Synoptic features associated with temporally coherent modes of variability of the north pacific jet stream. *J. Clim.*, **30 (1)**, 39–54.

Gruda, N., M. Bisbis, and J. Tanny, 2019: Influence of climate change on protected cultivation: Impacts and sustainable adaptation strategies - a review. *J. Clean. Prod.*, **225**, 481–495.

Gu, S., Y. Zhang, Q. Wu, and X.-Q. Yang, 2018: The linkage between arctic sea ice and midlatitude weather: In the perspective of energy. *J. Geophys. Res. D: Atmos.*, **123 (20)**, 11,536–11,550.

Hansen, J., M. Sato, R. Ruedy, K. Lo, D. W. Lea, and M. Medina-Elizade, 2006: Global temperature change. *Proc. Natl. Acad. Sci. U. S. A.*, **103 (39)**, 14 288–14 293.

Hartigan, J. A. and M. A. Wong, 1979: Algorithm AS 136: A K-Means clustering algorithm. *J. R. Stat. Soc. Ser. C Appl. Stat.*, **28 (1)**, 100–108.

Hartmann, D. L., 2007: The Atmospheric General Circulation and Its Variability. *Journal of the Meteorological Society of Japan*, **85B**, 123–143, doi: 10.2151/jmsj.85B.123.

Hassanzadeh, P. and Z. Kuang, 2015: Blocking variability: Arctic Amplification versus Arctic Oscillation. *Geophysical Research Letters*, **42 (20)**, 8586–8595, doi: 10.1002/2015GL065923.

Hassanzadeh, P. and Z. Kuang, 2016: The Linear Response Function of an Idealized Atmosphere. Part I: Construction Using Green's Functions and Applications. *Journal of the Atmospheric Sciences*, **73 (9)**, 3423–3439, doi: 10.1175/JAS-D-15-0338.1, URL `http://journals.ametsoc.org/doi/10.1175/JAS-D-15-0338.1`, `1511.02214`.

Hassanzadeh, P., Z. Kuang, and B. F. Farrell, 2014: Responses of midlatitude blocks and wave amplitude to changes in the meridional temperature gradient in an idealized dry GCM. *Geophysical Research Letters*, **41 (14)**, 5223–5232, doi: 10.1002/2014GL060764.

Held, I. M., 1993: Large-Scale Dynamics and Global Warming. *Bulletin American Meteorological Society*, **74 (2)**, 228–241.

Held, I. M. and M. J. Suarez, 1994: A Proposal for the Intercomparison of the Dynamical Cores of Atmospheric General Circulation Models. *Bulletin of the American Meteorological Society*, **75 (10)**, 1825–1830, doi: 10.1175/1520-0477(1994)075<1825:APFTIO>2.0.CO;2.

Holland, M. M. and C. M. Bitz, 2003: Polar amplification of climate change in coupled models. *Climate Dynamics*, **21**, 221–232, doi: 10.1007/s00382-003-0332-6.

Hoskins, B. and T. Woollings, 2015: Persistent extratropical regimes and climate extremes. *Current Climate Change Reports*, **1 (3)**, 115–124.

Hoskins, B. J. and T. Ambrizzi, 1993: Rossby Wave Propagation on a Realistic Longitudinally Varying Flow. *Journal of the Atmospheric Sciences*, **50 (12)**, 1661–1671, doi: 10.1175/1520-0469(1993)050<1661:RWPOAR>2.0.CO;2.

Hoskins, B. J. and D. J. Karoly, 1981: The Steady Linear Response of a Spherical Atmosphere to Thermal and Orographic Forcing. *Journal of the Atmospheric Sciences*, **38**, 1179–1196.

Hoskins, B. J. and P. J. Valdes, 1990: On the existence of storm tracks. *Journal of Atmospheric Sciences*, **47**, 1854–1864, doi: 10.1175/ 1520-0469(1990)047,1854:OTEOST.2.0.CO;2.

Iqbal, W., W.-N. Leung, and A. Hannachi, 2018: Analysis of the variability of the north atlantic eddy-driven jet stream in CMIP5. *Clim. Dyn.*, **51 (1)**, 235–247.

Jaffe, S. C., J. E. Martin, D. J. Vimont, and D. J. Lorenz, 2011: A synoptic climatology of episodic, subseasonal retractions of the pacific jet. *J. Clim.*, **24 (11)**, 2846–2860.

Kidston, J. and E. P. Gerber, 2010: Intermodel variability of the poleward shift of the austral jet stream in the CMIP3 integrations linked to biases in 20th century climatology. *Geophysical Research Letters*, **37**, L09 708, doi: 10.1029/2010GL042873.

Kidston, J. and G. K. Vallis, 2010: Relationship between eddy-driven jet latitude and width. *Geophysical Research Letters*, **37**, L21 809, doi: 10.1029/2010GL044849.

Kidston, J. and G. K. Vallis, 2012: The Relationship between the Speed and the Latitude of an Eddy-Driven Jet in a Stirred Barotropic Model. *Journal of the Atmospheric Sciences*, **69**, 3251–3263, doi: 10.1175/JAS-D-11-0300.1.

Kim, B. M., S. W. Son, S. K. Min, J. H. Jeong, S. J. Kim, X. Zhang, T. Shim, and J. H. Yoon, 2014: Weakening of the stratospheric polar vortex by Arctic sea-ice loss. *Nature Communications*, **5**, 1–8, doi: 10.1038/ncomms5646, URL `http://dx.doi.org/10.1038/ncomms5646`.

Kirch, W., B. Menne, and R. Bertollini, 2005: *Extreme Weather Events and Public Health Responses*. Springer, Berlin, Heidelberg.

Klink, K., 1999: Climatological mean and interannual variance of United States surface wind speed, direction and velocity. *International Journal of Climatology*, **19 (5)**, 471–488, doi: 10.1002/(SICI)1097-0088(199904)19:5<471::AID-JOC367>3.0.CO;2-X.

Kretschmer, M., D. Coumou, L. Agel, M. Barlow, E. Tziperman, and J. Cohen, 2018: More-Persistent weak stratospheric polar vortex states linked to cold extremes. *Bull. Am. Meteorol. Soc.*, **99 (1)**, 49–60.

Kretschmer, M., D. Coumou, J. F. Donges, and J. Runge, 2016: Using causal effect networks to analyze different arctic drivers of midlatitude winter circulation. *J. Clim.*, **29 (11)**, 4069–4081.

Kug, J.-S., J.-H. Jeong, Y.-S. Jang, B.-M. Kim, C. K. Folland, S.-K. Min, and S.-W. Son, 2015: Two distinct influences of arctic warming on cold winters over north america and east asia. *Nat. Geosci.*, **8 (10)**, 759–762.

Lee, M., C. Hong, and H. Hsu, 2015: Compounding effects of warm sea surface temperature and reduced sea ice on the extreme circulation over the extratropical north pacific and north america during the 2013–2014 boreal winter. *Geophys. Res. Lett.*, **42 (5)**, 1612–1618.

Li, M. and D. Luo, 2019: Winter arctic warming and its linkage with midlatitude atmospheric circulation and associated cold extremes: The key role of meridional potential vorticity gradient. *Sci. China Earth Sci.*, **62 (9)**, 1329–1339.

Liu, J., J. a. Curry, H. Wang, M. Song, and R. M. Horton, 2012: Impact of declining Arctic sea ice on win- ter snowfall. *Proceedings of the National Academy of Sciences*, **109 (11)**, 4074–4079, doi: 10.1073/pnas.1114910109.

Lorenz, D. J., 2014a: Understanding Midlatitude Jet Variability and Change Using Rossby Wave Chromatography: Poleward-Shifted Jets in Response to External Forcing. *Journal of the Atmospheric Sciences*, **71**, 2370–2389, doi: 10.1175/JAS-D-13-0200.1.

Lorenz, D. J., 2014b: Understanding Midlatitude Jet Variability and Change Using Rossby Wave Chromatography: Wave–Mean Flow Interaction. *Journal of the Atmospheric Sciences*, **71**, 3684–3705, doi: 10.1175/JAS-D-13-0201.1.

Lorenz, D. J., 2015: Understanding Midlatitude Jet Variability and Change Using Rossby Wave Chromatography: Methodology. *Journal of the Atmospheric Sciences*, **72**, 369–388, doi: 10.1175/JAS-D-13-0199.1.

Lubchenco, J. and T. R. Karl, 2012: Predicting and managing extreme weather events. *Phys. Today*, **65 (3)**, 31.

Magnusdottir, G., C. Deser, and R. Saravanan, 2004: The Effects of North Atlantic SST and Sea Ice Anomalies on the Winter Circulation in CCM3. Part I: Main Features and Storm Track Characteristics of the Response. *Journal of Climate*, **17 (5)**, 857–876.

Manney, G. L. and M. I. Hegglin, 2018: Seasonal and regional variations of Long-Term changes in Upper-Tropospheric jets from reanalyses. *J. Clim.*, **31 (1)**, 423–448.

May, J. C. and M. A. Bourassa, 2011: Quantifying variance due to temporal and spatial difference between ship and satellite winds. *Journal of Geophysical Research: Oceans*, **116 (8)**, doi: 10.1029/2010JC006931.

McGraw, M. C. and E. A. Barnes, 2016: Seasonal sensitivity of the eddy-driven jet to tropospheric heating in an idealized AGCM. *Journal of Climate*, **29**, 5223–5240, doi: 10.1175/JCLI-D-15-0723.1.

McKenna, C. M., T. J. Bracegirdle, E. F. Shuckburgh, P. H. Haynes, and M. M. Joshi, 2018: Arctic sea ice loss in different regions leads to contrasting northern hemisphere impacts. *Geophys. Res. Lett.*, **45 (2)**, 945–954.

Meier, W. N., et al., 2014: Arctic sea ice in transformation: A review of recent observed changes and impacts on biology and human activity. *Rev. Geophys.*, **52 (3)**, 185–217.

New, M., D. Liverman, H. Schroeder, and K. Anderson, 2011: Four degrees and beyond: the potential for a global temperature increase of four degrees and its implications. *Philos. Trans. A Math. Phys. Eng. Sci.*, **369 (1934)**, 6–19.

Nordhaus, W., 2019: Climate change: The ultimate challenge for economics. *Am. Econ. Rev.*, **109 (6)**, 1991–2014.

Overland, J., J. A. Francis, R. Hall, E. Hanna, S. J. Kim, and T. Vihma, 2015: The melting arctic and midlatitude weather patterns: Are they connected? *Journal of Climate*, **28 (20)**, 7917–7932, doi: 10.1175/JCLI-D-14-00822.1.

Overland, J. E. and M. Wang, 2018a: Arctic-midlatitude weather linkages in north america. *Polar Sci.*, **16**, 1–9.

Overland, J. E. and M. Wang, 2018b: Resolving future Arctic/Midlatitude weather connections. *Earth's Future*, **6 (8)**, 1146–1152.

Palomo, I., 2017: Climate change impacts on ecosystem services in high mountain areas: A literature review. *Mt. Res. Dev.*, **37 (2)**, 179–187.

Peings, Y., 2018: The atmospheric response to sea-ice loss. *Nat. Clim. Chang.*, **8 (8)**, 664–665.

Peings, Y., J. Cattiaux, S. Vavrus, G. Magnusdottir, and Y. Peings, 2017: Late 21 st Century Changes in the Mid-latitude Atmospheric Circulation in the CESM Large Ensemble. *Journal of Climate*, doi: 10.1175/JCLI-D-16-0340.1.

Peings, Y., J. Cattiaux, S. J. Vavrus, and G. Magnusdottir, 2018: Projected squeezing of the wintertime North-Atlantic jet. *Environ. Res. Lett.*, **13 (7)**, 074 016.

Peings, Y. and G. Magnusdottir, 2014: Response of the wintertime northern hemisphere atmospheric circulation to current and projected arctic sea ice decline: A numerical study with CAM5. *Journal of Climate*, **27 (1)**, 244–264, doi: 10.1175/JCLI-D-13-00272.1.

Petoukhov, V. and V. A. Semenov, 2010: A link between reduced Barents-Kara sea ice and cold winter extremes over northern continents. *Journal of Geophysical Research Atmospheres*, **115 (21)**, 1–11, doi: 10.1029/2009JD013568.

Petrie, R. E., L. C. Shaffrey, and R. T. Sutton, 2015: Atmospheric impact of arctic sea ice loss in a coupled ocean-atmosphere simulation. *Journal of Climate*, **28 (24)**, 9606–9622, doi: 10.1175/JCLI-D-15-0316.1.

Petrov, A. N., et al., 2017: *Arctic sustainability research: past, present and future*. Routledge.

Pithan, F., T. G. Shepherd, G. Zappa, and I. Sandu, 2016: Climate model biases in jet streams, blocking and storm tracks resulting from missing orographic drag: MISSING DRAG CAUSES MODEL BIASES. *Geophys. Res. Lett.*, **43 (13)**, 7231–7240.

Randel, W. J. and I. M. Held, 1991: Phase Speed Spectra of Transient Eddy Fluxes and Critical Layer Absoption. *Journal of the Atmospheric Sciences*, **48 (5)**, 688–697.

Raza, A., A. Razzaq, S. S. Mehmood, X. Zou, X. Zhang, Y. Lv, and J. Xu, 2019: Impact of climate change on crops adaptation and strategies to tackle its outcome: A review. *Plants*, **8 (2)**.

Ring, M. J. and R. A. Plumb, 2007: Forced Annular Mode Patterns in a Simple Atmospheric General Circulation Model. *Journal of the Atmospheric Sciences*, **64**, 3611–3626, doi: 10.1175/JAS4031.1.

Ring, M. J. and R. A. Plumb, 2008: The Response of a Simplified GCM to Axisymmetric Forcings: Applicability of the Fluctuation–Dissipation Theorem. *Journal of the Atmospheric Sciences*, **65 (12)**, 3880–3898, doi: 10.1175/2008JAS2773.1, URL http://journals.ametsoc.org/doi/abs/10.1175/2008JAS2773.1.

Robinson, W. a., 2006: On the Self-Maintenance of Midlatitude Jets. *Journal of the Atmospheric Sciences*, **63 (8)**, 2109–2122, doi: 10.1175/JAS3732.1.

Ronalds, B., E. Barnes, and P. Hassanzadeh, 2018: A barotropic mechanism for the response of jet stream variability to arctic amplification and sea ice loss. *J. Clim.*, **31 (17)**, 7069–7085.

Ronalds, B. and E. A. Barnes, 2019: A role for barotropic Eddy–Mean flow feedbacks in the zonal wind response to sea ice loss and arctic amplification. *J. Clim.*

Ruggieri, P., F. Kucharski, and L. Novak, 2019: The response of the midlatitude jet to regional polar heating in a simple storm track model. *J. Clim.*

Samarasinghe, S. M., M. C. McGraw, E. A. Barnes, and I. Ebert-Uphoff, 2018: A study of links between the arctic and the midlatitude jet stream using granger and pearl causality. *Environmetrics*, **40**, e2540.

Schubert, S., H. Wang, and M. Suarez, 2011: Warm season subseasonal variability and climate extremes in the northern hemisphere: The role of stationary rossby waves. *J. Clim.*, **24 (18)**, 4773–4792.

Screen, J. A., 2014: Arctic amplification decreases temperature variance in northern mid- to high-latitudes. *Nature Climate Change*, **4 (7)**, 577–582, doi: 10.1038/nclimate2268, URL http://www.nature.com/doifinder/10.1038/nclimate2268.

Screen, J. A., T. J. Bracegirdle, and I. Simmonds, 2018a: Polar climate change as manifest in atmospheric circulation. *Current Climate Change Reports*.

Screen, J. A. and I. Simmonds, 2010: The central role of diminishing sea ice in recent Arctic temperature amplification. *Nature*, **464 (7293)**, 1334–1337, doi: 10.1038/nature09051.

Screen, J. A. and I. Simmonds, 2013: Exploring links between Arctic amplification and mid-latitude weather. *Geophysical Research Letters*, **40 (5)**, 959–964, doi: 10.1002/grl.50174.

Screen, J. A., I. Simmonds, C. Deser, and R. Tomas, 2013: The atmospheric response to three decades of observed arctic sea ice loss. *Journal of Climate*, **26**, 1230–1248, doi: 10.1175/JCLI-D-12-00063.1.

Screen, J. A., et al., 2018b: Consistency and discrepancy in the atmospheric response to arctic sea-ice loss across climate models. *Nat. Geosci.*, **11 (3)**, 155–163.

Sellevold, R., S. Sobolowski, and C. Li, 2016: Investigating possible Arctic–Midlatitude teleconnections in a linear framework. *J. Clim.*, **29 (20)**, 7329–7343.

Serreze, M. C., 2003: A record minimum arctic sea ice extent and area in 2002. *Geophys. Res. Lett.*, **30 (3)**, 5.

Serreze, M. C. and J. A. Francis, 2006: The arctic amplification debate. *Climatic Change*, **76 (3-4)**, 241–264, doi: 10.1007/s10584-005-9017-y.

Shaw, T. A., et al., 2016: Storm track processes and the opposing influences of climate change. *Nature Geoscience*, **9**, 656–665, doi: 10.1038/NGEO2783.

Shepherd, T. G., 2016: Effects of a warming arctic. *Science*, **353 (6303)**, 989–990.

Simpson, I. R. and L. M. Polvani, 2016: Revisiting the relationship between jet position, forced response, and annular mode variability in the southern midlatitudes. *Geophysical Research Letters*, **43**, 2896–2903, doi: 10.1002/2016GL067989.

Singh, D., D. L. Swain, J. S. Mankin, D. E. Horton, L. N. Thomas, B. Rajaratnam, and N. S. Diffenbaugh, 2016: Recent amplification of the north american winter temperature dipole. *J. Geophys. Res. D: Atmos.*, **121 (17)**, 9911–9928.

Smith, D. M., N. J. Dunstone, A. A. Scaife, E. K. Fiedler, D. Copsey, and S. C. Hardiman, 2017: Atmospheric response to Arctic and Antarctic sea ice: The importance of ocean-atmosphere coupling and the background state. *Journal of Climate*, doi: 10.1175/JCLI-D-16-0564.1.

Smith, D. M., et al., 2019: The polar amplification model intercomparison project (PAMIP) contribution to CMIP6: investigating the causes and consequences of polar amplification. *Geoscientific Model Development*, **12 (3)**, 1139–1164.

Smith, K. L., R. R. Neely, D. R. Marsh, and L. M. Polvani, 2014: The specified chemistry whole atmosphere community climate model (SC-WACCM). *J. Adv. Model. Earth Syst.*, **6 (3)**, 883–901.

Stroeve, J., M. Serreze, S. Drobot, S. Gearheard, M. Holland, J. Maslanik, W. Meier, and T. Scambos, 2008: Arctic sea ice extent plummets in 2007. *Eos Trans. AGU*, **89 (2)**, 13.

Stroeve, J. C., V. Kattsov, A. Barrett, M. Serreze, T. Pavlova, M. Holland, and W. N. Meier, 2012: Trends in arctic sea ice extent from CMIP5, CMIP3 and observations. *Geophys. Res. Lett.*,

39 (16).

Strong, C. and R. E. Davis, 2008: Variability in the position and strength of winter jet stream cores related to northern hemisphere teleconnections. *J. Clim.*, **21 (3)**, 584–592.

Strong, C. and G. Magnusdottir, 2010: The role of rossby wave breaking in shaping the equilibrium atmospheric circulation response to north atlantic boundary forcing. *J. Clim.*, **23 (6)**, 1269–1276.

Sun, L., M. Alexander, and C. Deser, 2018: Evolution of the global coupled climate response to arctic sea ice loss during 1990–2090 and its contribution to climate change. *J. Clim.*, **31 (19)**, 7823–7843.

Sun, L., C. Deser, and R. A. Tomas, 2015: Mechanisms of stratospheric and tropospheric circulation response to projected Arctic sea ice loss. *Journal of Climate*, **28 (19)**, 7824–7845, doi: 10.1175/JCLI-D-15-0169.1.

Swain, D. L., D. Singh, D. E. Horton, J. S. Mankin, T. C. Ballard, and N. S. Diffenbaugh, 2017: Remote linkages to anomalous winter atmospheric ridging over the northeastern pacific: Remote linkages to pacific high pressure. *J. Geophys. Res. D: Atmos.*, **122 (22)**, 12,194–12,209.

Swart, N. C., et al., 2019: The canadian earth system model version 5 (CanESM5.0.3). *Geoscientific Model Development*, **12 (11)**, 4823–4873.

Teng, H. and G. Branstator, 2017: Causes of extreme ridges that induce california droughts. *J. Clim.*, **30 (4)**, 1477–1492.

Thomas, K., et al., 2019: Explaining differential vulnerability to climate change: A social science review. *Wiley Interdiscip. Rev. Clim. Change*, **10 (2)**, e565.

Thompson, R. O. R. Y., 1980: A Prograde Jet Driven by Rossby Waves. *Journal of the Atmospheric Sciences*, **37 (6)**, 1216–1226, doi: 10.1175/1520-0469(1980)037<1216:APJDBR>2.0.CO;2.

Tschakert, P., N. R. Ellis, C. Anderson, A. Kelly, and J. Obeng, 2019: One thousand ways to experience loss: A systematic analysis of climate-related intangible harm from around the world. *Glob. Environ. Change*, **55**, 58–72.

Vallis, G. K., 2017: *Atmospheric and Oceanic Fluid Dynamics*. 2d ed., Cambridge University Press, 964 pp.

Vallis, G. K., E. P. Gerber, P. J. Kushner, and B. A. Cash, 2004: A Mechanism and Simple Dynamical Model of the North Atlantic Oscillation and Annular Modes. *Journal of the Atmospheric Sciences*, **61**, 264–280.

Vermeer, M. and S. Rahmstorf, 2009: Global sea level linked to global temperature. *Proc. Natl. Acad. Sci. U. S. A.*, **106 (51)**, 21 527–21 532.

Vihma, T., 2014: Effects of Arctic Sea Ice Decline on Weather and Climate: A Review. *Surveys in Geophysics*, **35 (5)**, 1175–1214, doi: 10.1007/s10712-014-9284-0.

Vincent, W. F., 2020: Arctic climate change: Local impacts, global consequences, and policy implications. *The Palgrave Handbook of Arctic Policy and Politics*, K. S. Coates and C. Holroyd, Eds., Springer International Publishing, Cham, 507–526.

Walters, D., et al., 2019: The met office unified model global atmosphere 7.0/7.1 and JULES global land 7.0 configurations. *Geoscientific Model Development*, **12 (5)**, 1909–1963.

Wang, S.-Y., L. Hipps, R. R. Gillies, and J.-H. Yoon, 2015a: Probable causes of the abnormal ridge accompanying the 2013–2014 california drought: ENSO precursor and anthropogenic warming footprint. *Geophys. Res. Lett.*, 3220–3226.

Wang, S.-Y. S., W.-R. Huang, and J.-H. Yoon, 2015b: The north american winter 'dipole'and extremes activity: A CMIP5 assessment. *Atmos. Sci. Lett.*, **16 (3)**, 338–345.

Wang, S.-Y. S., J.-H. Yoon, E. Becker, and R. Gillies, 2017: California from drought to deluge. *Nat. Clim. Chang.*, **7 (7)**, 465–468.

Whittleston, D., K. A. McColl, and D. Entekhabi, 2018: Multimodel future projections of wintertime north atlantic and north pacific tropospheric jets: A bayesian analysis. *J. Clim.*, **31 (6)**, 2533–2545.

Wilks, D. S., 2016: "The stippling shows statistically significant grid points": How research results are routinely overstated and overinterpreted, and what to do about it. *Bulletin of the American Meteorological Society*, 2263–2273, doi: 10.1175/BAMS-D-15-00267.1.

Winton, M., 2006: Amplified Arctic climate change: What does surface albedo feedback have to do with it? *Geophysical Research Letters*, **33 (3)**, 1–4, doi: 10.1029/2005GL025244.

Wittman, M. A. H., A. J. Charlton, and L. M. Polvani, 2005: On the meridional structure of annular modes. *Journal of Climate*, **18**, 2119–2122, doi: 10.1175/JCLI3394.1.

Woollings, T. and M. Blackburn, 2012: The north Atlantic jet stream under climate change and its relation to the NAO and EA patterns. *Journal of Climate*, **25**, 886–902, doi: 10.1175/JCLI-D-11-00087.1.

Woollings, T., A. Hannachi, and B. Hoskins, 2010: Variability of the North Atlantic eddy-driven jet stream. *Quarterly Journal of the Royal Meteorological Society*, **136**, 856–868, doi: 10.1002/qj.625.

Woollings, T., B. Hoskins, M. Blackburn, and P. Berrisford, 2008: A New Rossby Wave–Breaking Interpretation of the North Atlantic Oscillation. *Journal of the Atmospheric Sciences*, **65 (2)**, 609–626, doi: 10.1175/2007JAS2347.1, URL `http://journals.ametsoc.org/doi/abs/10.1175/2007JAS2347.1`.

Woollings, T., et al., 2018: Daily to decadal modulation of jet variability. *Journal of Climate*, JCLI–D–17–0286.1, doi: 10.1175/JCLI-D-17-0286.1, URL http://journals.ametsoc.org/doi/10.1175/JCLI-D-17-0286.1.

Wu, Y. and K. L. Smith, 2016: Response of Northern Hemisphere midlatitude circulation to arctic amplification in a simple atmospheric general circulation model. *Journal of Climate*, **29**, 2041–2058, doi: 10.1175/JCLI-D-15-0602.1.

Yoshiike, S. and R. Kawamura, 2009: Influence of wintertime large-scale circulation on the explosively developing cyclones over the western North Pacific and their downstream effects. *Journal of Geophysical Research: Atmospheres*, **114**, 1–15, doi: 10.1029/2009JD011820.

Yuan, C.-Y., C.-H. Hsieh, and D.-T. Su, 2019: Effects of new shipping routes on the operational resilience of container lines: potential impacts of the arctic sea route and the kra canal on the Europe-Far east seaborne trades. *Maritime Economics & Logistics*.

Zappa, G., F. Pithan, and T. G. Shepherd, 2018: Multimodel evidence for an atmospheric circulation response to arctic sea ice loss in the CMIP5 future projections. *Geophys. Res. Lett.*, **45 (2)**, 1011–1019.

Zhang, X., T. Jung, M. Wang, Y. Luo, T. Semmler, and A. Orr, 2018: Preface to the special issue: Towards improving understanding and prediction of arctic change and its linkage with eurasian mid-latitude weather and climate. *Adv. Atmos. Sci.*, **35 (1)**, 1–4.

Appendices

A SUPPLEMENTAL MATERIAL FOR "A BAROTROPIC MECHANISM FOR THE RESPONSE OF JET STREAM VARIABILITY TO ARCTIC AMPLIFICATION AND SEA ICE LOSS"

This appendix contains a supplemental figure for Chapter 2. The figure represents the lower and upper level January-February mean zonal wind response to sea ice loss in the CCSM4 climate model.

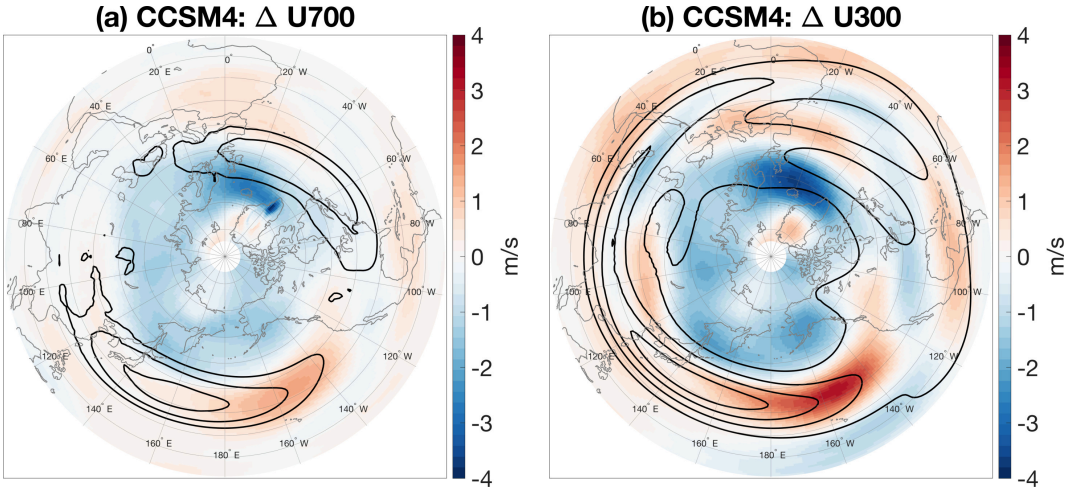

Fig. A.1. The difference in January-February mean zonal winds for *LOWICE-CONTROL* in the CCSM4 sea ice loss experiment. Panel (a) shading represents the difference in winds at 700 hPa, and the contours represent the *CONTROL* mean, with contour intervals of 5 ms^{-1} starting at -10 and 10 ms^{-1}. Panel (b) shading represents the difference in winds at 300 hPa, and the contours represent the *CONTROL* mean, with contour intervals of 15 ms^{-1} starting at -15 and 15 ms^{-1}.

B SUPPLEMENTAL MATERIAL FOR "NORTH PACIFIC ZONAL WIND RESPONSE TO SEA ICE LOSS IN THE POLAR AMPLIFICATION MODEL INTERCOMPARISON PROJECT AND ITS DOWNSTREAM IMPLICATIONS"

This appendix contains the model information and supplemental figures for Chapter 4. The figures consist of inter-model comparisons of the k-means cluster results, which have been organized by similar patterns for ease of comparison. The figures are as follows: the North Pacific daily anomalous zonal winds at 700 hPa centroids (Figures B.1-B.2), the difference in North Pacific zonal wind composite maps (Figures B.3-B.4), the North American daily anomalous surface temperature composites from the pre-industrial Arctic sea ice runs (Figures B.5-B.6), and the k-means cluster centroids of the North American daily anomalous surface temperatures (Figures B.7-B.8). AS noted in Chapter 4, all variables presented here are January-February daily fields smoothed with a 10-day, low-pass Lanczos filter. All four models used in this study (CESM2, CanESM5, HadGEM3 and SC-WACCM) provided daily zonal winds at 700 hPa, and three (CESM2, CanESM5, and HadGEM3) provided daily surface temperatures.

The results from the zonal wind k-means cluster analysis are grouped into six patterns: Super Strengthen, Strengthen/Extend, Poleward Tilt, Weaken/Retract, Equatorward Shift, and Poleward Shift. The first three patterns all represent a strengthened jet core and are grouped together in Figures B.1, B.3, and B.5. The last three patterns all represent a weakened and/or shifted jet, and are grouped together in Figures B.2, B.4, and B.6. Similarly, for the surface temperature k-means cluster analysis, the resulting centroids are again grouped into six patterns: Warm W/Cold E, Warm Air Outbreak, Warm NW/Cold SE, Cold NW/Warm SE, Cold Air Outbreak and Warm East. The first three patterns closely resemble the surface temperature composites shown in Figure B.5 and the last three patterns closely resemble those shown in Figure B.6. Thus, we keep the grouping into two figures consistent for Figures B.7-B.8 in comparison to Figures B.5-B.6.

Table B.1. Model information. Horizontal resolution given in degrees longitude by latitude. Vertical resolution includes the number of vertical levels and the model top.

Model Name	Institution	Horiz. Resolution	Vert. Resolution	Acknowledgements
CESM2	National Center for Atmospheric Research	0.9^o x 1.25^o	33 levels (2 hPa)	Lantao Sun
CanESM5	Canadian Centre for Climate Modelling and Analysis	2.8^o x 2.8^o	49 levels (1 hPa)	Michael Sigmond
HadGEM3	MetOffice UK Hadley Centre	0.8^o x 0.5^o	85 levels (85 km)	Rosie Eade
SC-WACCM	National Center for Atmospheric Research	2.5^o x 1.9^o	66 levels (140 km)	Yannick Peings

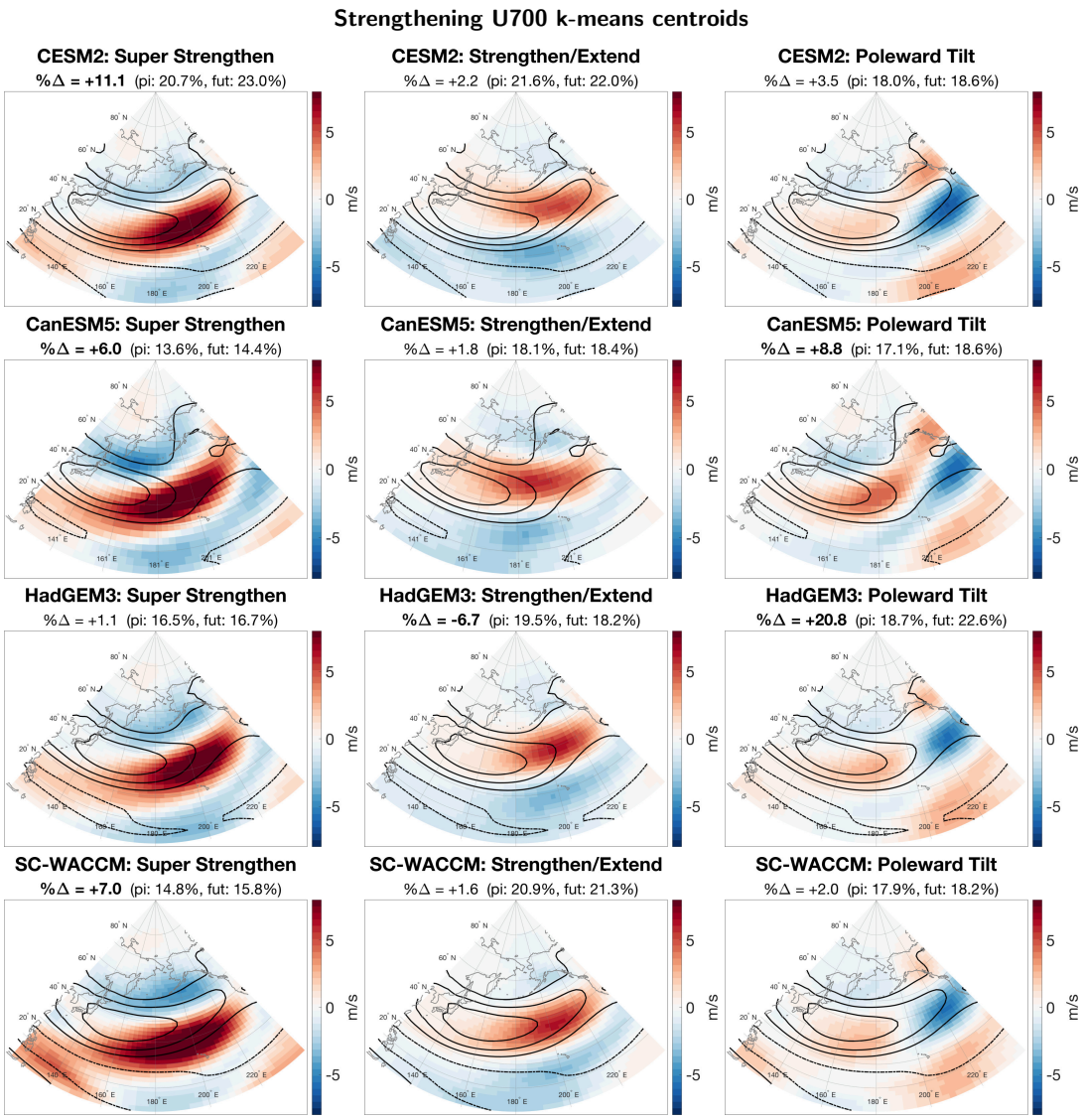

Fig. B.1. The January-February daily anomalous U700 centroids from all four models (shading; CESM2, CanESM5, HadGEM3 and SC-WACCM in rows 1-4, respectively) representing patterns with a strengthened jet: Super Strengthen, Strengthen/Extend, and Poleward Tilt (columns 1-3, respectively). Contours represent the piArcSIC January-February mean U700, and bold face on the %Δ represents significance at 80% confidence.

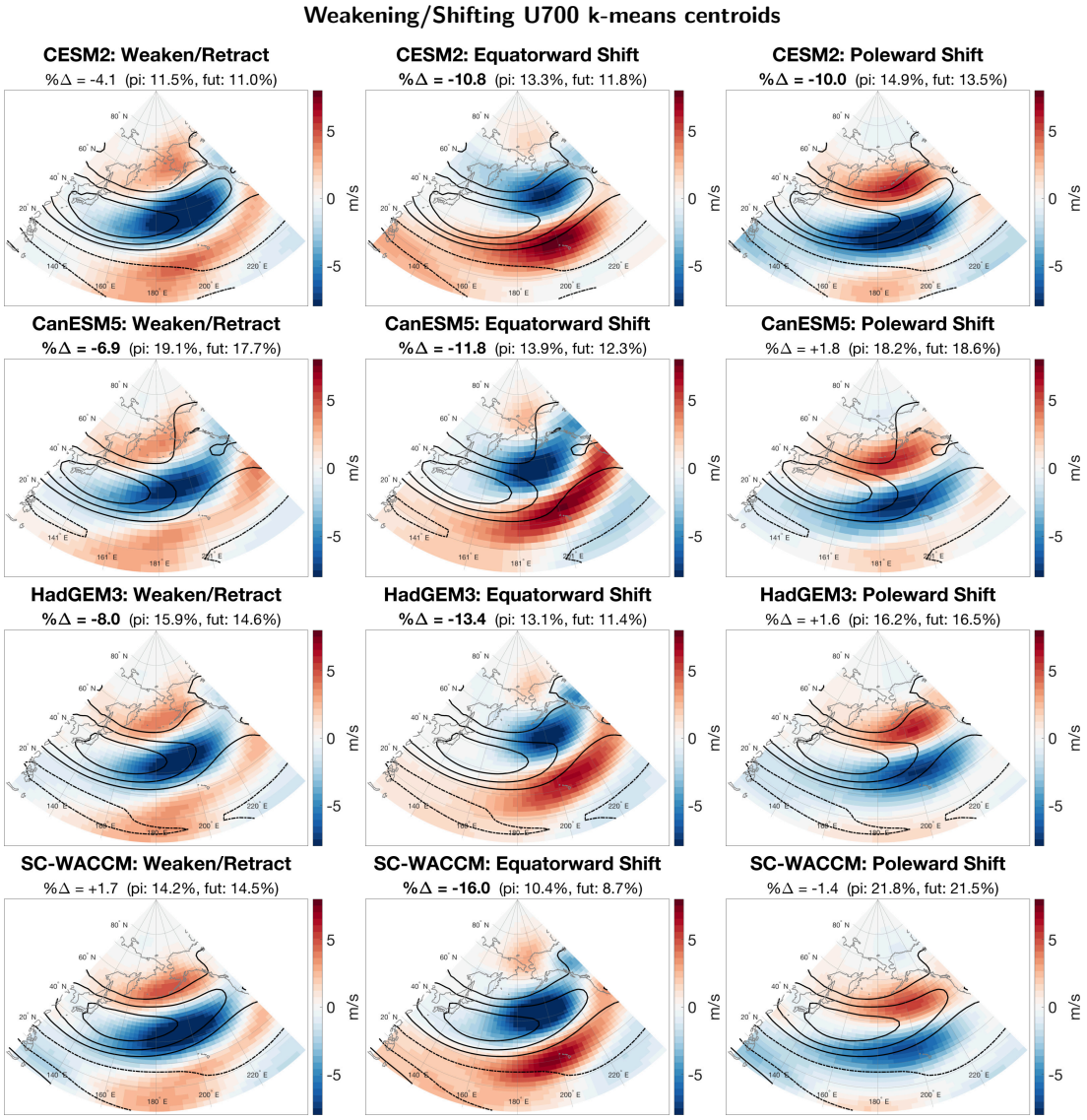

Fig. B.2. The January-February daily anomalous U700 centroids from all four models (shading; CESM2, CanESM5, HadGEM3 and SC-WACCM in rows 1-4, respectively) representing patterns with a weakened or shifted jet: Weaken/Retract, Equatorward Shift, and Poleward Shift (columns 1-3, respectively). Contours represent the piArcSIC January-February mean U700, and bold face on the %Δ represents significance at 80% confidence.

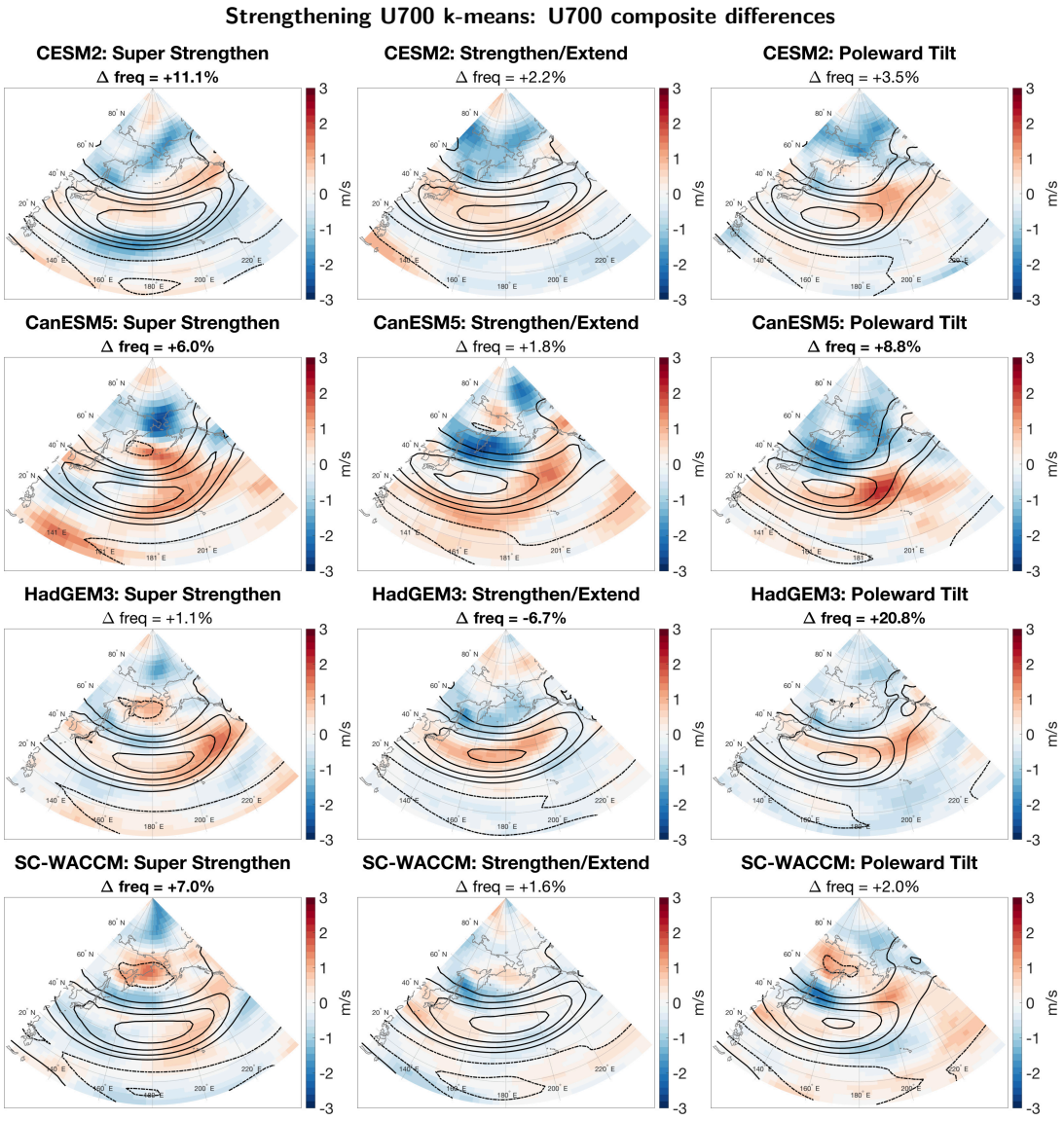

Fig. B.3. Difference between futArcSIC and piArcSIC full field U700 composite maps (shading), based on the daily anomalous strengthened jet U700 variability patterns for all four models (rows). Each column again represents the patterns with a strengthened jet: Super Strengthen, Strengthen/Extend, and Poleward Tilt. Contours represent the piArcSIC daily U700 composite maps, and bold face on the Δfreq represents significance at 80% confidence.

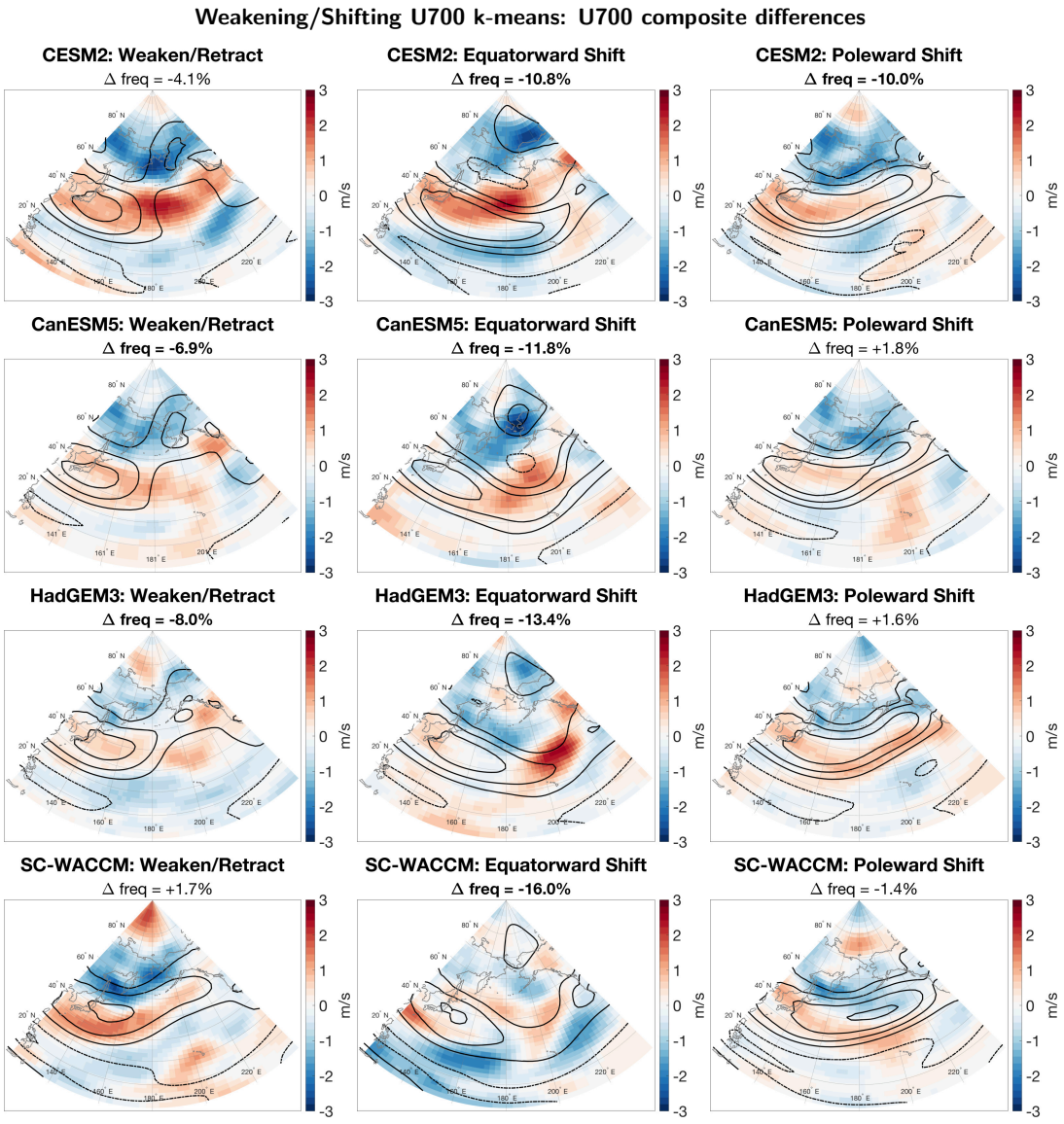

Fig. B.4. Difference between futArcSIC and piArcSIC full field U700 composite maps (shading), based on the daily anomalous weakened and shifted jet U700 variability patterns for all four models (rows). Each column again represents the patterns with a weakened or shifted jet: Weaken/Retract, Equatorward Shift, and Poleward Shift. Contours represent the piArcSIC daily U700 composite maps, and bold face on the Δfreq represents significance at 80% confidence.

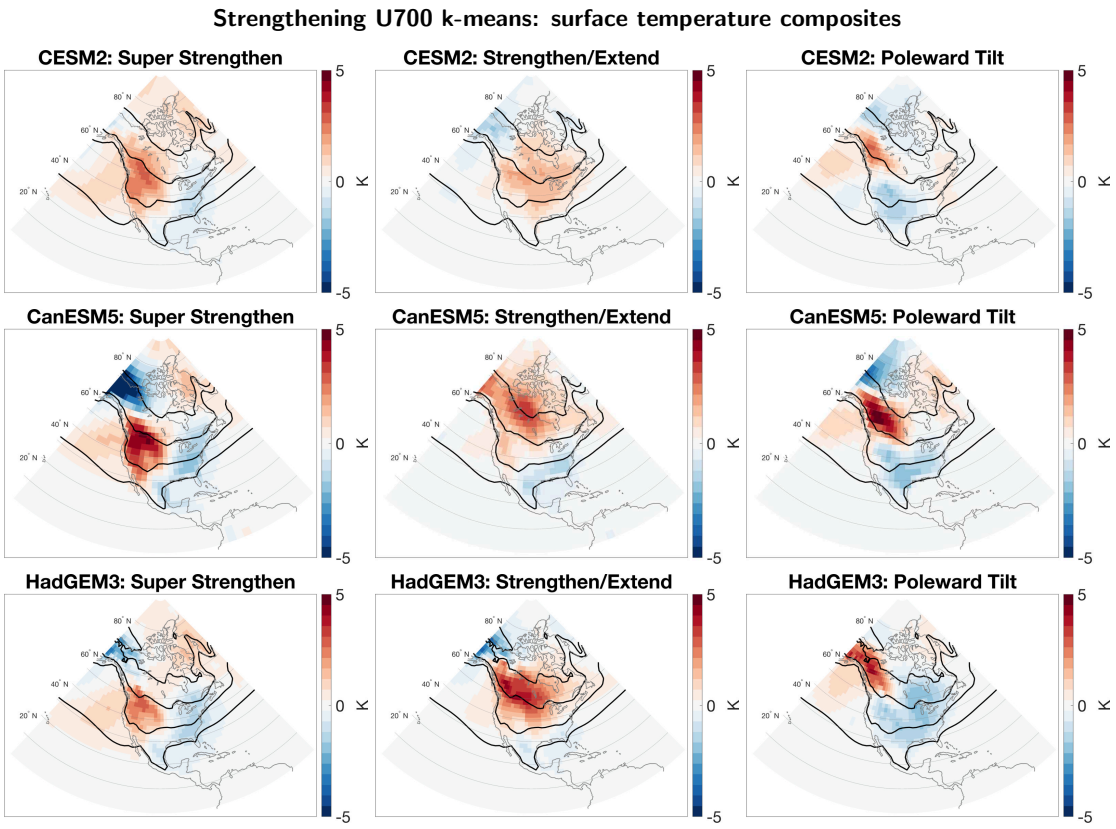

Fig. B.5. Composite maps of daily anomalous North American T_s from the piArcSIC experiment (shading), based on the daily anomalous strengthened jet U700 variability patterns for all four models (rows). Each column again represents the patterns with a strengthened jet: Super Strengthen, Strengthen/Extend, and Poleward Tilt. Contours represent the piArcSIC January-February mean surface temperatures.

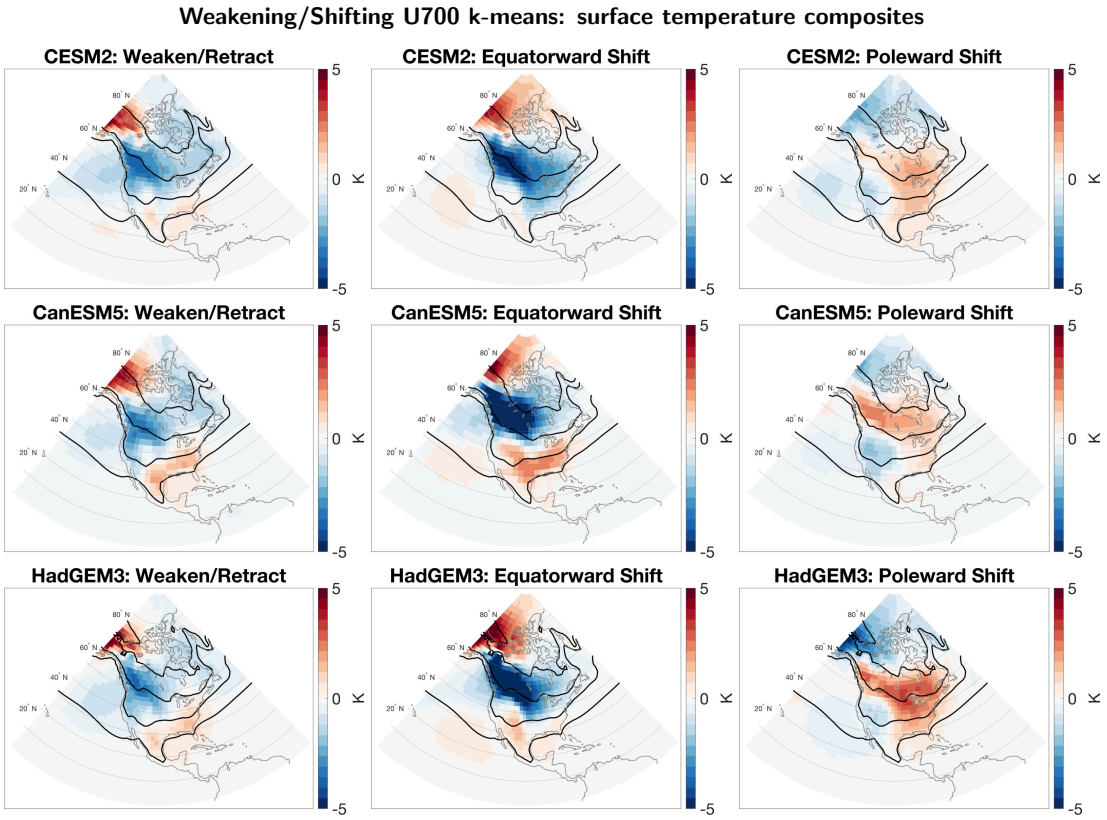

Fig. B.6. Composite maps of daily anomalous North American T_s from the piArcSIC experiment (shading), based on the daily anomalous weakened and shifted jet U700 variability patterns for all four models (rows). Each column again represents the patterns with a weakened or shifted jet: Weaken/Retract, Equatorward Shift, and Poleward Shift. Contours represent the piArcSIC January-February mean surface temperatures.

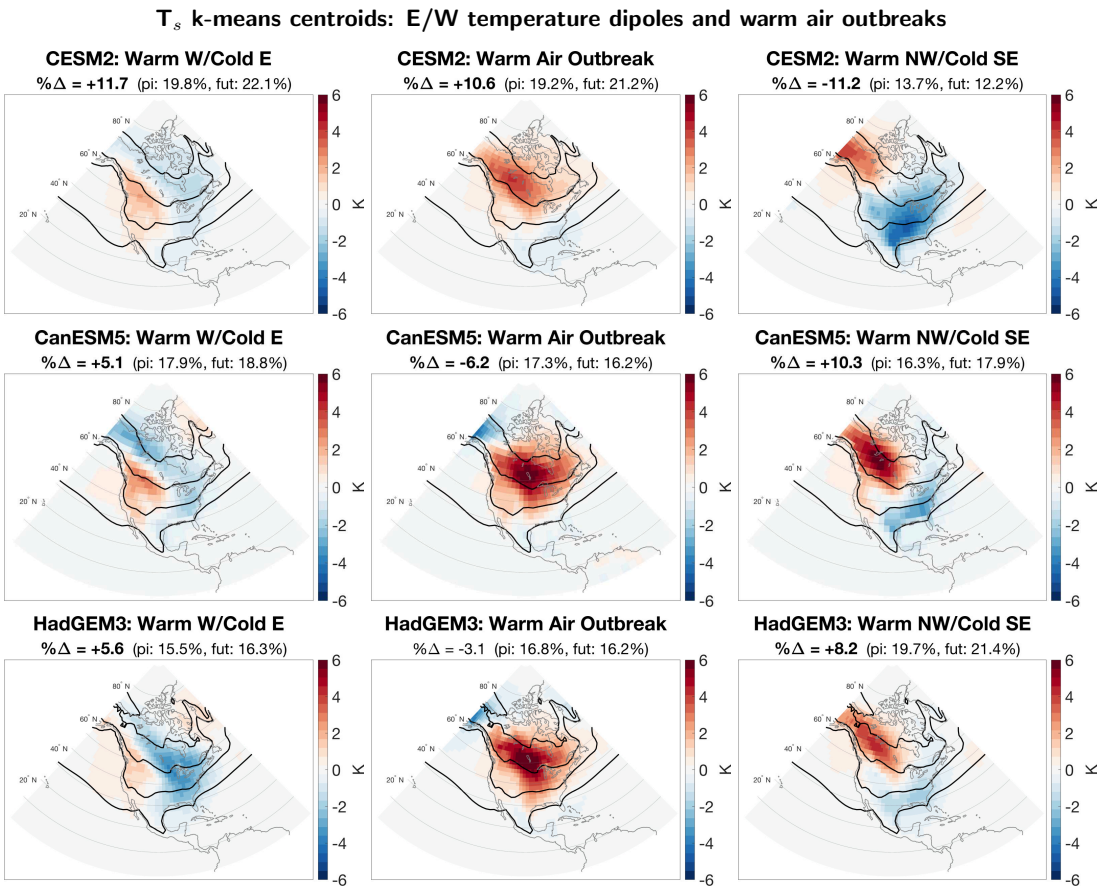

Fig. B.7. The January-February daily anomalous T_s centroids from three models (shading; CESM2, CanESM5, and HadGEM3 in rows 1-3, respectively) representing the following North American temperature patterns: Warm W/Cold E, Warm Air Outbreak and Warm NW/Cold SE (columns 1-3, respectively). Contours represent the piArcSIC January-February mean T_s, and bold face on the %Δ represents significance at 80% confidence.

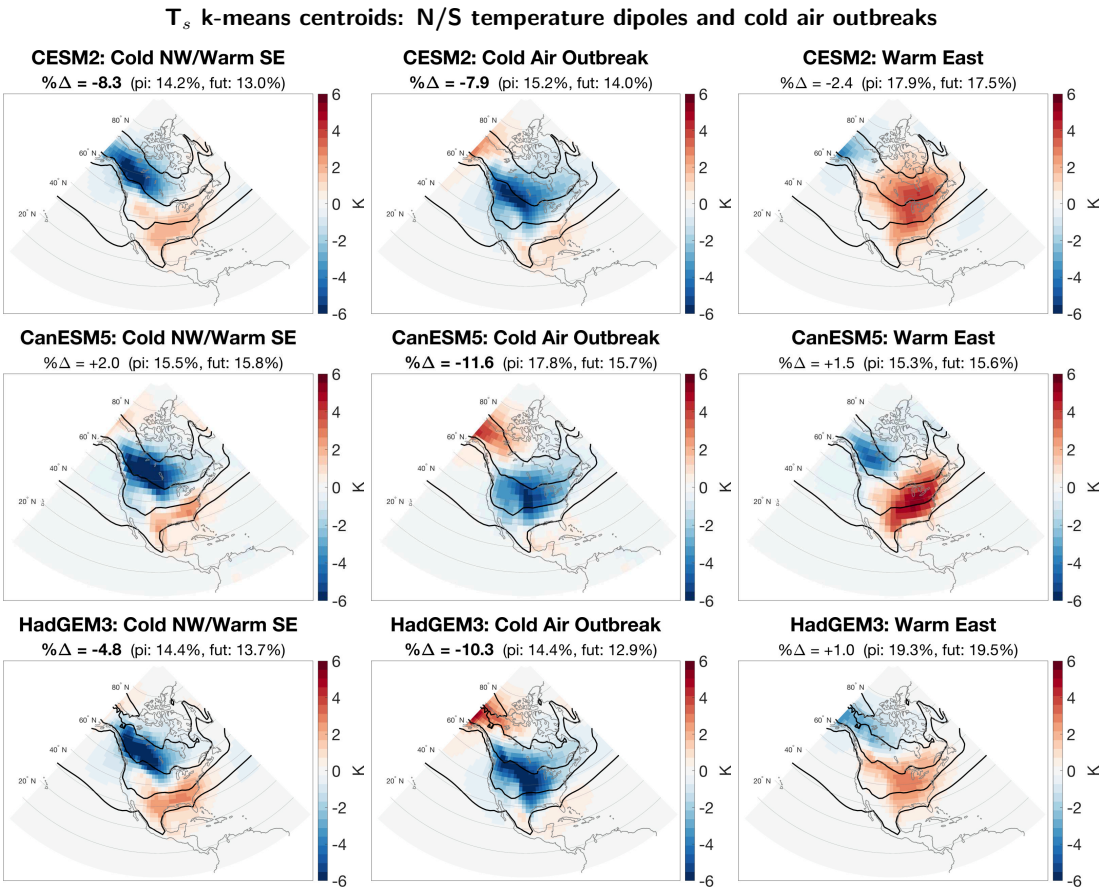

Fig. B.8. The January-February daily anomalous T_s centroids from three models (shading; CESM2, CanESM5, and HadGEM3 in rows 1-3, respectively) representing the following North American temperature patterns: Cold NW/Warm SE, Cold Air Outbreak and Warm East (columns 1-3, respectively). Contours represent the piArcSIC January-February mean T_s, and bold face on the %Δ represents significance at 80% confidence.